September 2015

Interplays of CO_2, Subnanometer Metal Clusters, and TiO_2: Implications for Catalysis and CO_2 Photoreduction

Chi-Ta Yang
University of South Florida, chita@mail.usf.edu

Interplays of CO_2, Subnanometer Metal Clusters, and TiO_2: Implications for Catalysis and CO_2 Photoreduction

by

Chi-Ta Yang

A dissertation submitted in partial fulfillment
of the requirements for the degree of
Doctor of Philosophy
Department of Chemical and Biomedical Engineering
College of Engineering
University of South Florida

Co-Major Professor: Babu Joseph, Ph.D.
Co-Major Professor: Venkat R. Bhethanabotla, Ph.D.
John Kuhn, Ph.D.
Rudy Schlaf, Ph.D.
Brandon Wood, Ph.D.

Date of Approval:
June 30, 2015

Keywords: Density Functional Theory, Catalysis, Photocatalysis, CO_2 Photoreduction, Ag/Pt Subnanometer Clusters, Structural Fluxionality, Decoration/Encapsulation

DEDICATION

To my Parents, Brother and my Wife.

ACKNOWLEDGMENTS

I would like to thank my advisors Dr. Babu Joseph and Dr. Venkat R. Bhethanabotla for their guidance, suggestions, and supports throughout my Ph.D. making me an independent and more mature researcher, motivating me to work harder, and bringing out the best of me; especially Dr. Babu Joseph, I am the grand student. I would also like to thank Dr. John Kuhn for the experimental guidance and supports to enable the validation of the computational results. Also, I would like to thank Dr. Brandon Wood for the guidance and suggestions to improve my research and writing skills. Thanks Dr. Rudy Schlaf for being my committee members, and also Dr. Matthias Batzill. I thank my labmates, Nianthrini Balakrishnan, Debosruti Dutta, Kassie Ngo, Ummuhah Cimenler and each individual in the labs. I thank Dr. Shi-Shang Jang for the encouragement and guidance that helped me attain this position. I want to extend my deep thanks to my mother, father, and brother for their supports and especially my wife for her understandings and encouragement. Most important, thank God for all the care and guidance.

TABLE OF CONTENTS

LIST OF TABLES

LIST OF FIGURES

ABSTRACT

This research is motivated by two significant challenges facing the planet: reducing the emission of CO_2 to the atmosphere and production of sustainable fuels by harnessing solar energy. The main objective of this work is the study of promising photocatalysts for CO_2 reduction. DFT modeling of CO_2, subnanometer Ag&Pt clusters, and anatase TiO_2 (101) surface is employed to gain fundamental understanding of the catalytic process, followed by validation using a guided experimental endeavor. The binding mechanism of CO_2 on the surface is investigated in detail to gain insights into the catalytic activity and to assist with characterizing the photocatalyst. For CO_2 photoreduction, the cluster induced sub-bandgap and the preferred adsorbate in the first and key step of the CO_2 photoreduction are explored.

It is found that TiO_2-supported Pt octamers offer key advantages for CO_2 photoreduction: 1. by providing additional stable adsorption sites for favored CO_2 species in the first step, and 2. by aiding in CO_2^- anion formation. Electronic structure analysis suggests these factors arise primarily from the hybridization of the bonding molecular orbitals of CO_2 with d orbitals of the Pt atoms. Also, structural fluxionality is quantified to investigate geometry dependent (3D-2D) CO_2 adsorption. Geometric information, electronic information, and C-O bond breaking tendency of adsorbed CO_2 species are proposed to connect to experimental observables (IR frequency). The CO_2 adsorption sites on supported Pt clusters are also identified using IR as the indicator. A cluster-induced CO_2 dissociation to CO pathway is also discovered. Finally, experimental work including dendrimer-encapsulated technique, TPD, and UV-Vis is performed

to validate the computational results, the availability of adsorption sites and CO_2 binding strength on supported Pt clusters.

CHAPTER 1: INTRODUCTION

1.1 Motivation

Harvesting solar energy to convert CO_2 to transferable hydrocarbon fuel addresses two major challenges facing the planet: reducing CO_2 levels in the atmosphere and generating renewable fuels.[1-3] According to an Intergovernmental Panel on Climate Change report(IPCC 2007),[4] the atmospheric CO_2 level have been rising at an increasing rate mainly due to the increased consumption of energy[3] with 81% of current energy usage coming from fossil fuels (2011).[3] Renewable fuels production from biomass, wind, solar energy are some possible ways to address this issue;[2] CO_2 photoreduction via sunlight is a very attractive option, because it addresses two significant challenges at the same time: reducing the emission of CO_2 to the atmosphere, and the production of sustainable fuels by harnessing solar energy.

Photocatalytic reduction of CO_2 involves first the absorption of incident photo energy that is equal to or greater than the band gap of the semiconductor to generate e-/h+ pairs in the conduction and valance bands, respectively. This is followed by the migration of the pairs to sites where the reduction of CO_2 and water take place, leading to production of hydrocarbons.[1, 2, 5-8] Recent reviews[1, 2] show that a large group of photocatalytic materials have activity for CO_2 conversion; however, efficiencies achieved to date have been abysmally small.[7] One challenge is that only a small fraction of the incident sunlight spectrum is utilized in creating e-/h+ pairs due to bandgap and band edge limitations. Doping the semiconductor with other materials such as N[9, 10] and Ag[11] is one approach proposed to lower the bandgap. The recombination of e-/h+ pairs is

another crucial challenge. The e-/h+ pairs tend to recombine either in the volume or on the surface of the semiconductor before redox reactions. Depositing metal nanoparticle such as Pt nanoparticle is one solution, the photo-generated electrons accumulating at the co-catalyst once these electrons are generated. The co-catalyst serves as a reservoir for the electrons and also promotes the reaction by lowering the activation barriers for the reduction reactions. A third approach that has been proposed is to use surface plasmon resonance (SPR) exhibited by nanoparticles to concentrate the electromagnetic field and promote the generation of e-/h+ pairs. The challenges and corresponding solutions are summarized[9, 12-18] in Figure 1.1.

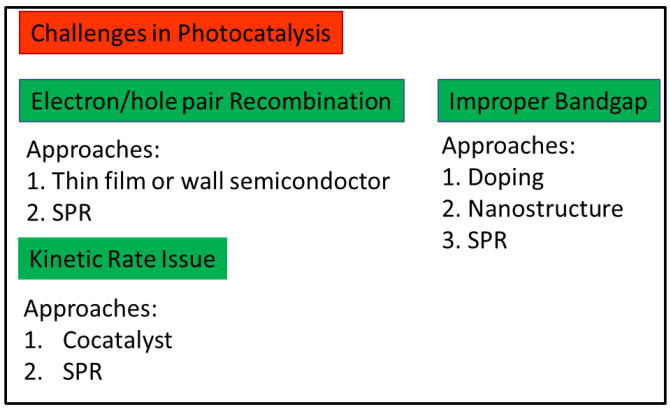

Figure 1.1 Summary of challenges and corresponding solution in photocatalysis

Nano- and sub-nanometer sized transition metal particles deposited on supports as the catalyst can enhance the activity of a variety of reactions including: organic photocatalytic degradation,[19, 20] direct propylene epoxidation,[21] CO oxidation,[22-25] and hydrogenation of acrolein and oxidative dehydrogenation of propane.[26, 27] For subnanometer metal clusters, consisting of several atoms, it has been shown that the activity enhancement is due to dynamic structural fluxionality,[24] larger fraction of under-coordinated surface atoms,[26] and the interactions between deposited cluster and the support.[28] A schematic representation of the advantages of subnanometer metal cluster and selected applications are shown in Figure 1.2. This has driven

this research on developing a new study of the subnanometer metal clusters based photocatalyst.[29]

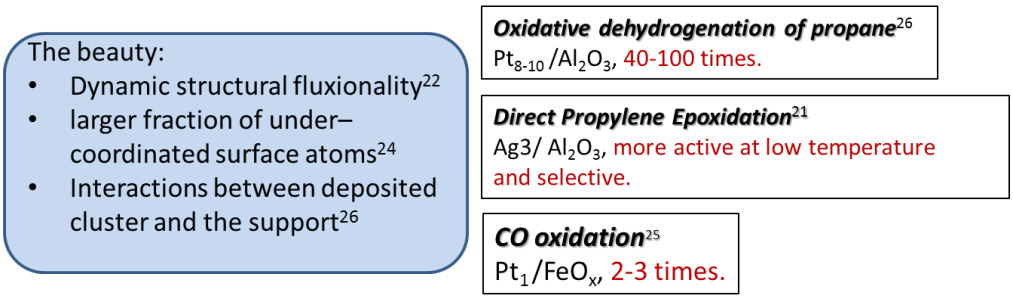

Figure 1.2 Advantages of subnanometer metal clusters and selected applications.

1.2 Approach Taken

In this research we study the properties of subnanometer Ag/Pt clusters deposited on anatase TiO_2 (101) surface to help design efficient catalysts and photocatalysts using *ab initio* calculations and dendrimer templated synthesis. An understanding of electronic and structural properties of such metal clusters adsorbed on support surfaces help gain insights into subnanometer clusters based catalysts. The application of subnanometer metal clusters on CO_2 photoreduction is studied to gain insights into a new class photocatalyst. Computational approach, VASP and Gaussian, provides understanding of interactions of subnanometer metal clusters, reactive species (CO_2), and the support surface. Derived information will then be verified with experimental results employing dendrimer-encapsulated subnanometer cluster synthesis. A schematic representation of this research is given in Figure 1.3. This methodology for the molecular design of photocatalysts can be used for other metal clusters and supports/semiconductors.

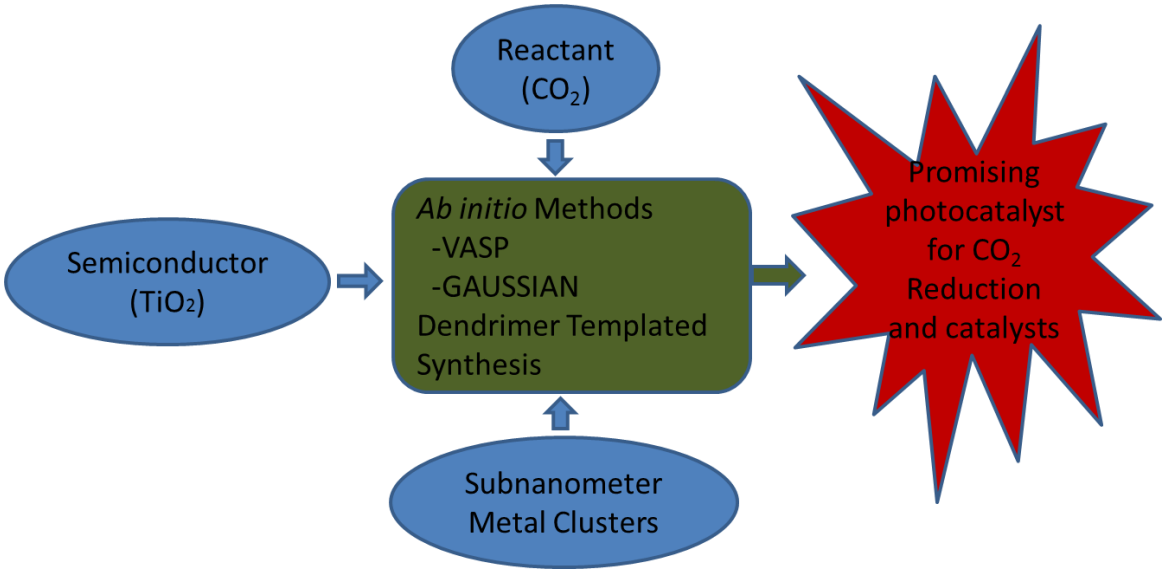

Figure 1.3 Schematic representation of this research.

1.3 Specific Objectives

Specific objectives of this research include:

- Study of the interplay between subnanometer Pt/Ag clusters and anatase TiO_2 (101): Study of binding mechanism to assist subnanometer clusters characterization, catalysis insights, sintering and decoration, photocatalysis insights, effect of metal induced sub-bandgaps.
- Study the effect of the presence of subnanometer metal clusters, the Pt cluster geometry, and the presence of extra electrons on the first and key step study of CO_2 photoreduction mechanism on anatase TiO_2 (101) supported Pt/Ag subnanometer.
- Dendrimer-encapsulated subnanometer cluster synthesis to validate the conclusions drawn from the computational method: sub-bandgaps and availability of key precursor binding sites.

1.4 Outline of Dissertation

The structure of this dissertation is as follows:

- Chapter 2 describes the computational and experimental methods: electronic structure calculations and dendrimer templated synthesis.
- Chapter 3 explores interaction between subnanometer Ag/Pt clusters and anatase TiO_2 (101) surface: implications for catalysis and photocatalysis.
- Chapter 4 investigates the key precursor adsorption in the first and key step of CO_2 photoreduction on the TiO_2 supported Ag/Pt octamers.
- Chapter 5 examines the Pt cluster size effect, structural fluxionality, on the key precursor adsorption.
- Chapter 6 studies the effect of added electrons on CO2 adsorption and reduction to simulate the effect of photoexcited electrons on photocatalysis.
- Chapter 7 attempts to validate the DFT results using Dendrimer- encapsulated synthesis technique, TPD, and UV-Vis experiments.
- Chapter 8 summarizes the conclusions and contains suggestions for future work.

CHAPTER 2: METHODS

In this chapter, methods for both computational and experimental work will be briefly described. The computational methods are based on electronic structure calculations to gain fundamental insights into the interactions of the CO_2, subnanometer metal clusters, and the support. Dendrimer based synthesis technique is used for the synthesis of the subnanometer clusters to validate the computational results.

2.1 Electronic Structure Calculations

Selected highlights in early first-principles calculations will be reviewed first in this section, followed by the introduction of Density functional theory (DFT), and of some important approximations to satisfy both computation efficiency and electronic property accuracy. Two softwares, VASP and GAUSSIAN, used in the research will be introduced last.

2.1.1 Early First-Principles Calculations

The ground-breaking Schrödinger equation is the basis of quantum mechanics, and the derived wave function from this equation given a specific Hamiltonian operator contains all electronic information needed. Born-Oppenheimer approximation is assumed to decouple the electronic and ionic variables in Schrodinger equation to simplify the problem. Early first-principles methods, Hartree and Hartree-Fock methods have a significant effect on the extraordinary density functional theory. The following are the descriptions of the abovementioned highlights.

2.1.1.1 Schrödinger Equation

The failure to apply classic mechanics to describe the behavior of small particles, like the electron, leads to the development of quantum mechanics. The foundation of this breakthrough is the Schrödinger equation (Erwin Schrödinger, 1926) as shown:

$$H\psi = E\ \psi \tag{2.1}$$

where, H is the Hamiltonian operator, ψ is wave function of the system, and E is the system energy. The Hamiltonian operator H is given by

$$H= E_n+E_e+U_{nn}+U_{ne}+U_{ee} \tag{2.2}$$

where E_n and E_e are kinetic energy of the nuclei and electron, respectively; U_{nn}, U_{ne},and U_{ee} are the potential energies regarding nuclei-nuclei, nuclei-electron and electron-electron, respectively. Note that the Schrödinger equation is a function of variables related to nuclei, electrons and time. If we focus on the time independent system, then time variable can be neglected in Equation 2.1, and this simplifies the problem. Another important assumption that brings the Schrödinger equation to further simplification is Born-Oppenheimer approximation (Born and Oppenheimer, 1927).

2.1.1.2 Born-Oppenheimer Approximation

An electron is far lighter than the nucleus and this means the former moves much faster than the latter. Therefore, when nuclei move, the electrons quickly react to the movement and always arrange themselves in the lowest energy states with respect to a given set of nuclear configuration. With this approximation, the nuclear and electronic variables are decoupled into separate mathematical formulation, meaning nuclear variable can be removed form Equation 2.1. The original Hamiltonian operator H, Equation 4.2, is also reduced to electronic related entities only:

$$H = E_e + U_{ne} + U_{ee} \quad (2.3)$$

The Schrödinger equation is then simplified to $(E_e+U_{ne}+U_{ee})\psi(r) = E\psi(r)$. Extending to many-electron problem, the Hamiltonian operator H is as below:

$$E_e = -\frac{\hbar^2}{2m}\sum_i \nabla_i^2 \quad (2.4)$$

$$U_{ne} = -\sum_{Ii}\frac{Z_I e^2}{|r_i - R_I|} \quad (2.5)$$

$$U_{ee} = \frac{1}{2}\sum_{i\neq j}\frac{e^2}{|r_i - r_j|} \quad (2.6)$$

The wave equation is now given by

$$\left(-\frac{\hbar^2}{2m}\sum_i \nabla_i^2 - \sum_{Ii}\frac{Z_I e^2}{|r_i - R_I|} + \frac{1}{2}\sum_{i\neq j}\frac{e^2}{|r_i - r_j|}\right)\psi = E\psi \quad (2.7)$$

2.1.1.3 Hartree and Hartree-Fock Methods

The pioneering approximation of the potential energy among electrons came from the Hartree method. This method assumes that the interactions among electrons are neglected and each electron experiences a mean field consisted of the electrons, leading to the separate non-interacting sub-systems instead of the many-electron system. Improved by Hartree-Fock (HF) method, the Slater determinant is introduced to incorporate the antisymmetry nature: when two electrons exchange their coordinates, the wave function should change its sign. Therefore, the exchange energy is considered in the HF method and this brings more accuracy to the obtained electronic properties. The corresponding Hamiltonian becomes

$$H = E_e + U_{ne} + U_H + U_x \quad (2.8)$$

Here, U_H represents Hartree potential and U_x accounts for the exchange energy.

2.1.2 Density Functional Theory

Hohenberg, Kohn, and Sham lay the foundation of Density functional theory (DFT). The electron density is introduced as the main player to solve the many-electron wave equation, and the problem is simplified from 3N dimensional problem to a set of N 3 dimensional problems. Note that the wave equation is moved from the wave function based problem to the electron density based problem. In DFT, the assumption of the noninteracting electrons makes possible the connection of the electron density and the related wave function; along with the Hohenberg-Kohn theorems (1964), and Kohn-Sham approach (1965), the ground-state electron density can determine all the electronic properties as those obtained from the wave equation method with appreciable reduced calculation cost. Selected important progress regarding the approximation of the term of Kohn-Sham equation and reduction of the computation cost will be highlighted.

2.1.2.1 Hohenberg-Kohn Theorems

The first theorem states that there is a relation between the ground-state electron density and the external potential, $U_{ext}(U_{ne})$. U_{ext} accounts for the interaction between the nuclei and electrons, so once the ground-state electron density is given, the external potential can be realized and vice versa. The corresponding Hamiltonian is then defined, so are all other electronic properties in the ground state of a system. The second theorem states the validation of the application of the variational principle on the DFT. The ground-state energy of the system can be obtained by varying the electron density. The minimum energy is the ground-state energy of the system and the ground-state electron density is the electron density at that minimizing state.

2.1.2.2 Kohn-Sham Approach

The Kohn-Sham (KS) ansatz is that the interacting many-electron system is represented as noninteracting one-electron sub-systems plus the exchange-correlation term. This means the electron density of the true physical problem can be obtained by dealing with a more solvable fictitious formulation. Note that the interacting and noninteracting terms are decoupled by this approach. In sum, the Hamiltonian of the Kohn-Sham approach is

$$H_{ks}= E_e+U_{ext}+U_H+U_{xc} \tag{2.9}$$

where E_e is the noninteracting kinetic energy here; U_{xc} is the exchange-correlation potential energy, and all the interacting elements are included in this term. With the theorems and approach, the system variables are reduced, and the electron density, external potential, Hamiltonian and wave function are interconnected. As shown below, the corresponding Kohn-Sham equations are therefore used in the framework of DFT.

$$H_{ks}\ \psi_i^{ks} = E\ \psi_i^{ks} \tag{2.10}$$

where ψ_i^{ks} is the KS orbital, which is the eigenfunctions of the KS equations.

2.1.2.3 Exchange and Correlation Functionals

Local density approximation (LDA) and generalized gradient approximation (GGA) are two most common methods to approximate the exchange-correlation term in Equation 2.9. LDA take the information of the local density to approximate the exchange and correlation functional. The idea is that the real electron density distribution is treated as a combination of pieces of homogeneous electron densities and the total property is then approached by summing up those of each element. On the other hand, GGA further considers the local gradient at a given point. Therefore, the GGA consider both local and semilocal information of the electron density. The common GGA based methods are Perdew-Wang (PW91)[30] and Perdew-Burke-Enzerhof (PBE)[31].

One important limitation of both methods is the underestimation of the bandgap, about 50% smaller.

2.1.2.4 Basis Set

In electronic structure calculations, the basis set is the mathematical formulation of the orbitals to make possible theoretical calculations. There are two common types of basis set: local and plane wave. Local basis set, Gaussian and atom-centered orbitals, is suited for isolated system such as atoms and molecules, because the localized nature of orbitals of such systems is satisfied. For the periodic systems, the plane wave basis set is a better choice. Plane wave basis set meets the Bloch theorem and the periodic boundary conditions. Also, they are orthonormal solutions and convenient for the related mathematical operations and Fourier transformation. However, for each atom in the systems, more than a hundred plane waves are needed and even in the vacuum space, and this makes the calculations tedious.

2.1.2.5 Pseudopotential Approach

In a chemical reaction or any physical property calculation, valence electrons mainly participate, whereas the core electrons mostly stay inactive due to their tight bounding to the nucleus. This facilitates the idea to freeze the core electrons leading to the pseudopotential (PP) approach.[32, 33] By neglecting core electrons in the calculation, the needed number of basis set is significantly reduced. The PPs are said to be hard and soft by the high and low cutoff energy adopted, respectively. The common PPs are ultrasoft pseudopotentials (US-PP)[34] and projector-augmented wave (PAW).[35] The US-PP is known for its reduced amplitude of the pseudo wave function and therefore smaller cutoff energy is sufficient and this leads to less computation cost. Note that USPP generates only valence charge density instead of total charge density. PAW is designed to consider both core and some valance parts of the wave function, in order to maintain

both the advantage of low computation cost and accuracy of the normal wave function; in addition, total charge density can be obtained from this method.

2.1.3 VASP

Vienna Ab Initio Simulation package (VASP) is a DFT based software tool developed by Mike Payne, Jürgen Hafner, Georg Kresse and Jürgen Furthmüller. It is used to perform *ab-initio* quantum mechanical molecular dynamics at finite temperature. VASP is equipped with US-PPs and PAW for PPs, and LDA and PBE for exchange-correlation functionals under the plane wave basis set, so it works well for the periodic systems. VASP carries electronic and ionic minimizations, generating the electronic properties such as total energy, density of state, band structure and partial charge density. The minimization framework of VASP involves an outer loop for ionic minimization and an inner loop for electronic minimization. The general flow of VASP starts with evaluation of the H_{ks} given the input files, solve the KS equations for KS orbitals and then test convergence of the generated electron density in each iteration. If the convergence is met, the output files are generated and so are the electronic properties.

2.1.4 Gaussian

Gaussian is an electronic structure package for computational chemistry mainly developed by the group led by John Pople. A graphical user interface (GUI), GaussianView, is also developed to offer a friendly use of Gaussian. Gaussian is embedded with a variety of theoretical levels, from semi-empirical, HF related to DFT. It supports the prediction of electronic properties such as total energy, stable and transition state molecular structures, and vibrational frequencies. Modeling of excited states and systems in solution are also one capability of Gaussian. Contrary to VASP, Gaussian works well for isolated systems due to its focus on the local basis sets.

2.2 Experimental Methods

The common techniques to prepare the subnanometer cluster can be classified into physical and chemical routes. For the physical route, the clusters are created using laser deposition by focusing YAG laser beam on a specific metal rod, then directed to quadrupole mass selector, and finally deposited on the support at ultrahigh vacuum. Selected examples are Ni_n(n=1,2,5,10,15)[36], Ag_n (n=1-3)[37], and Au_n (n=1-4,7)[38] on rutile TiO_2. Dendrimer templated synthesis, on the other hand, is one common chemical route for the synthesis of subnanometer clusters. In this section, a brief review of the nanoscopic nanoparticles (NPs) synthesis methods will be presented first, followed by the introduction of dendrimer templated synthesis.

2.2.1 Brief Review of Nanoscopic Metal Synthesis Methods

There are two ways to synthesize metal NPs, top down methods and bottom up methods. The former starts with grinding of bulk metals, and followed by stabilization procedures; the latter is based on the reduction of the metallic precursors, also called chemical reduction.[39] In this section, some common synthesis methods are briefly introduced including their recent applications, followed by the introduction of the dendrimer templated synthesis.

2.2.1.1 Chemical Reduction

Chemical reduction method is the chemical reduction of the metal salts aqueous solution to zerovalent metal colloids in the presence of surfactant or polymeric ligands (PVP) to control the nanoparticle growth and to prevent agglomeration. Since Faraday first developed this method in 1857, two mainstream reduction methods have been developed and widely used, co-reduction and successive reduction. Co-reduction is the simultaneous reduction of the proper metallic precursor mixture in a single reduction step by reducing agents. By simultaneously reducing the aqueous mixture of $HAuCl_4{\cdot}4H_2O$ and $AgClO_4$ using reducing agent $NaBH_4$, Toshima and

coworkers[40] obtained Ag(core)-Au(shell) bimetallic nanoparticles. Walker et al.[41] synthesized Au-Cu nanocubes by co-reduction of Cu-(acac)2 and $HAuCl_4$ using 1-dodecanethiol (DDT). On the other hand, successive reduction is the consecutive reduction of one metallic precursor after the previous reduction step. Marzan and colleagues[42] obtained multishell Au and Ag bimetallic NPs by successive reduction of $AgNO_3$ and $HAuCl_4$ in the existence of CTAB. Yacaman et al.[43] obtained a three layer core shell Au-Pd bimetallic NP with alloyed core, Au-rich intermediate layer, and Pd-rich outer shell.

2.2.1.2 Electrochemical Synthesis

The basic idea of this method is to have a sacrificial metal anode. When the sacrificial metal is oxidized, metal ion migrates to cathode where reduction, nucleation, and growth then take place.[39] Finally, mono or bimetallic NPs are formed. The advantage of this method according to Ma et al.[44] is its high yield, ease of operation and risking by-products. They co-reduced chloroauric acid ($HAuCl_4$) and silver nitrate ($AgNO_3$) in the presence of poly(vinyl-pyrrolidone) (PVP) to synthesize Au-Ag NPs. Rashid-Nadimi and coworkers[45] also obtained Au@Pt core shell bimetallic NPs with this method. A gold electrode was used, followed by the adsorption of $[PtCl_6]^{2-}$ on the produced gold NPs. Pulsed potentiostatic reduction was adopted to obtain the Au@Pt NPs.

2.2.1.3 Radiolysis

In this method, solvated electrons produced from the γ-ray irradiation of water reduce the metal ions, leading to the formation of NPs. Various sized bimetallic Ag-Pt and Au-Pt NPs were prepared by Delcourt et al.[46], irradiating aqueous containing Ag_2SO_4 and K_2PtCl_4 with different stabilizing agents. Recently, Nitani and colleagues[47] demonstrated that employing a 4.8-MeV

electron beam to reduce the metal ions without any surfactant or stabilizer's presence, and bimetallic composite NPs of Pt-Au, Pt-Cu and Pt-Ni on γ-Fe_2O_3 were synthesized.

2.2.1.4 Sonochemical Synthesis

This technique was carried out by Mizukoshi et al.[48] to prepare Au@Pd core shell NPs. The reduction of Au and Pd ions in the solutions of $NaAuCl_4 \cdot 2H_2O$, $PdCl_2 \cdot 2NaCl \cdot 3H_2O$, and sodium dodecyl sulfate (SDS) was carried out by ultrasound irradiation. Ashokkumar and colleagues[49] also reported the synthesis of Au-Ag Core-Shell bimetallic NPs by sonochemical method and claimed that this method could also be used to prepare other core shell NPs composed of a number of bimetallic systems.

2.2.1.5 Photochemical Synthesis

As has been reported by by Majima et al.[50] in their recent comprehensive review paper, the essential of the photochemical approach is the formation of M^0 under the conditions that prevents their precipitation. M^0 is formed in two ways. Direct photoreduction is the straight photoreduction of the metal source, while photosensitization is using photochemically generated intermediates to reduce the metal ions. The advantage of this method is clean process, high spatial resolution and a great versatility. In the work done by Scaiano's group,[51] the photochemically generated 2-hydroxy-2-propyl radical was used for the reduction of $HAuCl_4$ and $AgNO_3$ in aqueous surfactant solutions, producing Au-Ag bimetallic NPs with different composition and architecture, alloys and core-shells.

2.2.2 Dendrimer-Encapsulated Subnanometer Cluster Synthesis

Dendrimer templated synthesis of metal nanoparticles is one remarkable technique to obtain the size-controlled metal nanoparticles, which improves one important issue, sintering, for subnanometer cluster. Dendrimers are quasuspherical hyperbranched functional groups that are

well organized from the core to the boundary and it is these functional groups that prevent the aggregations.[52] The potential applications are catalysis, drug delivery, and molecular recognition.[53] Depending on the accumulation sites of metal nanoparticles within the denderimer, there are four common metallodendrimers: (a) dendrimer-encapsulated metal particle, (b) periphery metallodendrimers, (c)core metallodendrimers, and (d) focal-point metallodendrimers.[53] The major synthesis steps are complexation and reduction. For dendrimer-encapsulated metal particle, there are two common dendrimers, Poly (amidoamine) (PAMAM) and poly(propylene imine) (PPI), and for PAMAM there exists three common dendrimer generations, Gn-OH(n=4,6, and 8) dendrimers, each with a theoretical distance between two outermost hydroxyl groups as 8.2, 5.4, and 3.2 Å, respectively.[53] The nanovoid within the dendrimer allows the formation of the coordination bond between metal ion and the internal tertiary amine groups, which is the complexation step. Note that, the size of the nanoparticle is determined by the ratio of the metal ion/dendrimer. The following step is the reduction of the metal ion to zerovalent metal by reducing agent NaBH4.[54] Selected example are Pd_n (n=4,8,16) using poly(propylene imine)[55], Pt_{12} and Pt_{13} using fourth-generation dendritic phenylazomethine with a triphenylpyridylmethane core[56], and bimetallic Ni-Fe nanoparticles of ~1nm using fourth-generation poly aminiamide.[57] In this research, we focus on the dendrimer-encapsulated metal particle to study the sub-bandgap behavior of the subnanometer mono/bi metallic clusters and applications of subnanometer metal clusters on CO_2 photoreduction.

CHAPTER 3: INTERPLAY BETWEEN SUBNANOMETER AG AND PT CLUSTERS AND ANATASE TIO_2(101) SURFACE: IMPLICATIONS FOR CATALYSIS AND PHOTOCATALYSIS[58]

This chapter summarizes the fundamental study of the interplay between subnanometer metal clusters and the support to shed lights on the design of promising (photo)-catalysts. Structural and electronic properties of Ag_n and Pt_n (n=2, 4 and 8) clusters deposited on anatase TiO_2 (101) surface were investigated using Density Functional Theory. Binding mechanisms that characterize deposited subnanometer clusters on the model surface in terms of favored sites and geometry insights were explored. The restricted movement of interfacial cluster atoms as well as top layer cluster atom - surface atoms interaction was found to affect the adsorption characteristics. Metal nanoparticle encapsulation by the support is explained via the tendency to maximize orbital overlaps between deposited clusters and surface atoms. The cluster sintering was evaluated using adsorption energy and the number of local minima as indicators, suggesting sintering is less likely to occur for Pt cluster on the model surface. The cluster induced sub-bandgaps are investigated in terms of its formation, size effect, and the correlation with d-band distribution.

3.1 Introduction

Nano- and sub-nanometer sized transition metal particles deposited on supports have been shown to enhance the catalytic activity of a variety of reactions including: organic photocatalytic degradation,[19, 20] CO oxidation,[22-24] hydrogenation of acrolein and oxidative dehydrogenation of propane.[26, 27] For subnanometer metal clusters, consisting of several atoms, it has been shown that the activity enhancement is due to dynamic structural fluxionality,[24] larger fraction of under-coordinated surface atoms,[26] and the interactions between deposited cluster and the support.[28] An understanding of electronic and structural properties of such metal clusters adsorbed on the support surfaces will help the efficient design of subnanometer clusters based catalysts or photocatalysts.[29]

A number of investigators[21, 23, 24, 26, 59-69] have done experimental studies on the catalytic effect of oxide surfaces supported subnanometer clusters. Pt_{8-10} clusters based catalysts for the oxidative dehydrogenation of propane showed 40-100 times more reactivity than Pt monolith and vanadia.[26] Oxidation of CO over Pt_7 deposited TiO_2(110) with varying reduction state of the TiO_2 support was studied,[61] and the slightly reduced state showed two orders of magnitude larger CO_2 production rates than the strongly reduced state. Direct propylene epoxidation on Ag_3 and Ag_3 aggregates supported on alumina suppressed CO_2 formation while showing high activity at low temperature.[21] Studies[59, 62, 63, 68, 69] have also shown that the catalytic property of the subnanometer cluster varies with size as well as the geometry. However, while experimental characterizations of such clusters identify stable adsorption sites,[62] one finds it hard to experimentally determine the stable geometry of such clusters. Sintering is also an important issue in the subnanometer cluster related studies.[26] Lei et al. observed sintering initiation of Ag trimer supported on alumina at 110°C.[21] A motivation of this paper is to gain an understanding of

the interaction between the cluster and support, to suggest binding mechanisms associated with deposited subnanometer metal clusters, and also to shed light on the catalytic characteristics, such as sintering and encapsulation/decoration.

One approach taken to improve the efficiency of the semiconductor photocatalyst is to deposit noble metal nanoparticles on the semiconductor surface.[18, 70] The nanoparticles serve as a co-catalyst to reduce the recombination of e-/h+ pairs, and also as plasmonic particles to increase the concentration of photoexcited electrons.[71, 72] On the other hand, subnanometer clusters can potentially introduce additional electronic states within the bandgap (sub-bandgap) of the semiconductor.[73, 74] Thus, it is possible to generate a new class of photocatalysts by employing subnanometer metal clusters to lower the bandgap of semiconductors, allowing utilization of a broader spectrum of sunlight.

Prior studies concerning the behavior of TiO_2 supported subnanometer clusters suggested that the preferable site for Ag clusters is the hollow site between twofold coordinated oxygen atoms for Ag_n(n=2, 4, and 8) adsorbed on anatase TiO_2 (100).[75] Au_n(n=1-7) on the stoichiometric rutile TiO_2 (110) surface prefers the site where the number of Au-O bonds is maximized.[76] A recent study provided insights into the binding mechanism and geometry of Pt_n(n=4-8) supported on rutile TiO_2(110) surface.[77] A DFT study of Pt_n(n=1,2,7,10 and 37) clusters[78] on anatase TiO_2 (101) surface suggested that island-like particle is the preferred configuration. Gong et al. studied the adsorption properties of Pt_n and Au_n (n=1-3) on TiO_2 surfaces using combined experimental and computational methods.[79] 2-fold coordinated oxygen sites is suggested nucleation center for Pt_n (n=1-3)[73] and structural and electronic properties of bimetallic Pd_mAg_n(m+n=2-5) were also investigated.[80] Prior reports regarding sub-bandgap states focused on Pt_n(n=1-3),[73] Pt_n(n=1-8),[81] and Ag clusters (dimer, tetramer, and octamer)[74, 75] on anatase and rutile TiO_2 surfaces.

The physical and chemical properties of single crystal are related to the dominating exposed surface structure,[82] and this indicates the importance of understanding the behavior of different TiO_2 surfaces. Nonstoichiometric TiO_2 surfaces such as those with oxygen vacancies, bridge hydroxyl groups, and interstitial Ti atoms[83] have been observed under room temperature. Studies regarding oxygen vacancies have been done on rutile (110) surface using theoretical method,[84, 85] and on anatase (101) surface using combined experimental and theoretical approach.[79] For anatase (101) surface, experiments tend to find oxygen vacancies in the bulk than on the surface.[86] This implies that the pristine surface for anatase (101) is favored over vacant surfaces in the absence of adsorbates on the surface. Recent studies mentioned above have also shown promising catalytic results from Pt and Ag subnanometer clusters. Zhou et al. summarized the wide applications of Pt in heterogeneous catalysis, and pointed out the concern about the high cost of Pt metal.[78] In this study, Ag_n and Pt_n (n=2, 4, and 8) deposited on the perfect anatase TiO_2 (101) surface were examined using *ab initio* calculations. Objectives of this study are to (i) develop an understanding of the binding mechanisms between adsorbed clusters and surfaces, (ii) study the geometry and its effect on adsorption energy as a function of cluster size, (iii) gain insights into the decoration/encapsulation phenomenon in catalysis, (iv) suggest indicators characterizing the sintering of subnanometer clusters deposited on support, and (vi) explore the behavior of sub-bandgaps introduced by subnanometer clusters on semiconductor and correlate sub-bandgap states with theoretical descriptors.

3.2 Computational Details

We studied Ag and Pt dimer, tetramer, and octamer (two dimensional (2D) and three dimensional (3D) geometries) on anatase (101) surface[82] (see Figure 3.1). The surface Ti atoms contain five-fold coordinated Ti (5c-Ti), and six-fold coordinated Ti (6c-Ti) atoms. The surface

oxygen atoms comprise two-fold coordinated O (2c-O) and threefold coordinated O (3c-O), and the latter includes 3c-O in between five-fold coordinated Ti (3c-O(5Ti)) and in between six-fold coordinated Ti (3c-O(6Ti)) atoms.[78] VASP (Vienna Ab Initio Simulation package) code[87-89] was used with the Perdew–Burke–Ernzerhof (PBE) form of the generalized gradient approximation (GGA)[90] functional for the exchange and correlation functional along with projector-augmented wave (PAW) pseudopotentials.[91] A kinetic energy cutoff of 500 eV was used. Spin restricted calculations were carried out with an force tolerance of 0.01 eV/ Å. The standard DFT underestimates the bandgap due to DFT's inability to accurately model the strongly correlated localized 3d electrons of the Ti atoms, and the calculation using DFT+U is suggested. It was reported that for transition metal cluster adsorbed on the TiO_2 surface, the trends of the charge distribution and cluster stability are similar for calculations done with DFT and DFT+U.[80, 81, 92] DFT is used in this study and the band gap states reported should be used only for trending purposes. The (2x1) and (3x1) supercells of the anatase TiO_2 surface with six trilayers were considered for dimer and clusters larger than dimers, respectively. Among the six trilayers, the bottom three layers were frozen, while the top three layers and subnanometer clusters were allowed to relax. The Monkhorst-Pack[93] meshes of 4x4x1 k-point sampling in the Brillouin zone were used to study the adsorption of the clusters on the model surface except 6x6x1 was used for the density of state (DOS) calculations. The vacuum region between the slabs was set to 15 Å. The initial stable structures of clusters(clusters in the gas phase) were obtained as follows: initially using the Gaussian09 program package[94] with B3LYP functional[95, 96] and LanL2DZ basis set for the Ag and Pt atoms, and then VASP with the parameters mentioned earlier. The stable configurations of clusters on the model surface were then obtained via VASP from geometry optimization of the assumed initial adsorption configurations.

Total and atom-projected density of states (p-DOS) of the model systems within the energy range of interest (between the bottom of the valance band (VB) and the bottom of the conduction band (CB)), the density plot (DP), and d-band center and the standard deviation of d states[97] were examined to study electronic structure interactions of the subnanometer clusters with the model surface. Climbing Image Nudged Elastic Band (CI-NEB)[98-100] was used to determine the activation barrier and to suggest an encapsulation pathway. The zero position in each DOS and PDOS figure of this paper corresponds to the Fermi level. The density plot is the partial charge density within a specified energy range of the resonant peaks in the p-DOS calculated using VASP, and the density plots show equal density surfaces of 0.0005e/ $Å^3$. The critical bond formation distance between the metal and the binding atoms is taken as 3.00 Å. The adsorption energy of the cluster was calculated as the difference between the total energy of the surface with the cluster adsorbed, and the sum of the energies of the free cluster and clean anatase TiO_2 (101) surface. The more negative adsorption energy indicates most possible stable adsorption configuration on the model surface.

3.3 Results and Discussion

3.3.1 Binding Mechanism of Ag and Pt on TiO_2

Different initial adsorption configurations were relaxed in VASP to determine the possible stable configurations. (See Appendix B, Fig. B1-3). We explored (i) the stable cluster geometries and (ii) the favored cluster adsorption sites on the model surface (the cluster's binding tendency toward the surface) as a function of the cluster size. Observations from the cluster geometry are first summarized and then examined by electronic structure calculation results. The two most stable configurations were studied. The trends of electronic properties

from both configurations are the same, so the results for only the most stable configurations are shown except for a few cases.

3.3.1.1 Stable Geometry of Adsorbed Clusters on TiO_2

For Ag and Pt Dimers, the most stable Ag dimer configuration is shown in Figure 3.2a, where Ag1 is binding with two 2c-O atoms, while Ag2, located above the 5c-Ti, with one 2c-O. The second most stable configuration is shown in Figure 3.2b, with Ag dimer vertically adsorbed on one 2c-O. In the most stable mode, Ag-Ag bond length increased to 2.61 Å compared to the dimer in the gas phase (2.58 Å). When Ag dimer adsorbs in parallel to the model surface, the site that allows more interaction of Ag and 2c-O is favored. This is consistent with Ag dimer on the anatase TiO_2 (100) surface, where the preferred site for Ag dimer is between 2c-O.[75] Note that the most stable configuration of Ag dimer adsorbed on the anatase TiO_2 (100) exhibited two separated Ag atoms lying between 2c-O atoms.[75] We studied Ag dimer placed in parallel to the [010] direction and the dissociation of Ag2 was not observed. The optimum configuration turned out to be the same as the most stable configuration. We believe this is due to the difference of the surface structures of each anatase(100) and anatase(101), the former having longer distance between 2c-O atoms along [010] direction than that of the latter. Moreover, the converged geometry from the assumed initial configurations reveals that 5c-Ti helps to stabilize the horizontal adsorption of Ag dimer on the surface, while in the case of vertical adsorption 5c-Ti does not have a significant influence.

In the case of Pt dimer, the most stable configuration is shown in Figure 3.2c, reported as second stable mode in the study of Han and coworkers.[73] Pt2 is located in between the 2c-O and 5c-Ti atoms, while Pt1 is located above 3c-O (5Ti). The distance between the bridging 2c-O atoms was increased from 3.82 Å to 4.08 Å in the direction parallel to [010]. This increase was

also found in the second most stable configuration shown in Figure 3.2d, each Pt atom pushing the bridge oxygen, from 3.82 Å to 4.85 Å. To sum up, Pt dimer tends to be attracted by 2c-O, 3c-O, 5c-Ti and 6c-Ti atoms, and the length of the dimer increases to maximize overlap with the surface atoms, and this agrees with the conclusion from Han et al.[73] that Pt dimer either binds with 2c-O or 5c-Ti, and the length of Pt dimer increases significantly. Similar binding tendency of Pt dimer is reported on the rutile TiO_2 (110) surface[101] where the possible adsorption sites are between oxygen rows, and Pt-Pt bond increased by 0.24 Å.

For Ag and Pt Tetramers, the two most possible stable Ag tetramer adsorption configurations are shown in Figure 3.3, a & b, respectively. From different initial 2D geometries, the converged Ag tetramers exhibiting 3D geometry are more stable than converged 2D Ag tetramers. This indicates 3D is the favored geometry for Ag tetramers adsorbed on the surface. The optimized geometry of Ag tetramer was also 3D on the anatase TiO_2 (100) surface.[75] Figure 3.3a shows a pyramidal structure, each of the Ag atoms in the bottom triangle interacting with each 2c-O and Ag3 interacting with 5c-Ti. The stable adsorbed geometry of the second most stable mode (Figure 3.3b) is that Ag2 and Ag4 each binds with 2c-O, while Ag1 binds with two 2c-O atoms.

The most possible stable configuration of the Pt tetramer, Figure 3.3c, is a 3D geometry similar to a pyramid. In contrast to the Ag tetramer, the second most stable one, Figure 3.3d, remained a 2D geometry. This is different from the rutile TiO_2 (110) surface, where stable geometry of the adsorbed Pt tetramer was reported mainly 2D and square like structure.[77] The average distance between each interfacial Pt and 2c-O is 2.08 Å for the most stable configuration, while it is 2.13 Å for the second; the average distance between the binding Pt and surface Ti atoms for the former configuration is 2.57 Å, whereas it is 2.68 Å for the latter. It reveals that Pt

tetramer favors the site possessing most bonds of the Pt with surface Ti and 2c-O atoms, consistent with observations derived from the Pt dimer cases except for 6c-Ti's more important role here.

For Ag and Pt Octamers, shown in Figures 3.4 a&b are the two most stable Ag octamer configurations. The average distance between the binding Ag and the 2c-O is 2.25 Å for both configurations. The average distance between Ag and 5c-Ti atom is similar for both, 2.98 Å and 3.04 Å. Ag octamer favors the parallelogram at the interface, and the sites assisting maximum binding of Ag atoms with 2c-O are favored along with 5c-Ti's involvement. The major difference from the tetramer case is less involvement of 3c-O (5Ti). Note that among the two most stable configurations, we find that the top layer of the Ag octamer affect the adsorption energy, which numerically are -1.30 eV and -1.28 eV.

For Pt octamer, the most stable configuration (Figures 3.4c) has five bonds of Pt with surface Ti atoms (~2.74 Å) and three bonds with 2c-O atoms (~2.08 Å), while the second most stable(Figures 3.4d) configuration has three bonds of Pt with surface Ti atoms (~2.72 Å) and four bonds with 2c-O atoms(~2.05 Å). Similar to Ag octamer adsorption, the parallelogram structure is the favored interfacial shape. In addition to 2c-O and surface Ti atoms, 3c-O (5Ti) atom shows tendency to bind with Pt octamer, as revealed from the average distance of 2.11 Å between Pt and 3c-O (5Ti) (Figure 3.4c).

3.3.1.2 Binding Tendency of Clusters on TiO_2

For Ag Dimer, Tetramer, and Octamer, to investigate the binding tendency of the considered clusters toward the stoichiometry anatase TiO_2 (101) surface, p-DOSs of the most stable adsorption configuration in each case within the energy range of interest were examined, as shown in Figures 3.5a-c. The peaks of Ag and O atoms show stronger resonance in the VB,

while those of Ag and Ti atoms show such resonance in the bottom of the CB. This suggests Ag clusters have stronger tendency to interact with the O atoms in lower energy levels and with Ti atoms in higher energy levels. Within the bandgap, both atoms show comparable interacting tendency. Most of the resonant peaks occur within the VB and this discloses O atom's stronger tendency compared to the Ti atom to interact with the Ag clusters.

Further examination of the p-DOS of surface 2c-O, 3c-O, and total O atoms of the most stable configurations of each Ag cluster, Figure 3.6a-c, it indicates that Ag clusters of interest have the disposition to bind with 2c-O, consistent with previous studies of Ag clusters on anatase TiO_2 (100) surface.[75] Moreover, there is also a tendency to bind with 3c-O, not obvious from the geometry observation alone. As revealed from insets in Figure 3.6, a & c, at energy levels within the bandgap, 2c-O shows stronger interaction with Ag clusters than 3c-O, while reverse trend is found for the remaining energy levels. This reveals that 3c-O atoms play an important role in the Ag dimer, tetramer, and octamer adsorption.

DPs of significant resonant peaks in each Ag dimer, tetramer, and octamer systems were investigated in order to identify the surface atoms that have the tendency to bind with the Ag clusters. Selected DPs that suggest apparent bonding interactions are shown in Figures 3.5 a-c. In the case of Ag dimer, at -2.41eV and -3.45eV in Figure 3.5a, bonding orbitals formed by 2c-O can be clearly seen; for example, at -3.45eV Ag1 is interacting with 2c-O to form bonding orbital. At -2.41eV in the same figure, bonding orbital formed by 3c-O can also be seen. DP located at -4.7eV in Figure 3.5b shows that both 2c-O and 3c-O (5Ti) form bonding orbital with Ag4 of the Ag tetramer. In the case of Ag octamer, DPs around -4.0eV and -4.9eV show the formation of bonding orbitals from 2c-O and Ag3, while around -4.9eV bonding orbitals from 3c-O (5Ti) and Ag1 can be seen. On the other hand, the bonding orbital formed from 5c-Ti and 6c-Ti atoms

were scarce, with mainly 5c-Ti interacting around Fermi level, as seen in DPs around 0eV in Figure 3.5a-c. One possible reason for 6c-Ti's lack of involvement is due to its inward position on the model surface. The size, shape, or orientation restrictions of its atomic orbitals with respect to those of each HOMO of Ag clusters at each energy level are also possible reasons. This leads to insubstantial orbital overlaps and hence bonding orbitals are not able to form. The observations of DPs confirm that Ag clusters tend to bind with surface O in the lower energy range while with surface Ti in the high energy range. Moreover, as the cluster size increases from two to eight, the binding dispositions of the surface atoms with the Ag clusters do not vary.

From our investigations of the DPs regarding the two most stable adsorption configurations of the Ag octamer, bonding orbitals involving 3c-O (5Ti) atoms are seen, but overall they are a minor population. This could be explained by the restricted freedom of Ag atoms in the bottom layer of Ag octamer. In Figure 3.4a, for example, the interactions between the Ag atoms in top layer and Ag3/Ag4 restrict the movements of Ag3/Ag4 in $[10\bar{1}]$ direction and prevent the interaction with the 3c-O (5Ti). Comparing angles, Ag3 is at an angle of 100.94° with 2c-O and 6c-Ti in Figure 3.4a, while Ag4 is at 97.25° with 2c-O and 6c-Ti as shown in Figure 3.3a. In Figure 3.3a, there is only one Ag atom in the top layer, so there is less restriction upon Ag4 (bottom atom) to move toward 3c-O (5Ti), leading to the smaller angle; similar observations was also observed in the second most stable configuration. Therefore, when the Ag cluster becomes a 3-D structure, the top layer of the cluster may affect the Ag cluster adsorption by restricting the movement of bottom binding atoms. Besides, Ag1, Ag2, Ag3 and Ag4 in Figure 3.4a constitute the pyramid similar to Figure 3.3a, which suggests the Ag dimer, tetramer, and octamer can be used as the building blocks for larger size Ag clusters.

As the cluster size increases to eight, the HOMOs of the Ag clusters would cover more area of the surface and this broadens the ways of its interactions with the surface atoms. Hence, while not crucial in the binding tendency for Ag dimer, 3c-O (5Ti) also plays an important role in the Ag tetramer adsorption. In summary, the Ag dimer adsorption on the anatase TiO_2 (101) surface tends to be determined by the 2c-O with minor contribution from 5c-Ti. For Ag tetramer, the favored adsorption sites can be revealed by the maximum orbital overlaps of Ag tetramer and surface 2c-O/3c-O (5Ti) along with some contribution from 5c-Ti. In the case of Ag octamer, the favored adsorption sites can be suggested by the maximum orbital overlaps of Ag tetramer and surface 2c-O along with 5c-Ti's involvement. Also, surface 2c-O is suggested the favored nucleation centers for Ag clusters on the anatase TiO2 (101) surface.

Moreover, the binding tendency for Ag tetramer leads to an explanation for the geometry of the second most stable mode (2D to 3D). Consider the scenario of Ag3 lying on the same plane of Ag1, Ag2, and Ag4. In this layout, due to the repulsions between the Ag atoms, the ability of the tetramer to bind with 3c-O (5Ti) is mitigated, leading to orbital overlaps consisting of each Ag and 2c-O. However, as seen from the DP around -3.75eV in Figure 3.6d, movement of Ag3 to the top layer enables the orbital overlaps between Ag4 and the closest 3c-O (5Ti). This is also supported by the optimized angles of Ag4, 2c-O, and 6c-Ti: 97.95° compared to the initial angle of 103.44°. The interaction of Ag1 with two 2c-O atoms in the final configuration compensates for the loss of the interaction of Ag3 with one 2c-O in the initial configuration. Therefore, the final configuration not only possesses four bonding interactions with 2c-O, but also enhances the tetramer's bonding with 3c-O, allowing the maximum overlaps between orbitals of 2c-Os or 3c-O (5Ti) and HOMOs of the Ag tetramer. The orbital overlaps explain the geometry change and this is consistent with the work by Chretien and coworkers.[76] Note that

though Figure 3.3b has more number of Ag-O bonds than that in Figure 3.3a (6 vs. 5), the latter has shorter average distance (2.39 Å) than the former (2.46 Å). This suggests that bond distance is also an important factor in the Ag tetramer adsorption on the model surface.

For Pt Dimer, Tetramer, and Octamer, the P-DOSs of the most stable adsorption configuration of Pt dimer, tetramer, and octamer systems within the energy range of interest are given in Figure 3.7a-c. The resonant peaks suggest that Ti and O atoms possess similar inclinations to interact with the Pt clusters over the indicated energy range, with the peaks located mainly between the very top of the VB and the Fermi level of the system.

P-DOSs of surface 2c-O, 3c-O and total O atoms, and of surface 5c-Ti, 6c-Ti and total Ti atoms of the Pt dimer, tetramer, and octamer systems are shown in Figure 3.8a-f, respectively. 2c-O and 3c-O atoms show comparable interacting tendency to bind with the Pt clusters within the very top edge of the VB and Fermi level(see inset in Figure 3.8c), while 3c-O shows stronger inclination within most of the VB. In contrast, 5c-Ti and 6c-Ti generally show similar interacting tendency over the indicated energy span. Small exceptions are found within the bandgap of Pt tetramer and octamer systems, where 5c-Ti shows stronger binding tendency than 6c-Ti in the lower energy part of the bandgap, while reverse is true in the higher energy part of the bandgap.

Similarly, DPs (shown in Figure 3.7 and Figure 3.8) from selected resonant peaks of Pt dimer, tetramer, and octamer systems were studied to determine the key surface atoms interacting with Pt atoms. In Pt dimer system, 5c-Ti is the major atom to form bonding orbitals with Pt dimer (from DPs at -0.04eV in Figure 3.8a, -0.34eV, and -0.80eV in Figure 3.7a). 6c-Ti's contribution is missing for the reason mentioned earlier: the size, shape, or orientation restrictions of its atomic orbitals with respect to those of each HOMO of Pt dimer at each energy level, leading to insufficient orbital overlaps. This can be illustrated by examining the DP at -

1.02eV in Figure 3.8d; the shape and orientation of d_{z^2} orbital of 6c-Ti does not facilitate sufficient overlap with the orbital of Pt2 at that energy level. For the surface O atoms, 2c-O and 3c-O generally does not form bonding orbitals with Pt dimer. Only one was observed at -0.34eV and is from 2c-O's involvement. From the DP at -1.02eV, the orientation of the P orbital of 3c-O restricts its appreciable overlap with HOMO of Pt dimer. Therefore, though geometry observations reveal 3c-O and 6c-Ti's strong interactions with the dimer, they are not the key atoms to affect the dimer adsorption. We conclude that 5c-Ti(mainly) and 2c-O are key atoms for the Pt dimer adsorption consistent the work of Han and coworkers.[73]

In addition to 5c-Ti, 6c-Ti also contributes to bonding orbitals with the Pt tetramer. This can be seen in DPs around -0.81 eV and -1.78 eV in Figure 3.7b, which shows Pt3 and Pt4 forming bonding orbitals with 5c-Ti and 6c-Ti, respectively. As for the surface oxygen, bonding orbitals involved are primarily from 2c-O and is observed only in the second most stable adsorption configuration. From DPs at -0.05 eV, -0.25 eV, and -0.59 eV plotted in Figure 3.9, it can be seen that Pt1, Pt4, and Pt2 form bonding orbitals with 2c-O. This suggests that the geometry of the Pt tetramer is a factor of the formation of the bonding orbital. We attribute the missing bonding contribution of 3c-O to the reasons mentioned above, and illustrated with the DP at -1.62eV in Figure 3.8e. Compared to the HOMO of the Pt tetramer at that energy level, the horizontal atomic orbital of 3c-O prevents the substantial overlap, but facilitate 3c-O's bonding with the nearby 5c-Ti bonding atom. This also suggests that surface O contributes to the indirect bonding interaction through the neighboring bonding Ti atoms.

Like Pt tetramer system, bonding orbitals with Pt octamer mainly consist of 5c-Ti and 6c-Ti atoms as seen in DPs at -1.45eV in Figure 3.7c and around 0eV in Figure 3.8f, showing Pt5 bonding with 5c-Ti and 6c-Ti, respectively. 2c-O's contribution to the bonding orbital is not

common as seen in the top portion of the VB (DP at -2.41eV in Figure 3.7c), and 3c-O's contribution is not observed. Therefore, though the 3c-O (5Ti) atom seems to affect the Pt octamer adsorption from the geometry observations, in fact, its effect is not significant. While the Pt octamer does not interact with the support directly on the rutile TiO_2 (110) surface,[77] there is a direct interaction of the Pt atom in the top layer of the Pt octamer with the surface atom of anatase TiO_2 (101), as seen in DP at -0.16 eV in Figure 3.9d. The bonding interaction of Pt5 and 6c-Ti would extend the orbital of 6c-Ti toward the top layer. Thus a bonding orbital consisting of top layer atom (Pt6), Pt5 and the 6c-Ti is formed. This bonding participation would bring the top layer atoms close to the model surface. The distance between Pt6 and the 6c-Ti below was reduced from the initial 5.29 Å to 4.38 Å. This effect should also be considered as a factor in geometry change during the adsorption. This means that the atoms in the top layer would not only restrict the freedom of the binding atoms, but are also involved in the bonding with the surface atoms.

In summary, for Pt dimer, the binding favors maximum orbital overlap of Pt dimer with 5c-Ti and some contribution from 2c-O. For Pt tetramer/octamer, all surface Ti affect the cluster adsorption with minor contribution from 2c-O atoms. We suggest surface Ti atoms are the favored nucleation centers for Pt clusters on the anatase TiO2 (101) surface. Furthermore, with the derived binding tendency for Pt tetramer, the geometry evolution of the second most stable configuration (2D remains 2D) of the Pt tetramer can be explained using the DPs shown in Figure 3.9a-c. When the Pt tetramer lies on the surface, significant overlaps of its HOMOs with orbitals of the surface atoms easily formed without further change in the geometry. The difference between the second most stable configurations of Ag and Pt tetramer indicates that the

shape and orientation of the HOMOs of the metal cluster is a factor in determining the interaction behavior of the metal cluster on the model surface.

3.3.2 Issues Related to Catalysis and Photocatalysis

3.3.2.1 Encapsulation/Decoration

Encapsulation/decoration of metal nanoparticles reduces the catalytic property of the catalyst owing to occlusions of the deposited metal nanoparticles by the support during reduction at high temperatures. Encapsulation was observed for Pt/rutile(110) when temperature increased to 450K;[102] another study reported 270°C for the same system.[103] Pushkarev et al.[104] summarized several classic examples and a commonly accepted reason: the surface tension.

We consider one situation in which the cluster deposited on the support rotates and diffuses as the temperature is increased until one atom of the octamer intruding into the hollow site between the 2c-O atoms (see Appendix B, Fig. B4). Both Ag and Pt octamers were studied. The Ag octamer converged to the configuration similar to Figure 3.7, a & b, whereas the Pt octamer converged to the configuration corresponding to a rough model of the preliminary step for encapsulation, Figure 3.10, image 10. In this image, the oxygen atoms seem to start migrating onto the Pt octamer with an average distance increase of the 5c-Ti and 6c-Ti atoms from initial 2.90 Å to final 3.26 Å, indicating Pt octamer's tendency to peel the surface atoms. The Pt cluster has a strong tendency to bind with surface Ti atoms, so the bonds between surface Ti and O atoms would be weakened. The failure to see the reconstructed support surface in the Ag octamer case reveals that the encapsulation is likely to happen for the higher reactive metal clusters (high adsorption energy), Rh or Pt on CeO, TiO_2…etc.[105] and others.[104] NEB studies summarized in Figure 3.10 shows a possible pathway for rotation (Image 1-5) and diffusion (Image 5-9) of the deposited cluster when the temperature is increased. This pathway suggests that the temperature

increase facilitate mainly the rotation (an energy barrier estimated at 2.59 eV) and diffusion of the cluster on the support surface before encapsulation activation.

3.3.2.2 Sintering of Size Selected Ag and Pt Clusters

Sintering often occurs for metal clusters deposited on support material, resulting in a change in the size of the initially deposited clusters and this affects the catalytic reactions.[106] After depositing the size-selected ultra-small metal clusters on metal oxide surface, some of the clusters tend to aggregate to form larger clusters.[64, 65, 79, 107] For example, among Au_n^+(n=1-8), sintered clusters are found in the deposition of Au_1^+ on the rutile TiO_2 (110) surface at room temperature, which reveals Au monomer's high mobility on this surface.[64] On the same surface and temperature, among Ag_n^+(n=1-3), Ag monomer and dimer were also found to form sintered clusters.[65]

The low adsorption energy has been used to explain Au's high probability to form large clusters on step edges, and the observation of Pt monomer on the terraces of the anatase TiO_2 (101) surface.[79] In addition to the adsorption energy, the number of stable configurations (local minimums from the anatase TiO_2 (101) surface) is also suggested as an indicator of sintering tendency. A local minimum on the model surface suggests a site for the subnanometer cluster to adsorb on the surface. Large number of local minima indicate that there are many anchoring sites for such clusters, which reduce the mobility of the clusters and hence their agglomeration. The adsorption energies of two most stable configurations of the Ag and Pt dimer, tetramer and octamer, and the identified number of the local minima are reported in Table 1 incorporating previous results of Ag and Pt monomers and Pt trimer. [73, 80]

The number of local minimum of Ag dimer, 2, reveals that most of Ag dimers tend to diffuse and gather in those two areas on the model surface. On the contrary, the higher number of

Ag tetramer and octamer (7 and 4, respectively) indicate that these Ag clusters tend to anchor on more regions on the anatase TiO_2 (101) surface compared to the Ag dimer case. This reveals their mitigated mobility on the model surface, and less tendency for sintering. Among Ag monomer, dimer, tetramer, and octamer, Ag monomer and dimer have lower adsorption energies and lower numbers of local minima. The adsorption energy seems to form two groups: one group for monomers and dimers with lower adsorption energy, and the other group for tetramers and octamers with higher adsorption energy. The sintering probability of Ag clusters considered seems to reach a plateau with Ag tetramer. It can be suggested that when depositing ultra-small Ag clusters in the range of Ag monomer to octamer, it is very likely for Ag monomer and Ag dimer to sinter while the size of Ag clusters above tetramer is less likely to. Compared with the experimental work of Ag_n^+ (n=1-3) landing on rutile TiO_2 (110) surface, in which Ag monomer and dimer were found to sinter,[65] our evaluation give a reasonable prediction for the sintering tendency of Ag monomer and dimer on the anatase TiO_2 (101) surface. Likewise, Pt clusters of interest overall show higher adsorption energies than those of the Ag clusters and demonstrate another level of identified number of local minimum. Therefore, it can be suggested that there is less likelihood for their sintering except for Pt monomer.

3.3.2.3 Sub-Bandgap of Photocatalyst

The occurrence of metal induced states within the bandgap were reported in Ag and Pt subnanometer clusters on anatase or rutile TiO2 surfaces using PBE-PW/PBE-LOCA,[75] PW91-PAW,[81] PBE-PAW,[101, 108] and PW91-PW.[73] The number of the induced states within the bandgap is in proportion to the size of Pt clusters deposited on perfect and reduced rutile TiO_2(110),[81, 101] and the induced states would tend to form a continuous band as the cluster size increases from 1 to 8 atoms. In the case of a Pt cluster consisting of 37 atoms on the anatase TiO_2

(101) surface: a continuous band was detected. Muhich et al. suggested the continuous band leads to the formation of the recombination center for electron and hole pairs, which is detrimental to photoactivity.[109]

Our results of p-DOSs of Ag and Pt dimer, tetramer, or octamer (Figure 3.5 and 3.7) also show metal induced states within the bandgap. Furthermore, there appears to be a correlation between d-band center of the transition metal clusters and the formation of such induced states within the bandgap. The d-band center, the average energy of the metal valance d-bands, has been found to be a useful indicator for the adsorption energy of the adsorbates on 3d transition metals.[110] In Table 2, we report the d-band center of clusters in the gas phase and of clusters deposited on the model surface. Both sets of data show similar trends except for Pt tetramer case. This suggests that the d-band center of the deposited clusters is very similar to that of the clusters in the gas phase; the latter is easily obtained from low cost calculations.

Comparing the absolute d-band center of Ag and Pt clusters in the gas phase and the calculated bandgap value 1.9 eV (comparable to other reported value 1.94 eV[111]), the d-band centers of Pt clusters are smaller than or close to the bandgap value, while those of Ag are at most 1 eV off. This suggests that when the absolute value of d-band center is smaller than or close to the bandgap value, the d-band center is more shifted to the right, locating more likely within the bandgap and higher chance to induce those induced states. The lack of the induced states in Ag tetramer model is noticeable from this conclusion. The standard deviation (estimated as 2.5 half width for the d-band at half the maximum height) of the d-band of the cluster is also an indicator for the formation of the continuous band within the bandgap of the system. A low standard deviation suggests a tendency for the d states to locate around the d-band center. As shown in Table 2, larger standard deviations of the d-band centers of Pt group correlate with the

wider distributions of induced states within the bandgap. Those of Ag group have on average smaller values of standard deviation.

Examinations of the p-DOSs of surface O and Ti atoms of Ag clusters and Pt cluster models in Figure 3.6 and 3.8 reveal that the surface O and Ti atoms primarily contribute to the formation of the induced states within the bandgap. Looking at the p-DOSs of s, p, and d states of Ag and Pt octamers of the most stable configurations within the bandgaps as shown in Figure 3.11, it indicates the important role of d-states for such induced states. The d states are primarily involved in the formation of the induced states especially for Pt octamer. Observations of DPs located within the bandgap in Figure 3.7a-c suggest that the Pt d states primarily interact with the surface Ti atoms to form bonding orbitals, resulting in such induced states consistent with previous studies.[61, 112] These observations are consistent with using d-band center as indicator of the sub-bandgap formation. Note that the larger d-band centers of Pt clusters correlates with their d states locating closer to the Fermi level (within the bandgap), which increase the probability for Pt clusters to induce electronic states within the bandgap.

In summary, the formation of the induced states by Pt, Ag or other metal clusters within the bandgap of the model systems is indicated by the comparison between the bandgap value of the semiconductor and the absolute values of d-band centers of the clusters in the gas phase. If the d-band center is smaller than or close to the bandgap, it is very likely that the sub-bandgap states will exist.

3.4 Conclusions

The surface atoms that interact most with Ag cluster adsorptions on the anatase TiO_2 (101) surface are 2c-O and 3c-O atoms with a smaller contribution from 5c-Ti. Pt clusters tend to interact most with surface Ti with minor interaction with 2c-O. An important factor determining

the binding characteristic is the orbital overlap. Ag clusters tend to favor the sites where maximum orbital overlaps occur with the following combinations: 2c-O for dimer and octamer, and 2c-O/3c-O (5Ti) for tetramer along with the incorporation of the 5c-Ti. In case of Pt clusters the favored surface atoms are: 5c-Ti for dimers, and all surface Ti for tetramers and octamers with minor contribution from 2c-O. These represent 2c-O and Ti favored nucleation centers for Ag and Pt clusters, respectively, on the anatase TiO_2 (101) surface. We found tetramer as the structural transition size for 2D to 3D for both Ag and Pt clusters. The top layer of the octamers not only restricts the movement of atoms in the bottom layer to bind with the model surface, but also directly contributes to the interaction with the model surface. The stable geometry of the adsorbed Ag and Pt octamer is a parallelogram structure at the interface. The structure of the Ag and Pt dimer, tetramer, and octamer on the surface can be suggested as the building blocks for larger size clusters.

The behavior of Pt octamer on the anatase TiO_2 (101) surface was explored to gain insights into decoration/encapsulation of metal clusters deposited on support. A possible explanation is the tendency to achieve maximum orbital overlaps of the cluster and the surface atoms of the model surface. No reconstructed support surface was observed in the Ag octamer suggesting that encapsulation is likely to happen for more reactive metal clusters. NEB study suggests a possible pathway for encapsulation. When temperature is increased, the energy is used to overcome the energy barrier of rotation and/or diffusion of the clusters on the support. The adsorption energy and the number of stable cluster adsorption configurations suggest that Ag_n (n=1-3) have a tendency to sinter on the anatase TiO_2 (101) surface, while Ag_n (n=4-8) do not. On the same surface, Pt_n (n=2-8) do not have a tendency to sinter, Pt monomer being an exception. By comparing the bandgap of the semiconductor and d-band center of the cluster in

the gas phase, it is very likely that the sub-bandgap will be created for absolute values of d-band center smaller than or closer to the bandgap value. In addition, smaller standard deviation of the d-band center suggests the maintenance of the semiconductor nature of the subnanometer based photocatalysts.

The variation of the surface electronic structure is one factor determining the chemical and physical properties of the catalyst. Given a composite structure of the subnanometer metal cluster deposited on the semiconductor support, the d-band center shifts, leading to the formation of the sub-bandgaps and this in turn may allow photocatalytic reactions that utilize a larger fraction of photons in the solar spectrum. Investigations of the interactions of the subnanometer Ag and Pt clusters and the anatase TiO_2 (101) surface from a molecular point of view shed light on the behavior of subnanometer metal clusters deposited on the support. This will be useful in the design of promising subnanometer metal clusters based catalysts and photocatalyts.

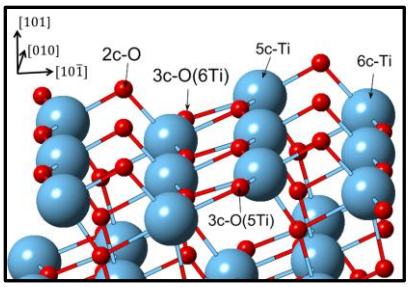

Figure 3.1 The perfect anatase TiO_2(101) surface, Ti and O are represented by blue and red, respectively.

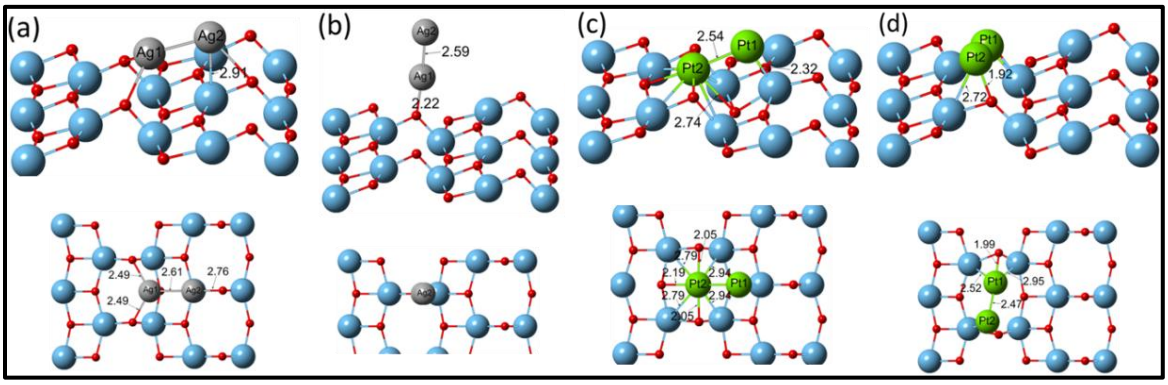

Figure 3.2 The most (1st) and second most (2nd) stable dimer adsorption configurations and their structural parameters on the anatase TiO_2(101) surface: (a)/(c) 1st and (b)/(d) 2nd stable Ag/Pt dimer systems, respectively(Ti in blue, O in red, Ag in silver and Pt in green).

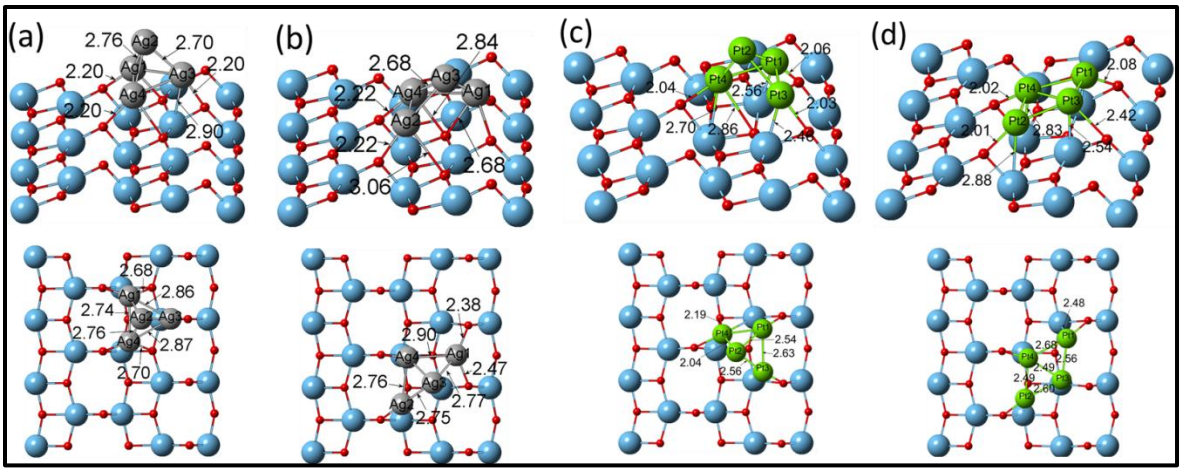

Figure 3.3 The most (1st) and second most (2nd) stable tetramer adsorption configurations and their structural parameters on the anatase TiO_2(101) surface: (a)/(c) 1st and (b)/(d) 2nd stable Ag/Pt tetramer systems, respectively(Ti in blue, O in red, Ag in silver and Pt in green).

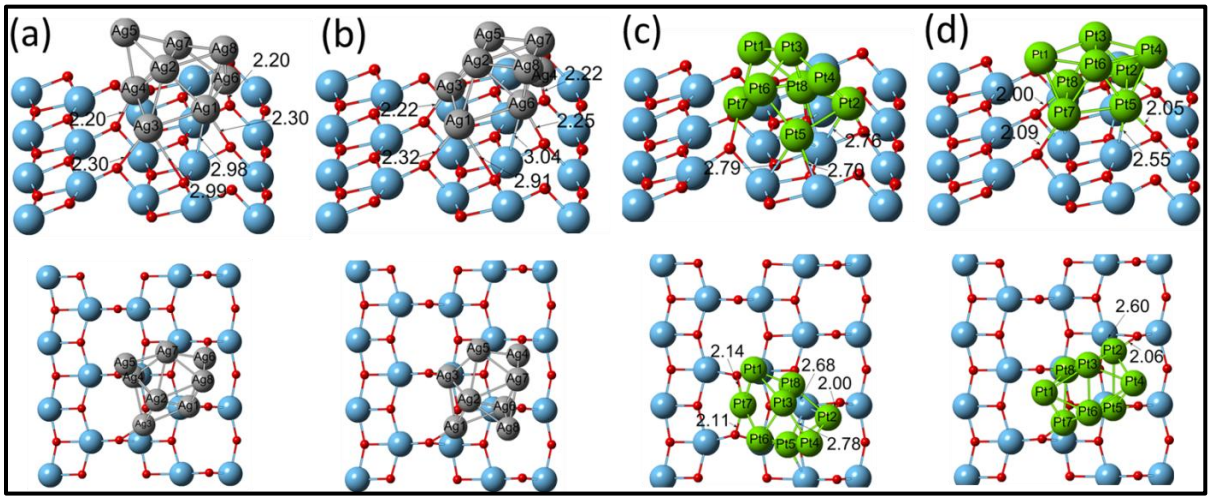

Figure 3.4 The most (1st) and second most (2nd) stable octamer adsorption configurations and their structural parameters on the anatase TiO_2(101) surface: (a)/(c) 1st and (b)/(d) 2nd stable Ag/Pt octamer systems, respectively(Ti in blue, O in red, Ag in silver and Pt in green).

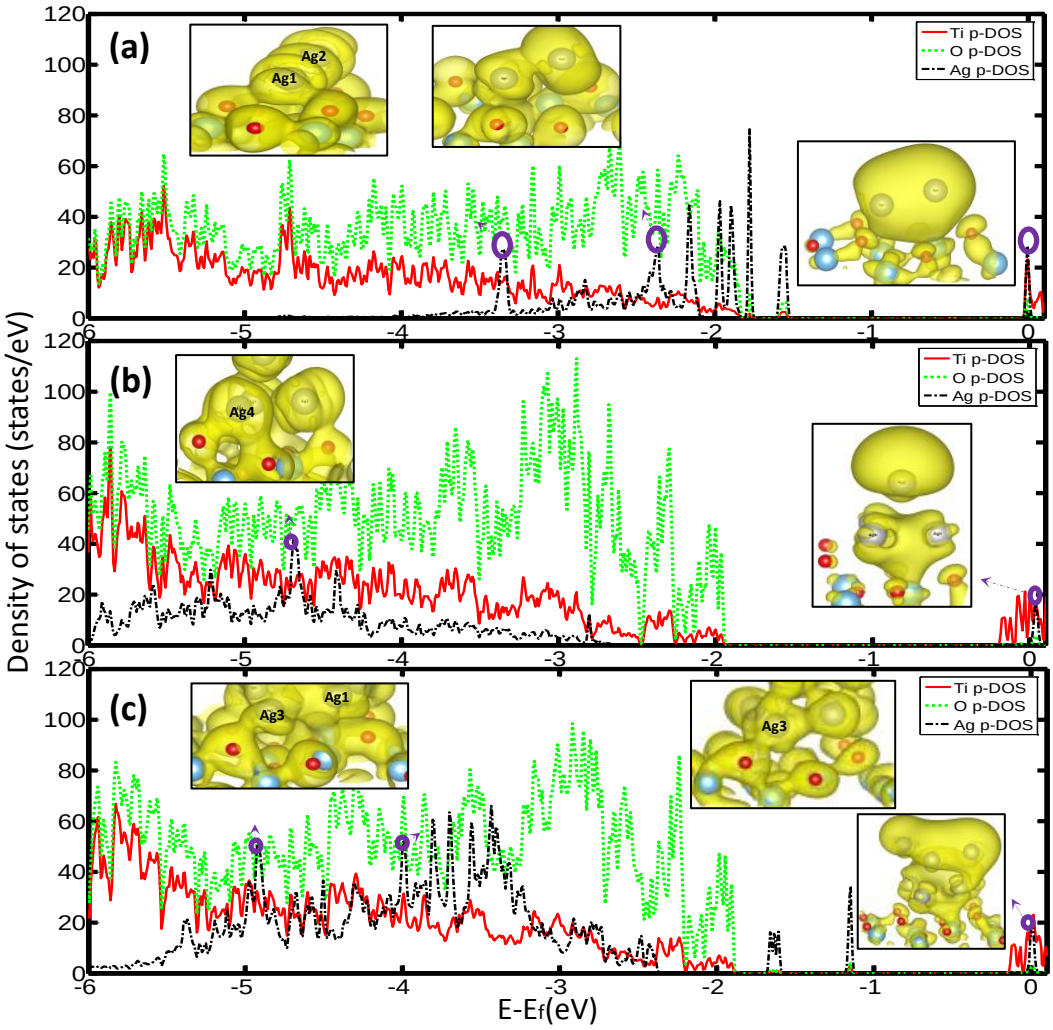

Figure 3.5 P-DOSs (Ti, O, and Ag) & density plots of the most stable adsorption configuration of Ag clusters: (a) dimer, (b) tetramer, and (c) octamer. The inset shows the density plots at corresponding positions: (a) 0, -2.41, and -3.45eV, (b) 0 and -4.7eV, and (c) 0, -4.0, and -4.9eV.

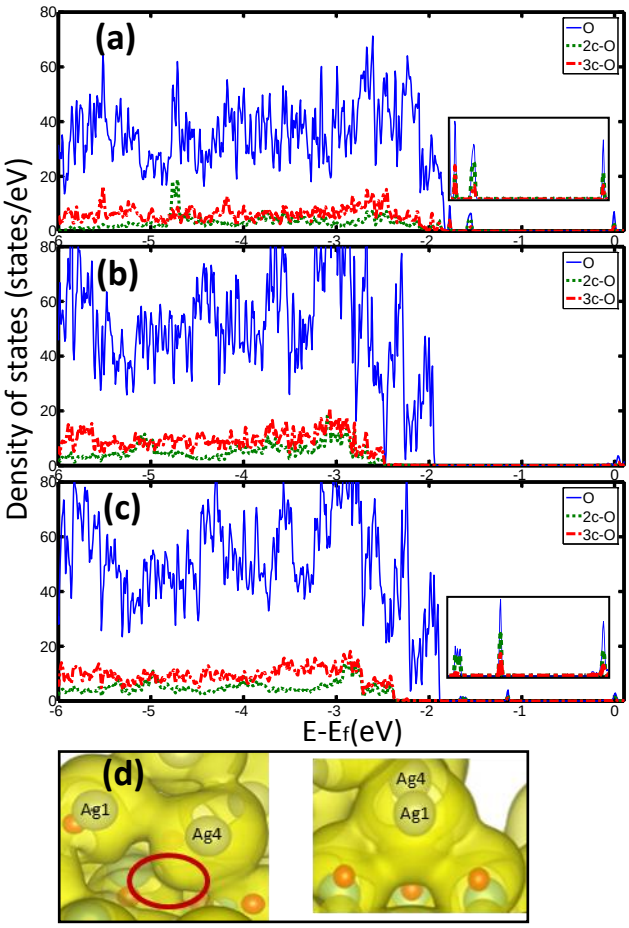

Figure 3.6 P-DOSs (surface 2c-O, 3c-O and total O) of the most stable adsorption configuration of Ag clusters: (a) dimer, (b) tetramer, and (c) octamer. (d) Density plot at -3.75eV of the second most stable Ag tetramer adsorption configuration. The inset shows the detailed p-DOSs within the bandgap.

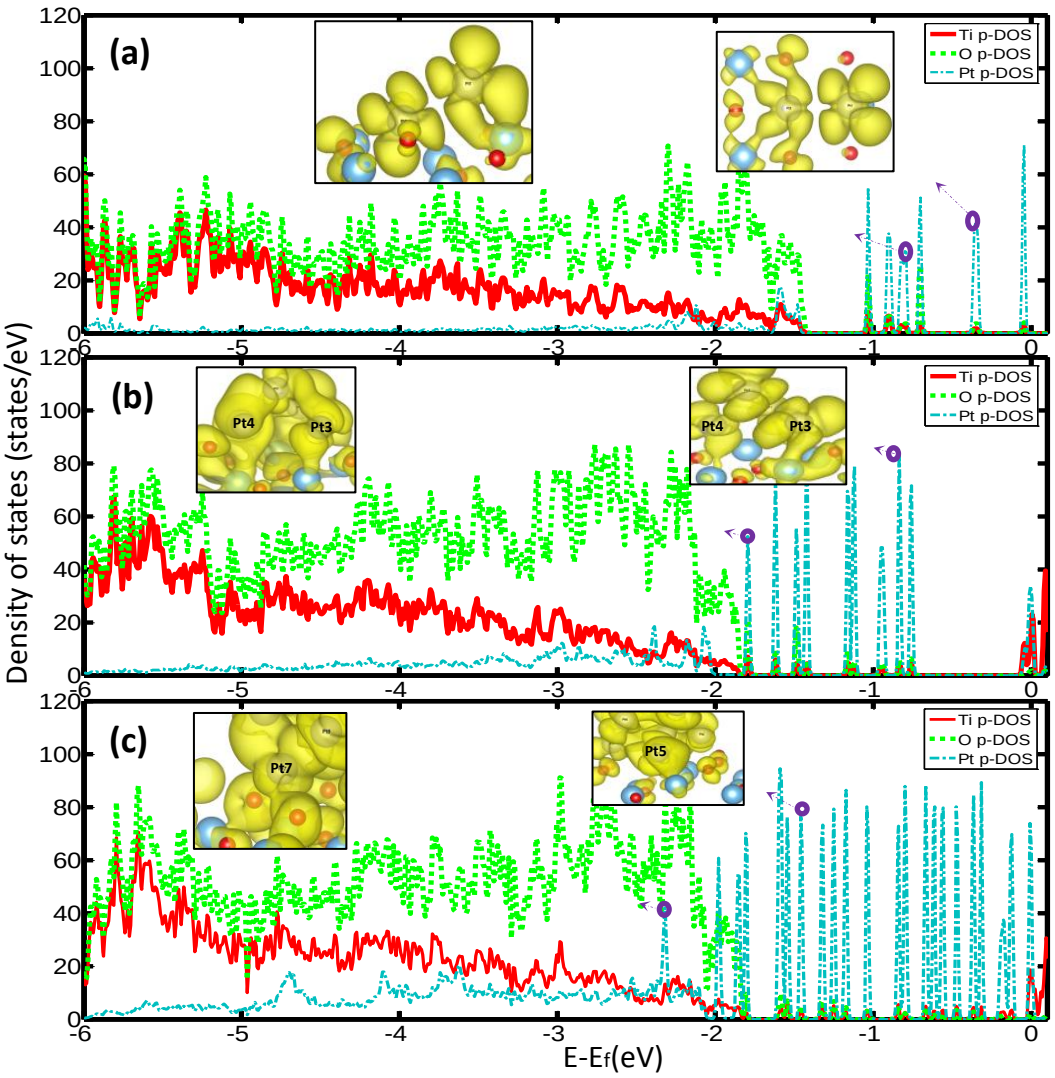

Figure 3.7 P-DOSs (Ti, O, and Pt) & density plots of the most stable adsorption configuration of Pt clusters: (a) dimer, (b) tetramer, and (c) octamer. The inset shows the density plots at corresponding positions: (a) -0.34 and -0.80eV, (b) -0.81 and -1.78 eV, and (c) -1.45 and -2.41eV.

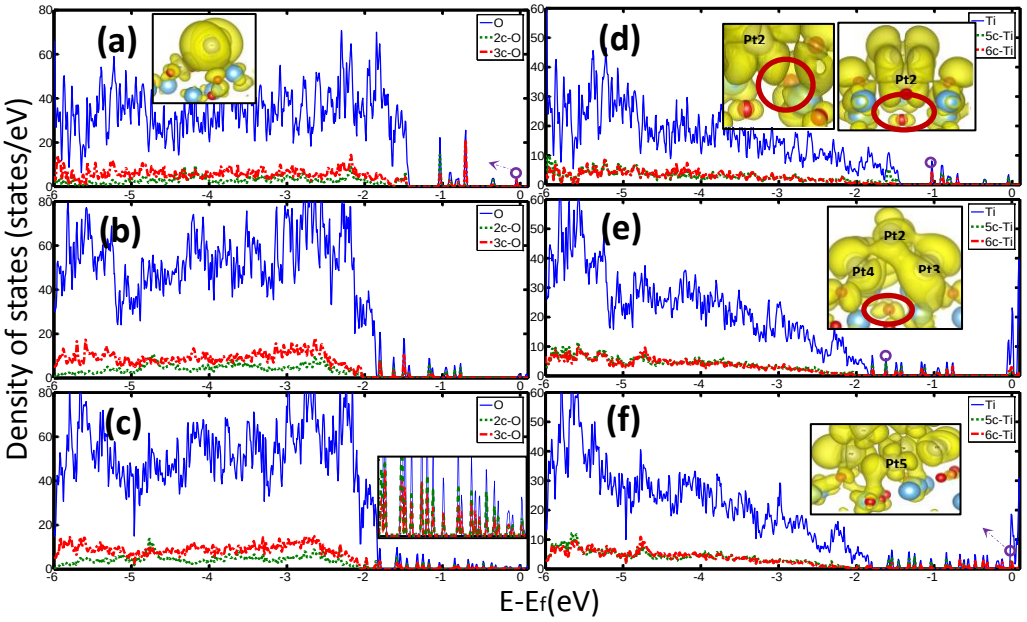

Figure 3.8 P-DOSs & density plots of the most stable adsorption configuration of Pt clusters: surface 2c-O, 3c-O and total O of (a) dimer, (b) tetramer, and (c) octamer; surface 5c-Ti, 6c-Ti and total Ti of (d) dimer, (e) tetramer, and (f) octamer. Density plots at corresponding positions are presented in the insets of (a) 0.04eV, (d) -1.02eV, (e) -1.62eV, and (f) 0eV. The inset in (c) shows the detailed p-DOSs with the bandgap.

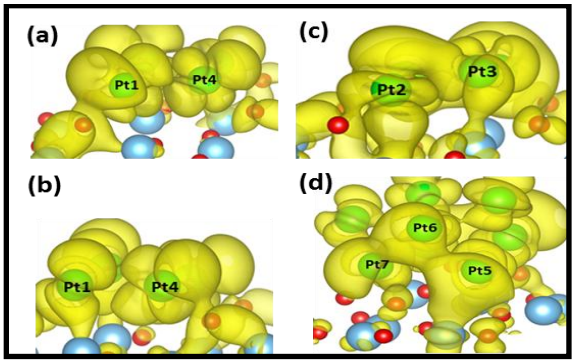

Figure 3.9 Density plots of the second most stable Pt tetramer configuration at (a) -0.05eV, (b) -0.25eV, and (c) -0.59eV, and of the most stable Pt octamer configuration at (d) -0.16eV.

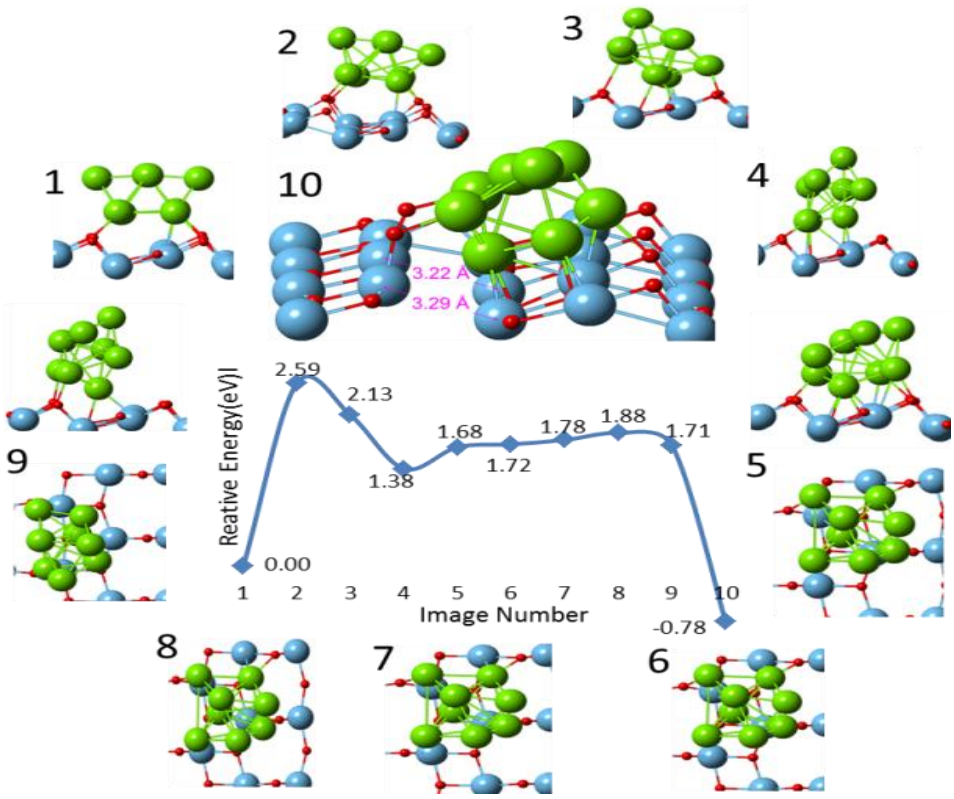

Figure 3.10 A possible pathway for the encapsulation from a stable Pt octamer adsorption configuration (Image 1). Image1 - 5 and 5 - 9 represents rotation and diffusion, respectively. Image 10 is the crude model of the early step of encapsulation (Image 9 is a relaxed configuration of the assumed initial configuration).

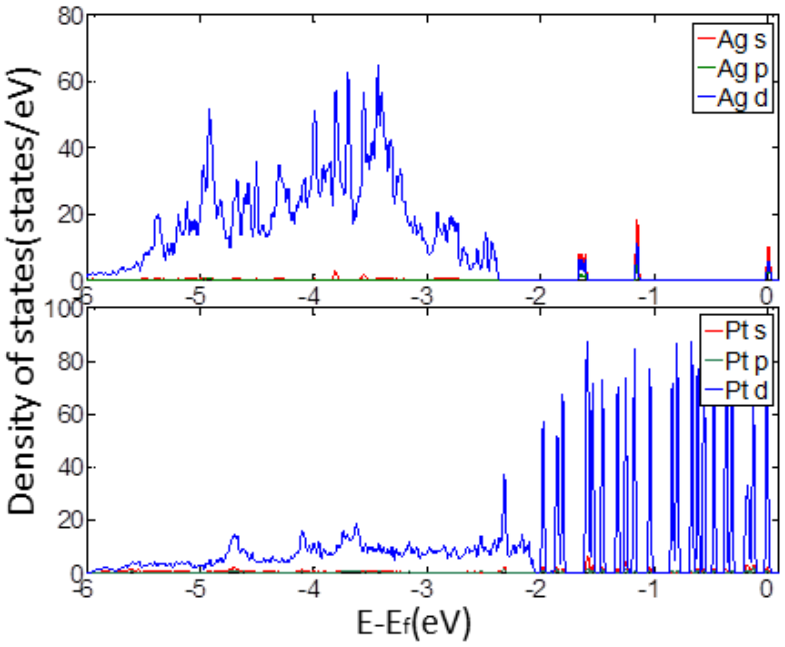

Figure 3.11 P-DOSs of the adsorbed Ag (top) and Pt (bottom) octamers in the most stable Ag and Pt octamers adsorption configurations.

Table 3.1 Adsorption energy of the first two stable configurations of Ag and Pt clusters on the anatase TiO_2(101) surface, and the number of local minimum in each system.

	Monomer		Dimer		Trimer	Tetramer		Octamer	
	Ag	Pt	Ag	Pt	Pt	Ag	Pt	Ag	Pt
Adsorption energy of 1st/2nd (eV)	-0.70[a] / -0.13[a]	-2.84[b] / -2.25[b]	-0.70/ -0.45	-2.87/ -2.35, -2.67[b] / -2.53[b]	-3.08[b] / -2.99[b]	-1.49/ -1.44	-4.29/ -3.94	-1.30/ -1.28	-4.10/ -3.97
Number of local minima	2[a]	3[b]	2	5, 6[b]	6[b]	7	7	4	4

[a] MS CASTEP GGA/PW91.[80] [b] VASP GGA/PW91.[73]

Table 3.2 d-band center and standard deviation of d states of the Ag and Pt clusters in the gas phase and deposited on the model surface.

	Ag d-band center (eV) (Standard deviation)		Pt d-band center (eV) (Standard deviation)	
	Free	Deposited	Free	Deposited
Dimer	-2.21(0.50)	-2.46(0.72)	-1.18(1.31)	-2.05(2.07)
Tetramer	-3.20(0.70)	-4.91(0.97)	-1.81(1.49)	-2.66(1.92)
Octamer	-3.02(0.76)	-4.01(0.88)	-2.05(1.52)	-2.32(1.80)

CHAPTER 4: CO_2 ADSORPTION ON ANATSE TIO_2 (101) SURFACES IN THE PRESENCE OF SUBNANOMETER AG/PT CLUSTERS: IMPLICATIONS FOR CO_2 PHOTOREDUCTION[113]

This chapter summarizes the investigations of CO_2 adsorption on subnanometer Ag & Pt clusters/ TiO_2 surfaces to gain understandings of clusters based photocatalysts for CO_2 reduction. Using Density Functional Theory calculations, we show how CO_2 adsorption on perfect and reduced anatase TiO_2 (101) surfaces can be substantially modified by the presence of surface Ag and Pt octamer clusters. We find that adsorption is affected even at sites where the adsorbate is not in direct contact with the octamer, which we attribute to charge donation to CO_2 from the Ag/Pt-modified surface, as well as an electrostatic competition between attractive (Ti-O) and repulsive (Ti-C) interactions. In addition, TiO_2-supported Pt octamers offer key advantages that could be leveraged for CO_2 photoreduction, including providing additional stable adsorption sites for bent CO_2 species and facilitating charge transfer to aid in CO_2^- anion formation. Electronic structure analysis suggests these factors arise primarily from the hybridization of the bonding molecular orbitals of CO_2 with d orbitals of the Pt atoms. Our results show that for adsorption on TiO_2-supported Pt octamers, the O-C-O bending and C-O asymmetric stretching frequencies can

---

Reprinted with permission from {Yang, C.-T.; Wood, B. C.; Bhethanabotla, V.; Joseph, B., CO_2 Adsorption on Anatase TiO_2 (101) Surfaces in the Presence of Subnanometer Ag/Pt Clusters: Implications for CO_2 Photoreduction. *The Journal of Physical Chemistry C* 2014, *118*, 26236-26248.}. Copyright {2015} American Chemical Society." (Refer to Appendix A)

be used as reliable indicators of the presence of the CO_2^- anion intermediate, as well as to distinguish unique adsorption geometries or sites. Finally, we suggest a possible pathway for subsequent CO_2 dissociation to CO at the surface of a reduced anatase TiO_2 (101)-supported Pt octamer, which has a computed energy barrier of 1.01eV.

4.1 Introduction

Ever since Fujishima and Honda first demonstrated the use of TiO_2 electrodes for photocatalytic water splitting in 1972,[114] numerous researchers have extended the idea to applications such as photocatalytic degradation of environmental harmful species,[115] and photoreduction of CO_2 into light hydrocarbons.[116] However, the efficiency of the photo-conversion remains a weakness.[7] One technique to improve the photo-efficiency is to deposit noble metal nanoparticles on the semiconductor surface.[18, 70] The nanoparticles serve as cocatalysts to reduce the recombination of e-/h+ pairs, or as plasmonic particles to increase the concentration of photoexcited electrons.[71, 72] However, cost is a concern for this technique; for example, Pt has proven to be an effective cocatalyst but is expensive and limited in supply. Doping the semiconductor with elements such as N[9, 10] and Ag[11] and introducing surface defects are other techniques for improving the photo-efficiency by reducing the bandgap, but they also increase the chances for recombination of e-/h+ pairs.[117]

The addition of subnanometer metal clusters consisting of several atoms represents an alternative strategy that can substantially reduce the materials requirements associated with larger cocatalyst particles. Such clusters have shown enhanced catalytic activity for a variety of reactions such as direct propylene epoxidation,[21] CO oxidation,[23, 25, 118] and oxidative dehydrogenation of propane.[26] The promotional effects are attributed to the dynamic structural fluxionality,[118] larger fraction of under-coordinated surface atoms,[26] and the interactions between

deposited cluster and the support.[28] In addition, such clusters can potentially introduce extra electronic states within the bandgap (sub-bandgap states) of the semiconductor, thereby reducing the optical absorption gap.[73, 74, 119, 120]

While TiO_2 may not prove to be the optimal catalyst for CO_2 photoreduction, TiO_2-based materials continue to provide common settings to understand the chemistry of CO_2 photoreduction.[121] One proposed mechanism starts with the absorption of an incident photon to form Ti^{3+}- O^- sites, followed by the interaction of the Ti^{3+} atoms with CO_2 to form CO_2^-, the latter being the first and key step of the reduction mechanism.[1, 7] The adsorbed CO_2^- then reacts with an H· radical to generate CO, HCO_2H, CH_2CO, CH_3OH, and CH_4. The success of the key step (reduction of CO_2 to CO_2^-) relies on the geometry with which CO_2 is adsorbed on the TiO_2 surface: the more bent the geometry of the adsorbed CO_2 molecule, the easier the transfer of photoexcited electrons to CO_2 to form the CO_2^- anion.[122-124] This is due to the decrease of the CO_2 LUMO energy as the O-C-O bond angle decreases.[125] Prior quantum mechanical calculations have investigated CO_2 adsorption on the electronic ground or excited states of different surfaces of TiO_2 clusters.[123, 126, 127] More thorough studies have considered CO_2 adsorption on periodic TiO_2 anatase (101) surfaces, including the effect of oxygen vacancies or interstitial Ti atoms at surface or subsurface sites.[122, 128]

In this article, we extend previous work by using density functional theory (DFT) to examine the interplay between CO_2 adsorbates and anatase TiO_2 (101) surfaces in the presence of subnanometer Ag & Pt clusters, which we represent by octamers. The choice of surface was motivated by the fact that anatase is the dominant crystal structure of TiO_2 in a commercial Degussa P25 photocatalyst (80% anatase and 20% rutile), and the (101) surface is the most stable anatase surface.[82] In addition, scanning tunneling microscopy (STM) points to the existence of

various point defects such as oxygen vacancies, hydroxyl groups, and interstitial atoms, which may bring important effects to the interaction between the surface and the metal clusters;[79] accordingly, we consider the possible presence of a surface oxygen vacancy (i.e., reduced surface) in addition to the pristine anatase surface.

Specifically, we frame our discussion according to four basic ingredients for designing an effective CO_2 photoreduction catalyst (focusing here on the formation of key reaction precursors): (i) availability of binding sites, (ii) intermediate adsorption energy at those sites (too strong = traps; too weak = inactive), (iii) bent geometry of CO_2, and (iv) localized charge transfer to CO_2 to facilitate CO_2^- formation. We investigate the impact that adding Ag and Pt clusters to anatase surfaces has on each of these four factors. The geometry and energetics of CO_2 adsorption are first examined in detail using electronic structure techniques. The CO_2 adsorption modes are then correlated with calculated vibrational frequencies to provide a roadmap for interpreting and characterizing IR spectra. Finally, a possible dissociation mechanism of CO_2 to CO (in its precursor state) on one of our tested surfaces is discussed. This understanding is intended to guide the design of promising subnanometer metal cluster/semiconductor catalyst frameworks for CO_2 photoreduction.

4.2 Computational Methods

Titanium atoms on the anatase TiO_2 (101) surface consist of 5-fold(5c-) and 6-fold(6c-) coordinated Ti atoms, whereas the surface oxygen atoms comprise 2-fold(2c-) and 3-fold(3c-) coordinated O atoms. The 3c-O atoms can be further decomposed into 3c-O between 5-fold coordinated Ti and between 6-fold coordinated Ti atoms.[78, 119] In order to compare with the corresponding literature results,[122, 128] the reduced surface is modeled by removing an oxygen atom from a bridge site (2c-O), resulting in conversion to 4c-Ti and fewer exposed 5c-Ti atoms.

The stable configurations of perfect and reduced surface supported Ag and Pt octamers were obtained by following the procedures from our previous work.[119]

The DFT calculations were performed with the Perdew–Burke–Ernzerhof (PBE) functional of the generalized gradient approximation (GGA)[90] using the VASP (Vienna Ab Initio Simulation package) code.[87-89] The electron-ion interactions were modeled by the projector-augmented wave (PAW)[91] method. A kinetic energy cutoff of 500 eV was used for the wavefunctions, and energies were converged to 10^{-5} eV. Spin polarized calculation was incorporated in the geometry optimization, with the force convergence criteria on each atom set to < 0.01 eV/ Å. It is known that the bandgap of transition metal oxides is underestimated with the standard DFT due to its improper self-interaction cancellation built in, leading to inability to accurately model the strongly correlated localized 3d electrons of the Ti atoms. This, for example, fails to describe small electron-polarons formed on the anatase (101) surface, particularly on the reduced surface.[129, 130] DFT+U approach is suggested to improve such localization deficiency. A test with DFT and DFT+U was done on Bader charge of configurations of CO_2 adsorbed on reduced surface reported in this research (refer to Appendix B, Fig. B5 and Table B1). The value of U=3.5 eV is chosen according to the literature[128] which gives comparable results to the experimental values. The effect of different U vales is tested following the work of Park et al.[131] It is shown that the charge distribution is comparable under both approaches for these two configurations. Some prior studies have also shown that for transition metal clusters[132, 133] or adsorbates[134] adsorbed on the perfect or reduced TiO_2 surfaces, the trends of the charge distribution and cluster stability are similar with DFT and DFT+U methods. Nevertheless, the results in this study from standard DFT should be taken with a word of caution due to limitations of standard DFT calculations.

A 3x1 supercell of the anatase TiO_2 surface with six trilayers was considered. Among the six trilayers, the bottom three layers were frozen, while the top three layers and metal clusters were allowed to relax. A Monkhorst-Pack [93] mesh of 2x2x1 k-points was used to sample the Brillouin zone for determining the adsorption geometry of CO_2 on the model surfaces; this was increased to 6x6x1 for the density of states (DOS) calculations. The vacuum region between the slabs was set to 12 Å. The adsorption energy of CO_2 was calculated as the difference between the total energy of the CO_2 adsorbed on the model surfaces, and the sum of energies of the isolated CO_2 and model surfaces. Within this definition, a more negative adsorption energy indicates more favorable adsorption.

To study the electronic structure of the interactions of CO_2 with the model surfaces, we computed atom-projected densities of states (p-DOS) within the energy range of interest (from the level of the bonding molecular orbitals of CO_2 to 1 eV above the Fermi level), as well as density plots (DPs) with equal-density isosurfaces of 0.001e/ $Å^3$. The zero energy position in each p-DOS figure within this work corresponds to the Fermi level. Charge population changes upon CO_2 adsorption on the model surfaces were analyzed using Bader charge analysis.[135] The climbing image nudged elastic band method (CI-NEB)[98-100] (Γ point sampling and spin restricted) was used to investigate the mechanism of CO_2 dissociation to CO. The vibrational frequencies were calculated using the frozen-phonon approach with a displacement of 0.015 Å for the C and O atoms of the CO_2 molecule.

4.3 Results and Discussion

4.3.1 CO_2 Adsorption on TiO_2 Surfaces

We begin with a discussion of CO_2 adsorption on perfect and reduced anatase TiO_2 (101) surfaces without Ag or Pt clusters. On the perfect anatase TiO_2 (101) surface, three CO_2

adsorption modes were identified: one linear (L1) and two bent (B1, B2) forms; on the reduced surface (Vo), six modes were obtained: one linear (LVo1) and five bent (BVo1-BVo5) forms. Among the adsorption modes, B1, B2, and BVo5 were found to be slightly metastable. The optimized geometries and corresponding structural parameters are given in Fig. B6 of Appendix B. Table 1 shows the corresponding adsorption energies, O-C-O angles of CO_2, and changes in the Bader charge of the CO_2 molecule and of its central C atom. Our computed configurations are almost the same as those reported by He et al. (using VASP with the PBE functional)[122] and by Sorescu et al. (using VASP with PBE with corrections for the long-range dispersion interactions).[128] Compared to the results obtained by He et al.,[122] the trends in the adsorption energy and structural parameters for binding on the perfect surface are the same, though our adsorption energies are a bit weaker; this may be due to a different convergence criterion and supercell size. Compared to the study by Sorescu et al.,[128] our converged configurations and the trends in the adsorption energy on both perfect and reduced surfaces are also quite similar, except for BVo4, for which we obtained a somewhat larger O-C-O angle. Note that the adsorption energy of LVo1 is comparable to the corresponding one reported by Wanbayor et al.,[136] and the NEB and MD simulation suggested the desorption of CO_2 from the reduced anatase TiO_2 surface at room temperature. It is revealed that CO_2 adsorption configurations reported in this research with adsorption energies around or below that of LV_01 may desorb under realistic conditions.

Comparing the energies in Table 1 to the geometries in Fig. B6 of Appendix B reveals site-specific trends of the binding mechanism. The O atom in CO_2 tends to bind with surface Ti atoms, whereas the C of CO_2 tends to bind with surface O atoms. Specifically, on the perfect surface, the preference is for the O atom of CO_2 to bind with 5c-Ti, while on the reduced surface

it also binds with 6c-Ti. The latter effect is likely due to the greater exposure of 6c-Ti surface sites in the presence of the oxygen vacancy, which results from the vacancy-induced modification of the local surface structure. The O atom's tendency to bind with both 5c-Ti and 6c-Ti on a reduced surface is best illustrated by BVo1, in which it binds to both sites simultaneously; this is also the most energetically favorable of all of our tested configurations. The C atom in CO_2 favors binding with 2c-O and 3c-O (5Ti) on the perfect surface, whereas on the reduced surface 3c-O (6Ti) also becomes possible (e.g., BVo3, for which the C-to-3c-O binding distance is 1.41Å).

On average, the introduction of oxygen vacancies appears to have two key effects on CO_2 adsorption: first, it increases the number of possible CO_2 binding configurations; and second, it enhances the adsorption strength on the surface. This second point is particularly evident when comparing the metastable B2 with the highly stable BVo2, which is analogous except for the removal of a bridging oxygen. The oxygen vacancy helps stabilize CO_2 adsorption in BVo2, likely because CO_2 gains electron density from the oxygen vacancy (0.088e). We emphasize that the negative charge accumulation at the C of CO_2 is crucial to the formation of the CO_2^- anion for CO_2 photoreduction,[122] and is particularly pronounced for BVo1 and BVo4 (0.827e and 0.421e, respectively). However, it takes energy to create oxygen vacancies, and this reveals the importance of subnanometer clusters which will be discussed below.

4.3.2 CO_2 Adsorption on TiO_2 Supported Ag/Pt Octamers Surfaces

Next, we discuss how the adsorption properties of CO_2 are affected by the presence of the Ag and Pt octamers on anatase TiO_2 (101), focusing on structural and electronic properties, the CO_2 binding mechanism, and the associated vibrational properties. Particular attention is paid to two factors that are directly relevant for catalytic activity: first, the availability of viable surface

binding sites for CO_2; and second, the bent geometry and charge accumulation on the adsorbate, which together facilitate CO_2 activation. Note that some reconstruction of the octamer occurs during CO_2 adsorption on both perfect and reduced surfaces; this is due to the fluxionality characteristic of the subnanometer metal cluster, which was discussed in our previous work on the adsorption of Ag and Pt dimers, tetramers, and octamers on the anatase TiO_2 (101) surface.[119]

4.3.2.1 Structural and Electronic Properties

For Pt/Ag on perfect anatase (101) surface, we begin by considering CO_2 binding on perfect (vacancy-free) anatase (101) surfaces with Ag and Pt octamers. The optimized configurations and structural parameters of CO_2 adsorption for this case are given in Figure 4.1. The adsorption energy, O-C-O angle of CO_2, and Bader charge difference of the CO_2 molecule upon adsorption for each of the configurations of Figure 4.1 are reported in Table 2. In the presence of the Ag octamer, two bent (BA1 and BA2) and one linear (LA1) CO_2 adsorption modes were found, as shown in Figure 4.1a-c. In the presence of the Pt octamer, four bent (BP1-BP4) and one linear (LP1) CO_2 adsorption modes were found, as shown in Figure 4.1d-h. The adsorption configurations can be broadly classified into two categories: those where CO_2 binds directly to the TiO_2 surface itself (BA2, LA1, BP4, LP1); and those where CO_2 interacts appreciably with the metal cluster (BA1, BP1, BP2, BP3).

For adsorption at TiO_2 sites (with octamer present), a comparison of Tables 1 and 2 makes it clear that the presence of Ag and Pt octamers affects CO_2 binding even when there is no direct contact between the adsorbate and the metal clusters, i.e., when binding is directly on TiO_2 surface sites (BA2, LA1, BP4, LP1). Moreover, the effect of the Ag & Pt octamers on CO_2 adsorption at these sites varies depending on the orientations of the CO_2 molecule.

To see this, consider the linear modes, LA1 & LP1 (Figure 4.1, c & h) and the bridge carbonate-like modes, BA2 & BP4 (Figure 4.1, b & g), which are similar to one another in terms of O-C-O angles of CO_2 and binding distances. In comparison with analogous modes on the perfect surface without Ag/Pt (L1 and B2 in Fig. B7, a & c in Appendix B), the linear LA1 and LP1 have longer bond lengths between the O atom of CO_2 and the surface Ti atom by up to 0.2 Å (Fig. B7 in Appendix B and Figure 4.1), as well as weaker adsorption energies (refer to Table 1 & 2). Conversely, the presence of Ag or Pt octamers stabilizes the metastable bent B2 configuration, strengthening adsorption for the stable BA2 and BP4 bent configurations (which have nearly identical structural parameters).

The Bader charge analysis in Table 2 indicates that the additional negative charge accumulated on the binding O atom of CO_2 for LA1 (0.026e) and LP1 (0.061e) sustains binding with the surface Ti atom, similar to the value found for L1 on the undecorated surface (0.033e). BA2 and BP4 also show net significant electron accumulation in both O atoms of CO_2 upon binding. However, though qualitatively consistent with B2 on the undecorated surface (Table 1), the magnitude of this accumulation is much greater for BA2 and BP4. Moreover, the electron accumulation on the O atoms of CO_2 for BA2 and BP4 is not accompanied by any significant electron depletion on the C atom, indicating charge is being transferred from the substrate rather than internally redistributed within the CO_2 molecule. This behavior may explain the transformation from the metastable B2 to stable BA2 and BP4 upon addition of Ag/Pt. The localized net charge at both O atoms of CO_2 facilitates binding with the surface Ti atom, which agrees with the result reported by He and coworkers.[122] The enhanced electron density in the CO_2 adsorbate derives from the tendency of Ag & Pt octamers to donate electrons to the anatase (101) surface: our previous work suggests that Ag and Pt octamers have the tendency to donate

electron to the anatase (101) surface (1.075 and 0.450e).[119] Similar trends have also been observed on model surfaces of Pt dimers on rutile TiO_2 (110)[108], Ag(2,4,8) on anatase (110)[137], and Pt(1-3) on anatase (101)[73]. The enhanced CO_2 adsorption phenomenon is similar to the observation that O_2 adsorption on stoichiometric rutile TiO_2 (110) becomes favored when electronic density is transferred from deposited small Au clusters to the oxide.[76]

For adsorption at sites associated with octamers, the examination of the sites for which CO_2 binds in direct contact with the Ag/Pt octamers (BA1, BP1, BP2, BP3) reveals two additional facts. First, we find that the presence of the Pt octamer exposes more additional CO_2 adsorption sites than does the presence of the Ag octamer (three for Pt vs. one for Ag). Second, CO_2 tends to adsorb rather strongly on the Pt site.

BA1 (Figure 4.1a) is the sole Ag octamer-associated CO_2 adsorption site, in which CO_2 binds at the interface between the Ag octamer and the TiO_2 surface with a distance of 2.26 Å between O(a) and the nearest Ag atom. Compared to analogous modes without the octamer (B1 in Fig. B7 in Appendix B), there is an increase of the C-O bond length in CO_2 by 0.04 Å; the O-C-O angle of CO_2 is also smaller. The elongation is attributed to the interaction of the Ag octamer with CO_2, indicated by increased charge transfer to O(a) for BA1 (0.072e) compared to B1 (0.042e). The additional charge transfer also explains the increase in adsorption strength by 0.33eV, and reveals the Ag octamer's role in stabilizing CO_2 on the surface in this mode.

The three additional CO_2 adsorption sites provided by the Pt octamer for bent-form CO_2 are BP1-BP3 (Figure 4.1d-f). BP1 represents CO_2 adsorption at the interface edge of the Pt octamer and TiO_2 surface. In this configuration, CO_2 binds with 5c-Ti using one of its O atoms, while using C and the other O to bind with the Pt octamer. On the other hand, in BP2 and BP3, CO_2 adsorbs solely on the Pt octamer, with no direct interaction with the anatase surface; notably,

these configurations are unique to Pt, with no analog for Ag. In BP2, the C atom of CO_2 bridges two Pt atoms, each of which also interacts with a different O atom of CO_2. In BP3, the CO_2 molecule uses C and one O to bind with one Pt atom.

On average, adsorption on the three Pt sites is stronger than on the surface with supported Ag octamers or on the clean perfect anatase surface, which means that the supported Pt octamer surface will tend to enrich the adsorbed CO_2 species. Moreover, BP1, BP2, and BP3 show a tendency for significant negative charge accumulation in the C atom of CO_2 (0.599, 0.537, and 0.374e, respectively), which is favorable for formation of the CO_2^- anion. The charge accumulation can also be easily observed in the charge density difference of BP1 and BP2 (see Fig. B8 in Appendix B). Note that the O-C-O angle of CO_2 decreases as the net charge transfer and the adsorption strength increase. In fact, the O-C-O angles of adsorbed CO_2 in BP1 and BP2 are close to the reported angles of the CO_2^- anion based on experimental and theoretical results, 127±8° and 138°, respectively.[122] We point out that the C atom's acquisition of additional negative charge is similar to the electronic behavior of adsorption modes found on clean perfect Zn_2GeO_4 (010) and (001) surfaces.[138] This reveals that depositing subnanometer metal clusters can bring new electronic properties to a conventional photocatalyst such as TiO_2, and that a Pt octamer deposited on perfect anatase (101) has the capability to activate the CO_2 molecule. Notably, this behavior contrasts with CO_2 adsorption modes on clean perfect anatase TiO_2 (101)[122], perfect brookite (210)[139], and perfect ceria (110)[140] where no stable bent form of CO_2 or net charge accumulation on C upon adsorption were found.

For Pt/Ag on reduced anatase (101) surface, we consider CO_2 binding on reduced anatase (101) surfaces (i.e., oxygen vacancy) with Ag and Pt octamers. Identified CO_2 adsorption configurations and corresponding structural parameters for this case are given in Figure 4.2. The

adsorption energy, O-C-O angle of CO_2, and Bader charge difference of the CO_2 molecule upon adsorption for each of the configurations of Figure 4.2 are reported in Table 3. On the reduced surface with the Ag octamer, two bent (BAVo1 and BAVo2) and one linear (LAVo1) CO_2 adsorption configurations were found, as shown in Figure 4.2a-c. In the presence of the Pt octamer, six bent (BPVo1-BPVo6) and one linear (LPVo1) CO_2 adsorption configurations were found, as shown in Figure 4.2d-j. As we did for the vacancy-free surface, we categorize the configurations into two categories: one where CO_2 binds directly to the TiO_2 surface (LAVo1, LPVo1, BAVo1, BPVo5), and another where there is direct interaction with the metal cluster (BAVo2, BPVo1, BPVo2, BPVo3, BPVo4, BPVo6).

For adsorption at TiO_2 sites (with octamer present), as we found for the perfect surface, the presence of the Ag or Pt octamer has an impact on TiO_2 sites, even those that are not directly associated with the octamer. However, unlike the perfect surface case, there does not appear to be a significant dependence on the specific orientation of the adsorbed CO_2 molecule.

Again, some insight can be gained by comparing adsorption configurations on the reduced surfaces with Ag/Pt to analogous configurations on the reduced surfaces without the octamer. The linear LAVo1 and LPVo1 configurations (Figure 4.2, c & j) are similar structurally, and are closest to LVo1 for the octamer-free surface (Fig. B6d in Appendix B); nevertheless, these two sites show longer bonding lengths between O of CO_2 and Ti atom by 0.38 Å and 0.29 Å, and less than half the adsorption energy magnitude of the octamer-free surface. For these linear geometries, the net effect of the octamers on CO_2 adsorption is therefore consistent between the reduced and perfect (vacancy-free) surfaces. The bent BAVo1 and BPVo5 (Figure 4.2, a & h) geometries, which are almost the same in terms of adsorption configuration, are also less stable compared to the analogous mode on the reduced surface (BVo2 in Fig. B6f in

Appendix B). In other words, the presence of Ag and Pt octamers weakens the CO_2 binding with the reduced surface in this configuration (in fact, BPVo5 becomes a metastable mode). Accordingly, the trend for the bent geometries matches that for the linear geometries, but is the opposite of the trend found in perfect surface-supported octamers. At first glance, this is curious given that the Bader charge analysis also shows negative charge localization at the binding O of the CO_2 molecule upon adsorption in the LAVo1 (0.019e) and LPVo1 (0.033e) configurations. However, this accumulation is much less than what we observed for LVo1 on the octamer-free surface (0.060e), which is consistent with the relative decrease in adsorption energy, and with the increase in the binding distance of the O atoms of CO_2 and the surface Ti atoms. We caution, however, that BAVo1 and BPVo5 show enhanced net charge transfer in the two binding O atoms compared to BVo2, but do not demonstrate a consistent trend in the adsorption energy; accordingly, significant charge transfer should be seen only as a rough guideline for predicting adsorption.

For adsorption at sites associated with octamers, like the perfect surface with Pt/Ag, we find that more additional CO_2 adsorption sites are introduced at the Pt octamer than at the Ag octamer (five for Pt vs. one for Ag); note that this difference between the two metals is even more pronounced than we saw with the perfect surface. We also find that although the reduced surface provides more binding sites at the octamer, the presence of the oxygen vacancy does not in general enhance the binding strength of CO_2 with respect the Ag/Pt-decorated perfect surface.

The lone Ag binding site, BAVo2 (Figure 4.2b), is a metastable adsorption site with the C atom of CO_2 binding with 3c-O, and with one O atom of CO_2 interacting with the Ag octamer at a distance of 2.36 Å while the other O atom fills the oxygen vacancy site. This configuration is similar to the corresponding mode on the reduced surface without Ag (BVo3 in Fig. B6g in

Appendix B), but it has a much smaller adsorption energy magnitude (by 0.65eV). This indicates that the Ag octamer's presence mitigates the CO_2 adsorption in this configuration. The net charge on the adsorbed CO_2 is also quite different when the Ag octamer is present: the charge transfer to the O atom of CO_2 in BAVo2 is almost double that in BVo3 (no octamer), while the charge transfer to the C atom is one fifth as large.

Five additional adsorption modes were observed on the reduced surface-supported Pt octamer, two more than were found for the perfect surface-supported case. Configuration BPVo1 (Figure 4.2d) can be compared to the perfect surface-supported BP1 (Figure 4.1d), since both sites involve CO_2 adsorption at the interface edge with comparable binding distances of CO_2 to the Pt octamer (albeit with a slight distance decrease by 0.11 Å of the O atom binding to the surface Ti and a smaller O-C-O angle by almost 2.8°). Configuration BPVo2 (Figure 4.2e) is similar to BP3 (Figure 4.1f), and mainly involves an interaction with one Pt atom in the top layer; again, both of these configurations possess comparable CO_2 binding parameters except for a 0.16 Å shorter distance between O of CO_2 and the Pt atom. BPVo3 (Figure 4.2f) is an analogous configuration to BP2 (Figure 4.1e), and both possess comparable CO_2 binding parameters except for a 1.7° smaller O-C-O angle for the former. However, BPVo4 (Figure 4.2g) and BPVo6 (Figure 4.2i) are unique configurations that have no analog in the perfect surface-supported Pt octamer case. BPVo4 (Figure 4.2g) shows CO_2 interacting at the interface edge, mainly with one Pt atom in the bottom layer of the octamer. This Pt atom binds the C and O of CO_2, while the other O atom of the adsorbate binds with a 5c-Ti atom, leading to an O-C-O angle of 140.6°. BPVo6 (Figure 4.2i) is also an interfacial CO_2 adsorption configuration, but a metastable one. In this case, the C atom is interacting with two Pt atoms, while one O atom is simultaneously interacting with one Pt and one surface 5c-Ti atom. Note that among all the CO_2 adsorption

configurations obtained in this research, the O-C-O angle in BPVo6 (121.1°) is the smallest, and the binding distance of C and O in CO_2 (1.39 Å) is the longest. Furthermore, this O-C-O angle is smaller than those of the CO_2 anion reported experimentally and computationally, and the C & O intra-bonding distance is larger by around 0.14 to 0.16 Å.[122, 141] This may account for the instability of this mode in terms of total energy, but it also reveals a strong tendency for CO_2 dissociation to occur on this model surface if binding can be achieved.

The adsorption energy for the Pt-derived configurations on the reduced TiO_2-supported Pt octamers is on average comparable to those on the perfect TiO_2-supported Pt octamers. This indicates that the presence of the oxygen vacancy does not contribute to the CO_2 adsorption energetically in the presence of the Pt octamer. However, because additional adsorption sites are introduced by the vacancy-induced modification of the local surface structure, it is likely that the net effect should be to enhance CO_2 photoreduction activity. This assumption is supported by the fact that all five Pt-derived binding configurations (BPVo1-BPVo4 and BPVo6) show a tendency for notable negative charge accumulation in the C atom of CO_2 molecule. Examination of the associated charge density difference plots provides additional confirmation of this effect (plots for BPVo1 and BPVo2 can be found in Fig. B7 in Appendix B). The magnitude of the charge accumulation is comparable to that seen in the modes on the perfect surface-supported Pt octamer, and as in the latter case, appears to correlate with the decreasing O-C-O angle of CO_2 (with one exception for BPVo6).

In summary, the reduced anatase TiO_2 (101)-supported Pt octamer surface shows the potential to activate CO_2 by generating the bent form of the molecule, while simultaneously increasing the number of available adsorption sites. This enhanced catalytic capability mirrors

our conclusions for clean reduced anatase TiO_2 (101) (BVo1-BVo4), and generally matches observations for Zn_2GeO_4 (010) & (001)[138], brookite (210)[139], and ceria (110)[140] surfaces.

4.3.2.2 Binding Mechanism

Additional insight into the influence of the octamer on CO_2 adsorption can be obtained by investigating the binding mechanism and electronic structure in more detail. We focus on two scenarios that are of particular interest: first, adsorption on perfect and reduced anatase sites for which there is no direct binding to the octamer; and second, adsorption on the Pt octamer, which introduces the most additional adsorption sties.

For adsorption on TiO_2 sites (with octamer present) and focusing first on sites where CO_2 is not directly bound to the octamer, we find that electrostatics seem to play the dominant role in the binding mechanism. More specifically, there is a competition between attraction and repulsion of CO_2 by surface Ti atoms: CO_2 adsorption on the TiO_2 (101) surfaces is affected by Ti atoms either attracting the O atom of CO_2 or else repelling the C atom.

The Ti-O attraction can be seen by observing the linear adsorption modes for all tested surfaces (refer to L1 & LVo1 in Fig. B6, LA1 & LP1 in Figure 4.1, and LAVo1 & LPVo1 in Figure 4.2), for which there is a general correlation between the binding strength and the net charge transfer to the binding O of the CO_2 molecule. For example, LVo1 has the highest adsorption energy as well as almost the highest net charge on the binding O atom of CO_2 (0.060e). The most notable exception to this trend is LP1, which has a net charge transfer to O that is comparable to LVo1 (0.061e), yet exhibits much weaker CO_2 binding. This is likely due to the different orientation of the adsorbed CO_2 molecule, as reflected in the variation in the electronic properties of linear modes obtained by Sorescu and coworkers.[128] By comparing LVo1 and LP1, both adsorb along [010] and are surrounded by three surface Ti atoms (more than those

of other linear modes), but CO_2 on LP1 lies flatter. This leads to a clear difference in the average distance between the C atom of CO_2 and the nearby surface Ti atoms, which is smaller for LP1 (3.89Å) than for LVo1 (4.01 Å). A likely consequence of this is increased electrostatic repulsion[122] between C and surface Ti atoms in the case of LP1, which results in a smaller adsorption energy.

Such repulsion role of C of CO_2 is also a factor in the binding strength of the bridge carbonate-like configurations (refer to B2 & BVo2 in Fig. B6, BA2 & BP4 in Figure 4.1, and BAVo1 & BPVo5 in Figure 4.2), where it competes with bonding between O atoms of CO_2 and surface Ti atoms. The Bader charge analysis of the pair of BP4 & BPVo5 suggests these two are dominated by the Ti-O bonding effect. Given that C of CO_2 in both modes exhibits the same electronic trend, the difference in the total negative charge accumulation at both O atoms of CO_2 uniquely explains the differences in their binding strength. On the other hand, the pair of B2 & BVo2 illustrates that the charge on the C atom of CO_2 is highly relevant to the binding strength. Whereas the total negative charge accumulations at O of CO_2 are comparable in the two cases (0.067 & 0.064e), the C of CO_2 in BVo2 gains a charge of 0.024e while that in B2 shows an opposite loss of 0.005e. As a result, BVo2 experiences less electrostatic repulsion than B2, which may explain why BVo2 is stable and B2 is metastable. Note that the least favored bridged-carbonate configuration identified in this study is B2, which has both weak binding via O of CO_2 (0.044e less charge accumulation compared to the barely favored BPVo5), as well as electrostatic repulsion between C of CO_2 and surface Ti atoms.

For adsorption at sites associated with Pt octamer, BP1-BP3 (Figure 4.1d-f) and BPVo1-BPVo6 (Figure 4.2d-i) reveal the Pt octamer's ability to provide additional adsorption sites for bent-form CO_2 species on anatase TiO_2 (101). This can be explained in terms of the electronic

structure of the Pt surface with respect to the adsorbate states, which facilitates the formation of bonding states. Figure 4.3 shows p-DOS plots for BP1 and BP2, superimposed with select charge density plots corresponding to specific states. The peaks corresponding to Pt and O of CO_2 show strong resonance at lower energy levels, as well as weaker resonances near the top of the valance band and in the bandgap. For Pt and C of CO_2 atoms, the resonant peaks lie mainly in the lower energy levels, with minor resonances elsewhere, especially in the range of -2eV to Fermi level. This suggests the adsorbed CO_2 has a strong tendency to hybridize with the Pt octamer at lower energy levels (around -10 eV ~ -6eV with respect to the Fermi level). Further examination of the charge density associated with DP1-DP4 (Figure 4.3a) and DP1&DP2 (Figure 4.3b) shows that CO_2 is using its bonding molecular orbitals (e.g. $2\sigma_g$ for DP1 in Figure 4.3a and $1\pi_u$ for DP2 in Figure 4.3b) to form additional bonding orbitals with d-like orbitals of the Pt octamer. At higher energies, additional orbital hybridization between C and the Pt octamer is observed, as can be seen in the charge densities associated with the DP3&DP4 states in Figure 4.3b. The ability of CO_2 to form a bonding orbital with the Pt octamer is attributable to the matching shapes, orientations, and comparable energy levels of the two sets of orbitals.[119] It can be concluded that the additional CO_2 adsorption sites provided by Pt octamer are made possible by the ability of Pt to form bonding orbitals with CO_2 molecule. In other words, the dominant binding mechanism for CO_2 on the Pt sites involves orbital hybridization, whereas electrostatic interactions dominate at sites associated with the TiO_2 surface.

4.3.2.3 Vibrational Frequencies

Analyzing the CO_2 vibrational frequencies on the surfaces with Ag/Pt octamers offers insight into key bond characteristics of the adsorbed molecule, and can provide a useful roadmap for interpreting experimental vibrational spectra. Table 2 & 3 shows the calculated vibrational

frequencies for CO_2 adsorbed on surfaces of anatase (101)-supported Ag and Pt octamers. Significantly, we find that specific vibrational modes can be used as indicators for key geometric and electronic quantities that are directly relevant for CO_2 activation. In particular, among the Pt octamer-associated bent-form CO_2 molecules, there is a correlation between the bending frequency (ν2) and negative charge accumulation at C, and between the asymmetric stretching frequency (ν3) and the O-C-O angle of the adsorbed CO_2 molecule. Moreover, characteristics of the ν2 and ν3 modes may reveal different CO_2 adsorption sites.

The experimental vibrational frequencies of symmetric (ν1) and asymmetric (ν3) stretching for linear adsorbed CO_2 on P25 and several metal oxide surface were reported to be around 1259 and 2373 cm^{-1},[142, 143] while frequencies for adsorbed bent-form CO_2 were reported to be 1315 and 1589 cm^{-1} on anatase TiO_2.[144] For the CO_2^- anion, the reported values are 1219 and 1640 cm^{-1} on P25,[143] 1245 and 1670 cm^{-1} on anatase TiO_2,[144] and 1247 and 1670 cm^{-1} on anatase TiO_2 in the presence of H_2O.[145] Previous calculation results[122, 128, 139] revealed that on neutral perfect anatase TiO_2 (101) and brookite TiO_2 (210) surfaces, the calculated vibrational frequencies of the bent CO_2 modes were close to the experimental results, although the electronic analysis prevented the actual formation of CO_2^- anion. For the reduced surfaces, the formation of CO_2^- anion was found, with the calculated vibrational frequencies showing a comparable or slightly larger shift with respect to the experimental values. The relatively good agreement between theory and experiment justifies comparison of our results to published data.

As described above, significant electron transfer to the CO_2 adsorbate was mainly found on the perfect and reduced TiO_2 surfaces in the presence of the Pt octamer. The most promising configurations for CO_2 activation are BP1 - BP3 in Figure 4.1d-f and BPVo1 - BPVo4 in Figure 4.2d-g, since these exhibit sufficient electron transfer so as to be close to an adsorbed CO_2^- anion.

Calculated vibrational frequencies indicate that the corresponding IR bands for the adsorbed CO_2 are obtained in the range of 602-1934 cm^{-1}. Compared to the reported experimental values for CO_2 on anatase TiO_2, ν1 modes show redshifts up to 131 cm^{-1}, while for ν3 the largest redshift is around 159 cm^{-1} and the largest blueshift around 264 cm^{-1}. The ν2 (bending) mode varies from 602 to 805 cm^{-1}. Note that ν1 and ν3 (1130 and 1690 cm^{-1}) of BP2 are the closest to the experimentally reported values for anatase.

Among the Pt octamer-associated CO_2 adsorption modes (BP1 - BP3 in Figure 4.1d-f and BPVo1 - BPVo4 in Figure 4.2d-g) in which the C atom gains appreciable negative charge, a clear trend between the ν2 mode and the charge accumulation at C was found, as shown in Figure 4.4a. Higher electron accumulation at C is correlated with a higher ν2 mode. This may be related to increased stiffness of the intra C-O bond of CO_2 due to the dipole moment enhancement from the charge transfer to C. Notably, the ν2 mode was also used by He et al.[122] to characterize the net charge transfer to C associated with CO_2 adsorption on the clean anatase TiO_2 (101) surface. Also, Figure 4.4a shows that in general, interface edge adsorption sites (in red circle, excepting BPVo4) tend to possess higher ν2 modes compared to adsorption sites directly on the Pt octamer (in green dotted circle). Furthermore, if we compare the Pt octamer-associated CO_2 adsorption modes in Figure 4.4a with modes not directly associated with the Pt octamer (BP4 in Figure 4.1g and BPVo5 in Figure 4.2h), the former tend to have ν2 modes below ~800 cm^{-1} while the latter tend to have ν2 modes above that value. This is likely because C interacts with different atoms in these two cases. In the direct interaction of C with Pt atoms, there is noticeable net charge transfer to C and hybridization with the Pt states, which induces a stronger interaction and an associated reduction in the frequency of the bending mode. In contrast, TiO_2 surface sites exhibit a much weaker interaction between C and surface O atoms,

involving comparatively minor charge transfer; this accounts for the higher frequency of the CO_2 bending.

The ν3 asymmetric stretching mode for the surfaces with Pt octamers correlates well with the O-C-O angle of the adsorbed CO_2 molecule. As shown in Figure 4.4b, the smaller the angle, the smaller the value of ν3 (note that this trend holds true even for configurations where charge transfer to C is minimal, i.e., BP4 and BPVo5). For the bent forms on the perfect surface in the presence of the Pt octamer (BP1-BP4 in Figure 4.1d-g), ν3 decreases as 1918, 1690, 1615, and 1511 cm^{-1}, and the O-C-O angle as 148.4, 135.9, 132.2, and 127.7°. Similarly, on the supported reduced surface (BPVo1 - BPVo5 in Figure 4.2d-h), ν3 decreases as 1934, 1791, 1715, 1647, and 1529 cm^{-1}, and the O-C-O angle decreases as 147.6, 140.6, 134.2, 132.5, and 124.9°. Apparently, the smaller O-C-O angle mitigates the antisymmetric stretching of the CO_2 molecule. Moreover, comparing the adsorption modes on the Pt octamer with those at the interface edge, the latter tend to possess a smaller O-C-O angle, and a correspondingly lower ν3 frequency. This is due to the cliff-like geometry created at the interface between the Pt octamer and the anatase (101) surface, which allows CO_2 to adsorb with an O-C-O angle that approaches 90°. Excepting BPVo4, we suggest that a smaller value of ν3 (~1500-1540 cm^{-1}, red circle in Figure 4.4b) could be used as a signal that CO_2 is adsorbed at the cluster/support interface edge.

In summary, for bent-form CO_2 species associated with the Pt octamer, a higher ν2 mode seems to be an indicator of adsorbed CO_2 with more negative charge accumulation. On the other hand, a higher ν3 mode seems to reveal a larger O-C-O angle of CO_2. Moreover, a ν2 mode below ~800 cm^{-1} tends to indicate CO_2 adsorption sites for which there is direct interaction between the adsorbate at the Pt octamer, whereas direct TiO_2 surface sites show higher ν2 values. Values of ν2 in the range ~750-800 cm^{-1} are primarily associated with interface edge adsorption,

whereas values below that range indicate adsorption mainly on the Pt octamer itself. Interface edge adsorption sites may also be revealed by smaller ν3 values (~1500-1540 cm^{-1}).

Note that according to Tables 2 & 3, the calculated frequencies of pairs with similar adsorption configurations (e.g., BP1 & BPVo1, BP2 & BPVo3, and BP3 & BPVo2) are similar to each other. This gives confidence in uniquely assigning frequencies to observed adsorption sites. For instance, on the surfaces with a Pt octamer deposited on anatase TiO_2 (101), we can assign ν1 and ν3 in the ranges of 1174-1203 cm^{-1} and 1511-1529 cm^{-1}, respectively, to an adsorbed CO_2^- anion at the interface edge. The ν1 and ν3 ranges of 1114-1130 cm^{-1} and 1690-1715 cm^{-1} can be assigned to a CO_2^- anion on a Pt octamer involving simultaneous interaction with two Pt atoms. The ν1 and ν3 ranges of 1142-1167 cm^{-1} and 1918-1934 cm^{-1} can be ascribed to a CO_2^- anion on a Pt octamer involving interaction with only one Pt atom.

4.3.3 Pt Octamer Induced CO_2 Dissociation to CO

So far, we have considered the formation of surface-adsorbed complexes that resemble the CO_2^- anion, which is a key precursor for the formation of CO. In this section, we explore a possible pathway for the subsequent reduction step, namely, cleavage of CO_2^- to form surface-adsorbed CO on a neutral surface of a reduced anatase TiO_2 (101)-supported Pt octamer.

The dissociation of CO_2 to CO has been investigated by a number of investigators.[145-148] While such dissociation was observed on the surfaces of reduced TiO_2-supported Pt, Rh, and Ir upon illumination at 190K, supported Pd and Ru surfaces exhibited no CO formation.[146] An investigation using an electron-induced route (i.e., electrocatalysis) was also reported on reduced TiO_2 (110) with a threshold of 1.4 eV.[148] Based on DFT calculations, promising photocatalysts such as Zn_2GeO_4 (010)[138] and ceria (110)[140] also suggest the possibility of forming CO from CO_2 dissociation on surfaces with oxygen vacancies. One common feature of the proposed

dissociation mechanisms is that one O atom of the CO_2 molecule is linked to the oxygen vacancy, resulting in the weakening of the C-O bond.

Figure 4.5 shows a possible dissociation pathway (CF1-CF7) for adsorbed CO_2 to adsorbed CO. In the final configuration (CF7), CO is found at the interface edge with C interacting with two Pt atoms at an average distance of 1.94 Å and O with 5c-Ti in a distance of 2.28 Å. The dissociated O bridges a 5c-Ti and a Pt atom at distances of 1.78 Å and 2.01 Å, respectively. To understand the energy needed to activate the CO_2 dissociation, a scenario is investigated starting with CO_2 adsorbed on the TiO_2 surface, shown in CF1 (resembling the BPVo5 CO_2 adsorption configuration in Figure 4.2h). The CI-NEB calculation shows that a disturbance of 0.15eV is initially needed to destabilize the adsorbed CO_2 (CF2), following which the system follows a downhill path to a configuration where C of the CO_2 is interacting with one Pt atom of the Pt octamer (CF3). The major energy barrier (CF4) is then reflected in the extraction of one O from CO_2 to a bond distance of 1.83 Å (for reference, the calculated bond distance of C-O is 1.18 Å for free CO_2), followed by a downhill path to continue the C-O separation and transition to a configuration in which the C atom interacts with two Pt atoms instead of one (CF5-CF7). The energy barrier of CO_2 dissociation to CO is estimated to be 1.01eV.

This mechanism is different from what has been reported for larger nanoparticles, where one O of CO_2 fills the oxygen vacancy as C bonds to the nanoparticle, then upon irradiation transfers the photo-induced charge to the CO_2 molecule to activate C-O bond breaking.[146] In the case of the Pt octamer on reduced anatase (101), our proposed dissociation mechanism is not directly related to filling of the oxygen vacancy. Rather, the key role of the vacancy here is to enable the cluster to more easily modify its geometry to facilitate the dissociation process. This is

a direct consequence of the fluxionality of the subnanometer metal cluster, which is not possible for larger particles. This geometric reorganization is best seen in the early steps in the proposed mechanism (CF2-CF4), in which one Pt atom stretches out of the Pt octamer to interact with the CO_2 molecule.

The weakening of the C-O bond is attributed to the filling of antibonding orbitals of the CO_2 molecule.[110] Based on the configurations in Figure 4.3, it is difficult to uniquely identify the antibonding orbitals, but the highest bonding orbital of CO_2 can be seen in DP4 of Figure 4.3a and DP2 of Figure 4.3b, which lie deep below the Fermi level. This suggests that the hybridization of antibonding orbitals of CO_2 could also occur below the Fermi level. For instance, in Figure 4.3b, states DP3 & DP4 clearly have antibonding character, and could lead to the cleavage of the C-O bond of the CO_2 molecule. This result suggests another possible advantage that Pt octamers or other subnanometer metal clusters may bring to CO_2 photoreduction.

4.4 Conclusions

The presence of Ag or Pt octamers can substantially modify CO_2 adsorption on perfect & reduced anatase TiO_2 (101) based on DFT calculations. In fact, the presence of the Ag & Pt octamers affects CO_2 adsorption even at TiO_2 surface sites where there is no direct binding between CO_2 and the octamer, suggesting the octamer modifies the properties of the TiO_2 itself as it donates electron density to the surface. For adsorption on the TiO_2 sites not directly abutting the octamers, the nature of the Ag/Pt-induced effect depends on the orientation of the adsorbed CO_2 molecule. It also differs for the perfect (vacancy-free) and reduced (oxygen vacancy) surfaces. We attribute this behavior to a binding mechanism that involves electrostatic competition between two factors: (1) attraction between Ti and the O atom of CO_2 as the latter accepts negative charge from the surface; and (2) repulsion between Ti and the C atom of CO_2.

Deposition of subnanometer Pt clusters appears to provide certain important advantages for CO_2 activation on anatase TiO_2 (101) surfaces. First, the Pt atoms provide extra adsorption sites for bent-form CO_2—a key dissociation precursor state leading to the products of CO_2 photoreduction—as compared to the Ag-octamer-decorated or pure anatase TiO_2 (101) surfaces. The available sites were found at the interface edge of the Pt octamer and the anatase surface, and also directly on the Pt octamer. In most cases, the adsorption strength at these sites is also enhanced, which is generally beneficial for bond activation. In addition, Bader charge analysis suggests that at these Pt surface or Pt-TiO_2 interface sites, the adsorbed CO_2 can be spontaneously converted to a CO_2^- anion-type complex as negative charge accumulates at the C atom of the CO_2 molecule. A detailed examination of the associated electronic structure suggests that unlike binding to TiO_2 sites, where electrostatics play a key role, the interaction between CO_2 and Pt is instead facilitated by the molecular orbitals of CO_2 forming bonding orbitals with d states of Pt in the octamer. This explains the significant charge transfer to the adsorbed CO_2, as well as the Pt octamer's ability to provide additional adsorption sites. This same advantage is lacking for the Ag octamer, likely a consequence of insufficient orbital overlap due to the shape and orientation of the outer s orbitals of Ag.

Calculated vibrational frequencies suggest that the ν2 vibrational mode of bent CO_2 molecules adsorbed on Pt octamers can be used as an indicator of negative charge accumulation on C, and hence the formation of the CO_2^- anion precursor. In addition, a direct relation between the ν3 mode and the O-C-O angle of the CO_2 molecule was found, providing a possible indicator for identifying bent CO_2 geometries. Information from the vibrational frequencies can also be used for identification of CO_2 adsorption sites. For instance, a ν2 mode > ~800 cm^{-1} seems to indicate CO_2 adsorption on sites that are not directly associated with the Pt octamer, while lower

frequencies correspond to sites that are related to the Pt octamer. Also, ν2 in the ~750-800 cm^{-1} range, combined with a small ν3 (~1500-1540 cm^{-1}), tends to indicate interface edge adsorption.

Finally, we show one possible mechanism by which a Pt octamer on reduced anatase TiO_2 (101) could further dissociate adsorbed CO_2 to CO, aided by the enhanced fluxionality of the Pt octamer due to the oxygen vacancy, and by the filling of antibonding orbitals of CO_2 to weaken the intramolecular C-O bond. The calculated energy barrier for this surface dissociation process is 1.01eV. In summary, our results suggest that subnanometer metal clusters such as Pt could be used to enhance the photocatalytic activity of TiO_2 and other semiconductors.

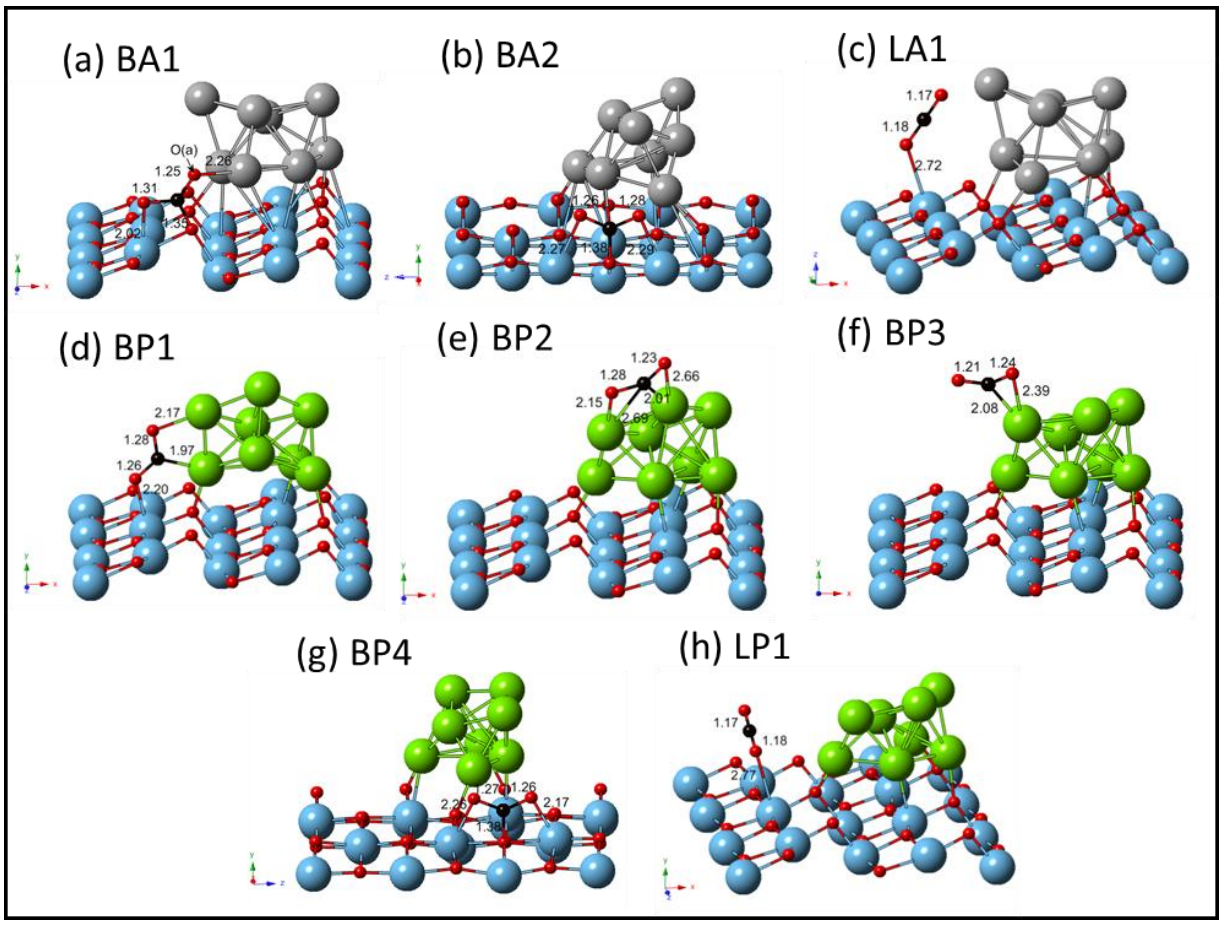

Figure 4.1 Stable CO_2 adsorption configurations on the perfect anatase TiO_2(101) surface in the presence of Ag and Pt octamers (O in red, C in black, Ti in blue, Ag in silver, Pt in green. The numbers indicate the bond lengths in Å).

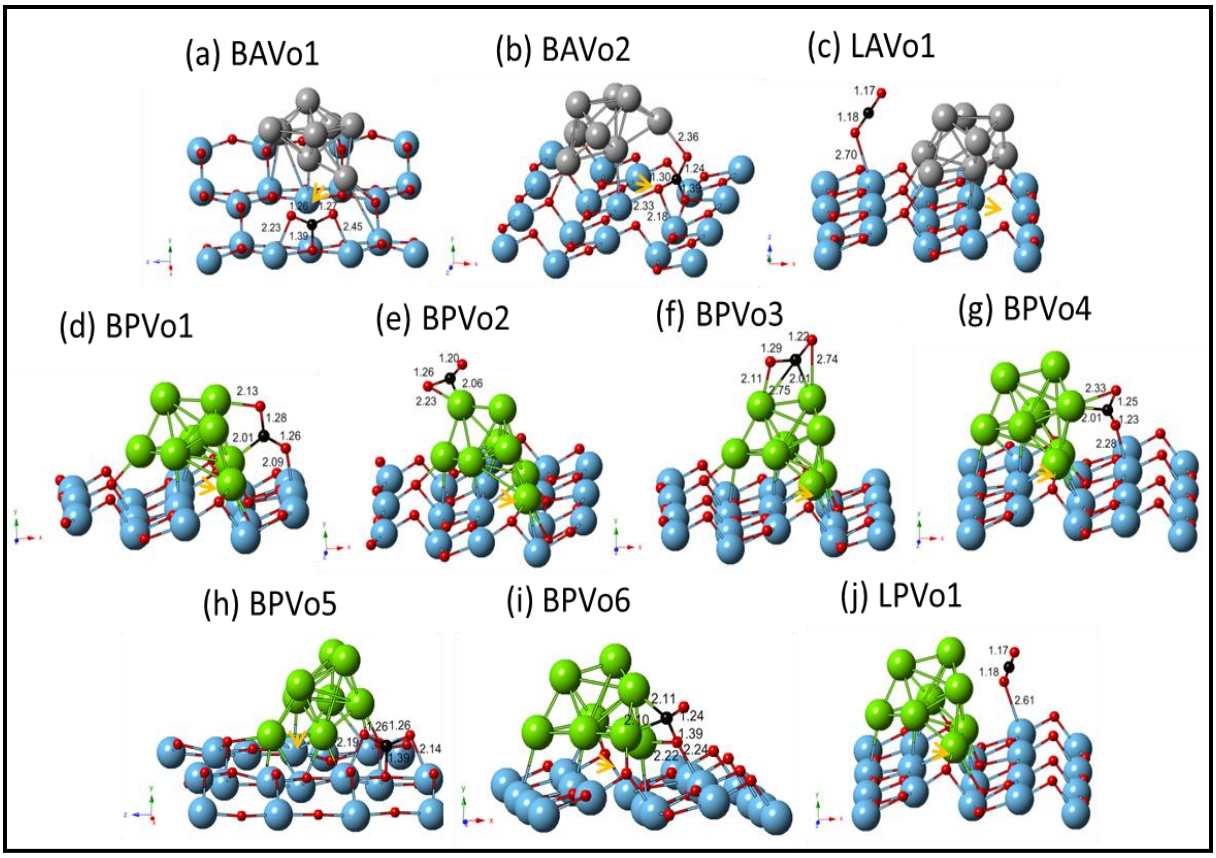

Figure 4.2 Stable CO_2 adsorption configurations on the reduced anatase TiO_2(101) surface in the presence of Ag and Pt octamers (O in red, C in black, Ti in blue, Ag in silver, Pt in green. Yellow arrow indicates the oxygen vacancy. The numbers indicate the bond lengths in Å).

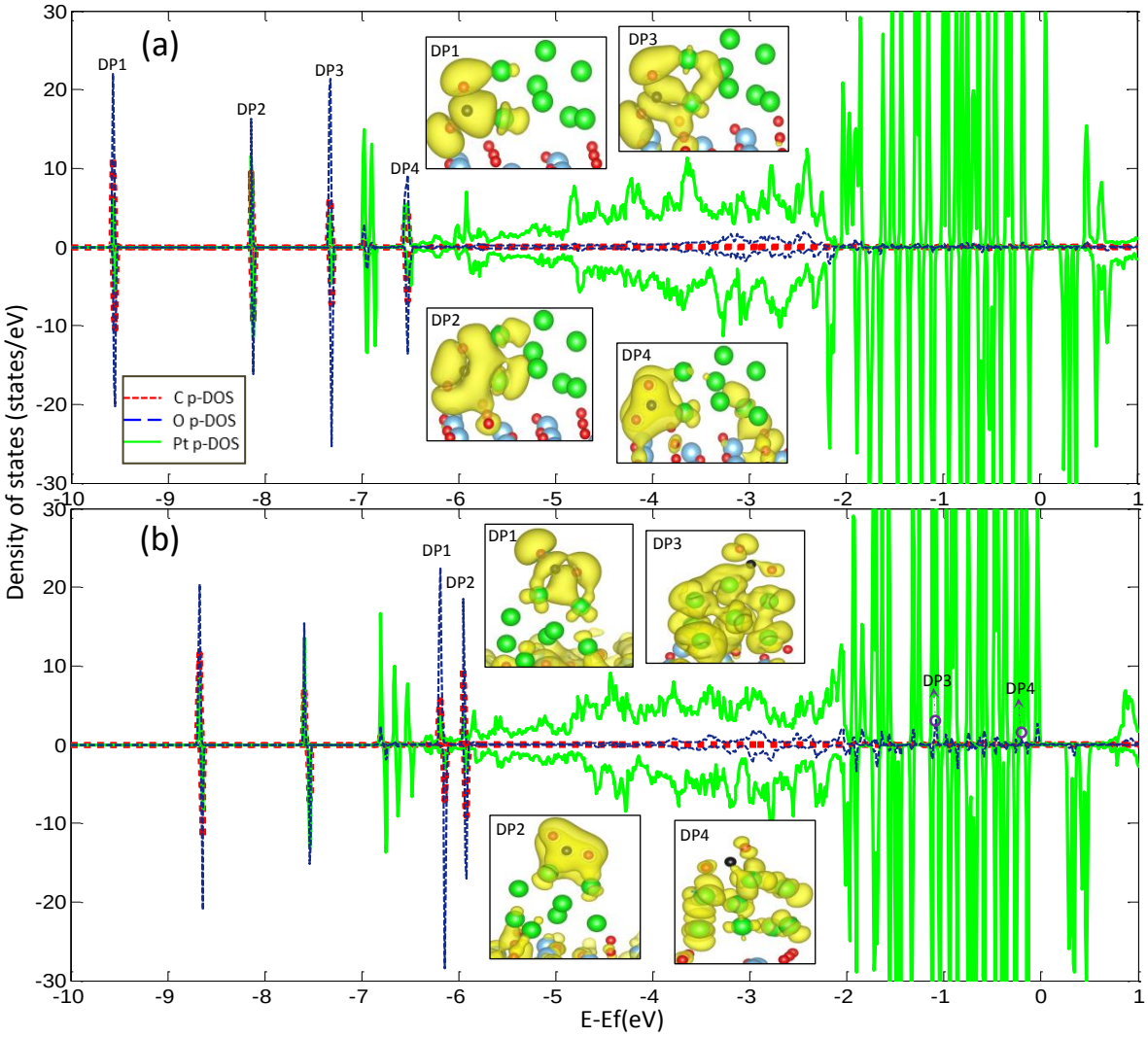

Figure 4.3 p-DOSs (C & O of CO_2 and Pt) and associated density plots of specific states formed upon CO_2 adsorption at the interface edge (BP1) and directly on the Pt octamer (BP2): (a) configuration BP1 with states DP1-DP4 at -9.57, -8.13, -7.32, and -6.53 eV; (b) configuration BP2 with states DP1-DP4 at -6.17, -5.93, -1.10, and -0.13 eV (Above and below the axis correspond to spin up and spin down, respectively).

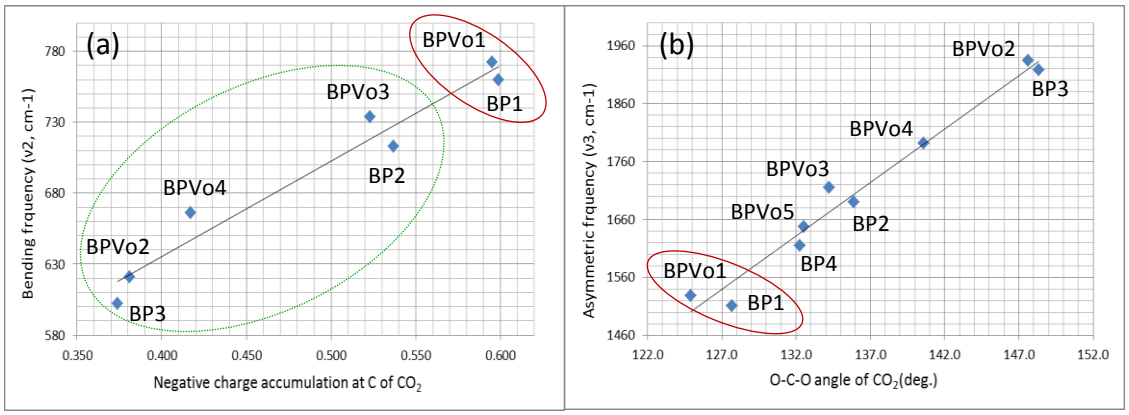

Figure 4.4 Correlations between (a) the bending frequency (ν2) and the negative charge accumulation at C of CO_2, and of (b) the asymmetric stretching frequency (ν3) and the O-C-O angle of CO_2. (Red circle: CO_2 adsorption sites at the interface edge; Green dotted circle: CO_2 adsorption sites directly on the Pt octamer.)

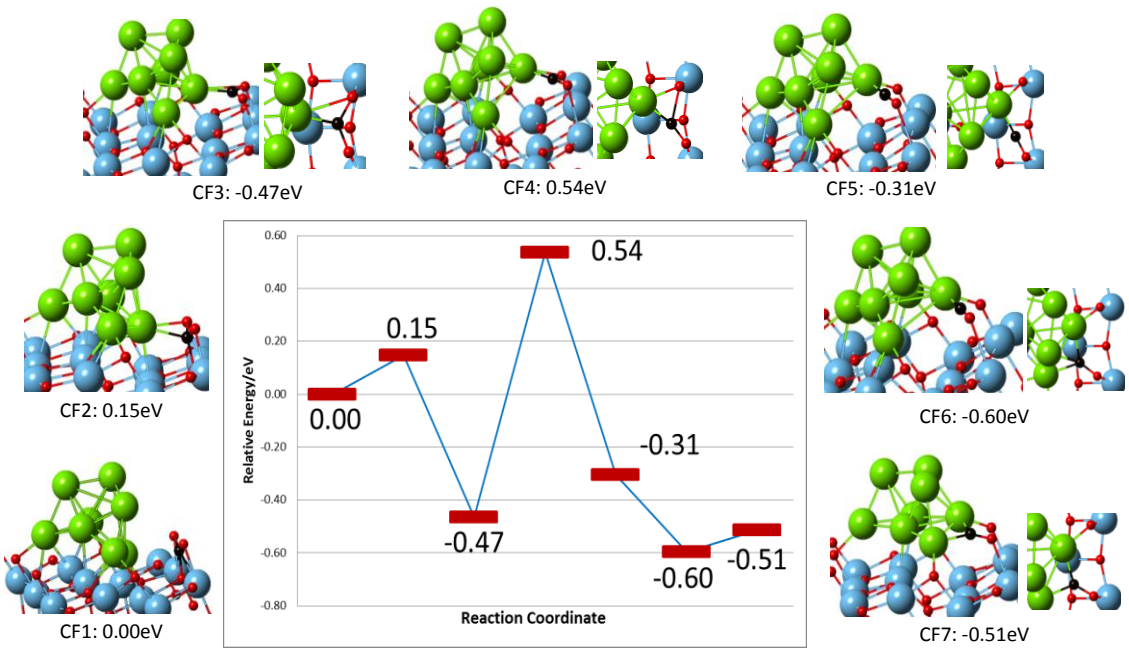

Figure 4.5 A proposed pathway, CF1-CF7, for CO_2 dissociation to CO on the surface of a reduced anatase TiO_2(101)-supported Pt octamer.

Table 4.1 Calculated properties[a] based on CO_2 adsorption configurations on perfect/reduced anatase TiO_2(101).

Ads. config.	$-E_{ads}$(eV)	∠OCO(deg.)	Δe of CO_2	Δe of C in CO_2
B1	-0.02	130.1	-0.011	0.017
B2	-0.09	134.1	0.062	-0.005
L1	0.14	178.7	-0.013	-0.025
BVo1	0.76	135.2	0.799	0.827
BVo2	0.51	132.4	0.088	0.024
BVo3	0.37	127.6	0.150	0.064
BVo4	0.13	150.1	0.393	0.421
BVo5	-0.03	129.9	0.001	-0.005
LVo1	0.36	177.8	-0.036	-0.048

[a] Values represent the adsorption energy, O-C-O angle of CO_2, and the difference of the Bader charge of the CO_2 molecule upon adsorption (Δe >0 means negative charge accumulation; L and B represent linear and bent adsorption forms, respectively; Vo represents an oxygen vacancy).

Table 4.2 Calculated properties[a] based on CO_2 adsorption configurations on perfect anatase TiO_2(101) in the presence of Ag and Pt octamers.

Ads. config.	$-E_{ads}$(eV)	∠OCO(deg.)	Δe of CO_2			ν(CO_2)(cm^{-1})		
			C	O	O	ν1	ν2	ν3
BA1*	0.31	126.1	-0.012	-0.018	0.072	1213	827	1606
BA2	0.20	132.7	0.001	0.077	0.102	1247	801	1629
LA1	0.11	178.6	-0.014	0.000	0.026	1317	624	2359
BP1*	0.72	127.7	0.599	0.044	-0.051	1174	760	1511
BP2*	0.69	135.9	0.537	-0.041	-0.053	1130	713	1690
BP3*	0.16	148.4	0.374	-0.058	0.000	1167	602	1918
BP4	0.09	132.2	-0.006	0.054	0.072	1260	806	1615
LP1	0.10	179.0	-0.029	-0.003	0.061	1307	608	2345

[a]Values represent the adsorption energy, O-C-O angle of CO_2, difference of the Bader charge of the CO_2 molecule upon adsorption, and vibrational frequencies of symmetric (ν1), bending (ν2), and asymmetric (ν3) stretching modes (Δe >0 means negative charge accumulation; L and B represent linear and bent adsorption forms, respectively; A and P represent Ag and Pt; asterisks indicate direct interaction with Ag/Pt octamers).

Table 4.3 Calculated properties[a] based on CO_2 adsorption configurations on reduced anatase TiO_2(101) in the presence of Ag and Pt octamers.

Ads. Config.	$-E_{ads}$(eV)	∠OCO(deg.)	Δe of CO_2			ν(CO_2)(cm^{-1})		
			C	O	O	ν1	ν2	ν3
BAVo1	0.12	132.9	0.009	0.068	0.092	1251	798	1640
BAVo2*	-0.28	128.0	0.012	0.100	0.084	1185	806	1626
LAVo1	0.14	178.8	-0.014	0.002	0.019	1315	626	2359
BPVo1*	0.71	124.9	0.595	-0.058	0.039	1203	772	1529
BPVo2*	0.68	147.6	0.381	-0.086	-0.003	1142	621	1934
BPVo3*	0.66	134.2	0.523	-0.023	-0.065	1114	734	1715
BPVo4*	0.32	140.6	0.417	0.075	-0.077	1180	666	1791
BPVo5	0.00	132.5	-0.007	0.042	0.069	1265	805	1647
BPVo6*	-0.19	121.1	0.566	-0.020	0.009	1145	728	1670
LPVo1	0.15	179.3	-0.020	0.033	-0.009	1318	626	2361

[a]Values represent the adsorption energy, O-C-O angle of CO_2, difference of Bader charge of CO_2 molecule upon adsorption, and vibrational frequencies of symmetric (ν1), bending (ν2), and asymmetric (ν3) stretching modes (Δe >0 means electron accumulation; L and B represent linear and bent adsorption forms, respectively; Vo represents an oxygen vacancy; A and P represent Ag and Pt; asterisks indicate direct interaction with Ag/Pt octamers).

CHAPTER 5: MORPHOLOGY EFFECT OF SUPPORTED SUBNANOMETER PT CLUSTERS ON FIRST AND KEY STEP OF CO_2 PHOTOREDUCTION

This chapter summarizes the investigations of the geometry effect (2D-3D) of the supported Pt cluster on the key precursor for CO_2 photoreduction using Density Functional Theory calculations. Initially, from our previous study[113] it is anticipated that as long as it is Pt clusters the availability of the bent form CO_2 adsorption sites is expected. Interestingly, we find supported 3D rather than 2D Pt clusters benefit CO_2^- anion formation by providing more binding sites for bent CO_2 species and facilitating charge transfer. In addition, particularly for CO_2 adsorbed at interface edge site, 3D clusters tend to possess higher structural fluxionality than pro-2D clusters, and the structural fluxionality correlates positively with CO_2 binding strength. The binding competition among Pt - CO_2 interactions is found to affect the CO_2 adsorption. A model based on these two factors is proposed to explain why CO_2 does not adsorb on the surface of the pro-2D Pt cluster. Electronic structure analysis suggests for CO_2-TiO_2 supported Pt subnanometer clusters, CO_2 s&p - metal d are the dominating bonding states. Also, we find that the strong binding tendency of Pt clusters with surface Ti atoms determines the geometry of the deposited Pt clusters, which explains why on the reduced TiO_2 surface Pt tetramer and hexamer tend to be 2D geometries. The charge accumulation at C and the O-C-O angle of adsorbed CO_2 are found to correlate with the C-O bond breaking tendency. The C-O symmetric(v1), O-C-O bending (v2), and asymmetric (v3) stretching frequencies can be used as reliable indicators to

reveal unique electronic/geometric properties and C-O bond breaking tendency of adsorbed CO_2 as well as to distinguish specific adsorption sites.

5.1 Introduction

Ever since Fujishima and Honda first demonstrated photocatalytic water splitting with TiO_2 electrodes in 1972,[114] numerous researchers have extended the idea to environmental[115] and solar energy[116, 149] related applications. CO_2 photoreduction is of important application since it has dual effects of reducing the CO_2 levels in the atmosphere and generating renewable energy (light hydrocarbon). However, the efficiency of the photo-conversion remains a weakness.[7] Techniques to improve the efficiency include cocatalyst,[70] plasmonic active particles,[71, 72] doping,[5] and surface defects.[150] Understanding the mechanism of CO_2 photoreduction has been a focus of a number of theoretical studies.[7, 113, 122, 127, 151] Among CO_2 photoreduction steps, the highest reduction potential resides in the first step, CO_2 to CO_2^- anion, which makes itself a key step.[1] One vital factor for the success of this step is the geometry of the adsorbed CO_2 species,[7] bent form CO_2. Due to the decrease of the CO_2 LUMO energy as the O-C-O bond angle decreases, bent form CO_2 makes it easier to obtain photoexcited electrons to form CO_2^- anion.[7, 122] Prior ab initio studies have investigated CO_2 adsorption on different neutral surfaces of TiO_2 clusters.[124, 126, 127, 152] More thorough studies have considered periodic TiO_2 models with/without oxygen vacancies[122, 153] and interstitial Ti atoms at (sub)surfaces[128]. Other oxide surfaces such as Zn_2GeO_4[138] and ceria(110)[140, 154] have also been studied.

Oxide supported subnanometer metal clusters have drawn considerable interest due to their enhanced catalytic activity[21, 25, 118, 155-157] which are attributed to the unique properties of such tiny clusters: dynamic structural fluxionality,[118] larger fraction of under-coordinated surface atoms,[25, 156] and the interactions between deposited cluster and the support.[28] The fundamental

understandings of subnanometer metal cluster related studies have become crucial in advancing the development of promising subnanometer cluster based catalysts and photocatalysts.[29] We studied interplays between Ag&Pt clusters (dimer, tetramer, and octamer) and anatase TiO_2 (101) surface,[58] and developed a binding mechanism of cluster on support to assist subnanometer cluster characterization. Also, we proposed an explanation for decoration, and suggested indicators for sintering and clusters induced sub-bandgaps. Interestingly, we found the reconstruction of clusters, Pt tetramers exhibiting two dimensions (2D) and three dimension (3D) geometries.

Recently, we have studied the favored CO_2 adsorbates for the first and key step on subnanometer Ag&Pt clusters/anatase TiO_2 (101) surfaces, wanting to know what effect these tiny clusters can bring.[113] We found the presence of Ag and Pt octamers can enhance CO_2 adsorption through direct or indirect channels. Supported octamers can indirectly donate negative charge through the anatase TiO_2 (101) surface to enhance CO_2 binding. Interestingly, TiO_2-supported Pt octamers rather than supported Ag octamers can directly interact with CO_2 species, providing stable adsorption sites for bent-form CO_2 species as well as facilitating CO_2^- anion formation.

However, the effect of the cluster geometry (ex: structural fluxionality) on the key precursor adsorption is not well investigated. The cluster size is an important factor for catalytic behaviors of metal/oxide catalysts.[158, 159] Studies[38, 69, 160-162] have shown the catalytic activity is related to the cluster size and geometry. Watanabe et al.[160] showed that as the size of Pt_n(n=4, 7-10 and 15) on the rutile TiO_2 varied, there was a geometrical transition of planar and 3D dimensional structures at n=8, at which a significant decrease in activation energy occurred for CO oxidation reaction. Kaden et al.[69] reported that for Pd_n/rutile TiO_2 (n=1, 2, 4, 7, 10, 16, 20,

and 25) the size variation positively correlated with CO oxidation activity, and that the increase of the cluster size also correlated with the growth of cluster layer from one to two.

In this article, using density functional theory (DFT) we examine the effect of the cluster geometry (2D to 3D) on the preferred CO_2 adsorbates for the first and key step of CO_2 photoreduction, which we study on Pt tetramer, hexamer, and octamer[113] supported on perfect/reduced anatase TiO_2 (101) surfaces. We focus on the effect of geometries on the four basic ingredients leading to the formation of the precursor for CO_2 photoreduction:[113] (i) availability of binding sites, (ii) intermediate adsorption energy at those sites (too strong = traps; too weak = inactive), (iii) geometry of the bent CO_2, and (iv) charge transfer to C of CO_2. The displacement per Pt atom is found to represent cluster's structural fluxionality, and is used to investigate the relationship with these four basic ingredients. The properties of 2D and 3D geometries of the deposited clusters are explored in detail. The C-O bond breaking tendency is also evaluated. Finally, an attempt is made to connect with experimental studies by analyzing the variations in calculated vibrational frequencies for adsorbed CO_2 as a function of adsorption sites, geometry, and electronic information. Such understanding is intended to help the development of promising subnanometer metal cluster/semiconductor catalyst for CO_2 photoreduction.

5.2 Computational Methods

The choice of the surface was inspired by the fact that TiO_2 continues to be the standard material for the fundamental study of photocatalysis;[121] also, anatase TiO_2 (101) is the most stable surface and is the main constituent in commercial Degussa P25 photocatalyst.[82] Anatase TiO_2 (101) surface is characterized by 2-fold(2c)/3-fold(3c) coordinated O atoms, and 5-fold(5c-)/6-fold(6c-) coordinated Ti atoms. The 3c-O atoms consist of 3c-O between 5-c Ti and between 6-c Ti atoms.[58] Pristine anatase surface (i.e., perfect surface) is considered as well as the surface

with an oxygen vacancy (i.e., reduced surface) due to interesting catalytic effect from point defects such as oxygen vacancies, hydroxyl groups, and interstitial atoms.[79] Oxygen vacancy (reduced surface) is modeled by removing an oxygen atom from a bridge site (2c-O) to compare with previous work[113] and others.[122, 128] The stable geometries of the supported Pt tetramer and hexamer on perfect and reduced were obtained using the method described in our previous work.[58]

The DFT calculations were performed using the VASP (Vienna Ab Initio Simulation package) code.[87-89] Exchange-correlation was represented by the Perdew–Burke–Ernzerhof (PBE) functional of the generalized gradient approximation (GGA),[90] and the electron-ion interactions were modeled by the projector-augmented wave (PAW)[91] method. A kinetic energy cutoff of 500 eV was used for the wavefunctions, and energies were converged to 10^{-5} eV. Spin polarized calculations were incorporated in all calculations with the force convergence criteria on each atom set to < 0.01 eV/ Å. One limitation of the standard DFT is to underestimate the bandgap of transition metal oxides due to the improperly description of the strongly correlated d- and f-states. Thus, in our model the strong electron localization at surface Ti atoms surface may affect the charge transfer among the support, clusters, and CO_2. DFT+U approach is proposed to improve the issue by shifting localized states. We have done a test[113] regarding the effect of U values (U=3.5, 4.0, and 4.5) on the Bader charge of CO_2 adsorption sites on reduced anatase TiO_2 (101) surface-supported Pt octamer. The results showed the maximum difference of around 1% charge transfer under DFT and DFT+U. Previous studies concerning the interactions of transition metal clusters[132, 133]/adsorbates[134] and perfect or reduced TiO_2 surfaces also showed similar charge distributions and cluster stability with these two methods.

We consider a 3x1 supercell of the anatase TiO_2 (101) surface with six trilayers, in which the bottom three layers were frozen, and the top three layers and metal clusters were relaxed; the vacuum region between the slabs was set to 12 Å. A Monkhorst-Pack [93] mesh of 2x2x1 k-points was used to sample the Brillouin zone for determining the CO_2 adsorption on the surfaces of TiO_2 – supported Pt clusters; the k-points setting was increased to 6x6x1 for the density of states (DOS) calculations. The electronic analysis includes atom-projected densities of states (p-DOS) within the energy range of interests, and the zero energy position represents Fermi level in the p-DOS figures. Density plots (DPs) with equal-density isosurfaces of 0.001e/ $Å^3$ are also studied to investigate the binding mechanism. Bader charge[135] is analyzed to understand the charge distribution of CO_2 adsorption sites. The vibrational frequencies are obtained from the frozen-phonon approach with a displacement of 0.015 Å for each atom in the CO_2 molecule. The adsorption energies of CO_2 on the model surface were calculated as the difference between the total energy of the composite system (CO_2 adsorbed on TiO_2 supported Pt clusters) and the sum of total energies of the isolated CO_2 and TiO_2 supported Pt surfaces. An more negative adsorption energy indicates more favorable adsorption.

5.3 Results

To enable investigating the effect of the cluster geometry (3D-2D) on the key precursor state for CO_2 photoreduction, the basic framework used in our previous study of Pt octamer/TiO_2 surfaces [113] is applied here to Pt tetramer and hexamer for completeness, which is necessary for later discussions such as geometric deformability and geometry (size)-key precursor state relationship. Reported here are the structural and electronic information of adsorbed CO_2 mainly in contact with Pt tetramer and hexamer: at the interface edge of the Pt clusters and TiO_2 surface (interface edge site, one O of CO_2 is interacting with the surface 5c-Ti atom while C or the other

O with Pt clusters); only on the Pt clusters (Pt only site: 1-Pt only and 2-Pt only sites in which CO_2 interacts accordingly with only one Pt and two Pt of the clusters).[113]

The optimized configurations and structural parameters of CO_2 on perfect surface-supported Pt tetramer and hexamer are given in Figure 5.1 and 2 while those on reduced surface in Figure 5.3 and 5.4, respectively. The adsorption energy, O-C-O angle of CO_2, and Bader charge difference of the adsorbed CO_2 molecule for each configuration on the cluster/perfect and cluster/reduced surfaces are reported in Table 1 and Table 2, respectively.

5.3.1 CO_2 Adsorption on Pt Clusters/Perfect TiO_2

Previously, we found Pt octamer/perfect TiO_2 surface offer adsorption site for bent form CO_2, and those CO_2 bind rather strongly compared to the CO_2 binding on the pure TiO_2 surface.[113] We find Pt hexamer/perfect surface follows the same trend, and even better in these two aspects; however, supported Pt tetramer does not exhibit such advantages. This makes Pt hexamer a potential candidate for CO_2 photoreduction on perfect anatase TiO_2 (101) surfaces. Note that the geometry of the deposited tetramer and hexamer are 3D geometry which is the same as the deposited octamer on the same surface.[58] On the supported Pt tetramer surface, three CO_2 adsorption sites (PT1-PT3 in Figure 5.1a-c) were found, whereas six (PH1-PH7 in Figure 5.2a-g) were found for hexamer case.

For tetramers, Pt only and interface edge sites were observed on the supported hexamer and octamer; however, only 1-Pt only site (PT1, Figure 5.1a) was obtained on the supported tetramer. The O-C-O angle for this adsorbate is not observed in other cases (Pt hexamers & octamers), and may be a characteristic signal for the CO_2 adsorption on the supported Pt tetramer. Bader charge analysis indicates the formation of the CO_2^- anion, and this is the only one found on this surface. PT2 & PT3 (Figure 5.1, b & c) are not in contact with the Pt tetramer and are not

favored. PT3 reveals the formation of carbonate-like molecule upon CO_2 adsorption, and a reconstruction of the TiO_2 surface occurs, in which the distance of the bridge oxygen and the 6c-Ti atom increased from 2.16 Å to 2.78Å (before and after CO_2 adsorption).

For hexamers, PH1, PH3, PH6, and PH7 (Figure 5.2, a, c, f, and g) are interface edge sites. PH1 is the most favored adsorption site among supported Pt clusters considered. The one Pt atom-CO_2 interaction was not found on the Pt octamer/perfect surface, but was observed on the Pt octamer/reduced surface. This suggests a higher geometry reconstruction ability of the Pt hexamer over the Pt octamer, and the presence of the oxygen vacancy can help the reconstruction of the cluster. The comparison of PH3 to the analogous one on the Pt octamer/perfect surface shows that the structural and electronic properties are quite similar to each other with an average O-C-O angle of 126.8°. PH7 is similar to PH3 but not a stable one. An apparent difference between PH3 and PH7 is the distance between C and the binding Pt atom in the top layer, and the charge accumulation at C is more in the latter. PH6 is barely stable, and similar to PT3 (Figure 5.1c) that a carbonate-like molecule is formed but with an interaction of the O of CO_2 and the cluster.

PH2 and PH4 are stable 1-Pt only and 2-Pt only sites. Compared to the corresponding ones found on the Pt octamer/perfect surface,[113] the structural parameters of PH2-like configurations are similar with an average O-C-O angle of 147.5°. The structural parameters of PH4-like configurations are quite similar with an average O-C-O angle of 136.3°. In terms of electronic properties, PH4-like configurations share comparable binding strengths, while PH2 has higher binding strength; also, PH2 & PH4 have more negative charge accumulation in C than the corresponding ones.

5.3.2 CO_2 Adsorption on Pt Clusters/Reduced TiO_2

Different from the Pt octamer case where the presence of the surface oxygen vacancy does not mitigate the CO_2 adsorption;[113] surprisingly, though many adsorption sites were obtained on Pt hexamer/reduced surface, most are not favored. Besides, only interface edge site is found on Pt tetramer/reduced surface. Note that unlike the perfect surface cases, tetramer and hexamer on reduced surfaces tend to exhibit planar geometries (2D), and this is also different from the Pt octamer on the reduced surface.[113] This leads to a conclusion that the geometry of the cluster is crucial to the CO_2 adsorption. On the Pt tetramer/reduced surface, three CO_2 adsorption sites (PTVo1-PTVo3 in Figure 5.3 a-c) were found, whereas seven (PHVo1-PHVo7 in Figure 4a-g) were found on the Pt hexamer/reduced surface.

For tetramers, PTVo1 (Figure 5.3a) is the interface edge site and the only Pt cluster related site. It is also the only stable configuration found on this surface with favored charge distribution in the adsorbed CO_2. PTVo2 & PTVo3 (Figure 5.3, b & c) are not Pt tetramer related sites and are not stable. PTVo3 is a bidentate carbonate specie with a tilted adsorbed CO_2 compared to corresponding ones found on the clean surface;[113, 122, 128] there are differences of the longer bonding distance of O of CO_2 with surface Ti and of the C with the surface O atoms by 0.21 and 0.16Å, respectively. Also, the O-C-O angle in PTVo3 is larger by 7.3°.

For hexamers, PHVo1 and PHVo5 (Figure 5.4, a & e) are 1-Pt only and 2-Pt only sites, and only PHVo1 is a stable site. Notably, the O-C-O angle in PHVo1 (154.7°) is close to that in PT1 (151.2°), and this angle similarity seems to relate to the geometry of the clusters. The geometry of the tetramer on the perfect surface (pyramid-like, Figure 5.1a) can be considered as part of the geometry of the hexamer on the reduced surface. Moreover, the trend of net charge transfers in both adsorbed CO_2 molecules is quite similar except the magnitude (ex, C: 0.341 &

0.337 for PHVo1 & PT1) which may be due to the number of the Pt atoms in the clusters or the presence of the oxygen vacancy. Surprisingly, in Pt octamer (perfect & reduced surfaces), hexamer (perfect surface), and tetramer (perfect surface) cases, all Pt only sites are stable, but PHVo5 is not stable; this may be due to PHVo5's smallest O-C-O angle (126.9°) among such sites found in Pt clusters studied.

PHVo2, PHVo3, PHVo4, and PHVo6 (Figure 5.4, b, c, d, and f) are interface edge sites, and PHVo2 is the only favored one. All binding with one Pt atom at these interface edge is different from octamer/reduced surface where interactions with two Pt atoms exist. In this group, the O-C-O angles lie between 131.8° and 140.4°. Comparing the structural parameters and electronic properties of this group to stable interface edge ones in Pt octamer and hexamer cases, no significant differences are found; hence, the dimension of the cluster geometry (2D or 3D) seems to play a significant role in the CO_2 adsorption.

To sum up, considering CO_2 adsorption associated with Pt clusters (tetramer, hexamer, and octamer[113]), almost all adsorbed CO_2 species are bent forms, and have appreciable acquisition of negative charge in C of CO_2. Also, the CO_2 binding strength is rather strong compared especially to clean stoichiometry TiO_2 surface. It is revealed that subnanometer Pt clusters are able to bring new electronic property on the conventional TiO_2.[113] However, this does not always hold true for Pt hexamer, because on the reduced surface most configurations are not favored in terms of total energy. The same is true for Pt tetramer due to its lack of availability of adsorption sites.

Note that bridged carbonate configurations in PT2, PTVo2, PH5, and PHVo7 (Figure 5.1b, Figure 5.2b, Figure 5.3e, and Figure 5.4g) are the same CO_2 configuration found in perfect anatase TiO_2 (101),[122, 128] Pt octamer/anatase TiO_2 (101).[113] This configuration stays stable on

reduced TiO_2 surface, and supported Pt hexamer/octamer (perfect surface). Possible factors are electrostatic competition between attractive (surface Ti - O of CO_2) and repulsive (surface Ti - C of CO_2) interactions, and charge transfer to CO_2 from Ag/Pt clusters.[113] Notably, CO_2 in PTVo2 has appreciable negative charge accumulation at C (different from most of the corresponding configurations) perhaps due to the closer contact of CO_2 with the Pt tetramer as reflected from the distances of C and Pt tetramer being 2.42 and 4.00 Å for PTVo2 and PT2, respectively.

5.4 Discussion

5.4.1 Geometry Change of Adsorbed Clusters (2D->3D)

Observing adsorbed tetramer and hexamer on the reduced surface, both geometries tend to evolve toward flat (2D) geometry as compared to 3D geometries of both clusters on the perfect surface. We find that the driving force for the pro-2D geometries is due to the tendency of Pt tetramer and hexamer to form bonding orbitals with surface Ti atoms (including 4c-Ti and 5c-Ti due to the presence of the oxygen vacancy). This is consistent with our previously developed binding mechanism of Pt_n (n=2, 4, and 8) on perfect anatase TiO_2 (101) surface,[58] which suggests that Pt clusters have a strong tendency to bind with surface Ti atoms but lesser tendency to bind with 2c-O atoms; the underlying factor is the sufficient orbital overlaps of Pt clusters and surface Ti atoms to form bonding orbital.

To see this, we examine the p-DOSs of O, Ti, and Pt atoms of the supported tetramer and hexamer (Figure 5.5), the resonant peaks can be seen consisting of Ti, O, and Pt atoms, which suggests the disposition of Pt clusters to bind with Ti and O atoms. Further investigations of density plots (DPs) show bonding orbitals formed by the cluster and 4c-Ti; for example, DP at -2.05eV in Figure 5.5a shows Pt1 of the tetramer binding with 4c-Ti, and DP at -0.58eV in Figure 5.5b shows Pt2 of the hexamer binding with 4c-Ti. The binding with 5c-Ti can also be

seen; for example, DP at -1.60eV in Figure 5.5a shows Pt2 of the tetramer binding with 5c-Ti, and DP at -1.77eV in Figure 5b shows Pt5 of the hexamer binding with 5c-Ti. Our result is also consistent with other DFT calculations. Gong et al.[79] obtained the results that Pt_n(n=1-3) prefer to bind with the surface Ti & O atoms of anatase TiO_2(101), and 4c-Ti & 5c-Ti atoms are favored in the presence of oxygen vacancy. The study of Pt_n(n=4-8) supported on rutile TiO_2(110) surface[77] also pointed out the importance of the Pt-Ti bond on the cluster-support binding strength, and two-layer structure are preferred for Pt_5-Pt_8 except Pt_6 favoring planar geometry.

5.4.2 Geometry (Size)-Related Binding Mechanism

Prior investigations of the binding mechanism regarding CO_2 adsorption on perfect/reduced anatase TiO_2 (101)-supported Ag & Pt octamers[113] found that for CO_2 adsorption in contact with Pt octamers, the binding is facilitated by the hybridization of the molecular orbitals of CO_2 with d orbitals of the Pt atoms. The results presented here suggest that structural fluxionality plays an important role in the adsorption as well as the binding competition between Pt atoms with the adsorbate.

First, we retouch the electronic analysis of the Pt related binding site (interface edge, 2-Pt only, and 1-Pt only sites). We have shown DOS and DPs of the interface edge and Pt only sites involving two Pt atoms;[113] in this study those of the Pt only site involving one Pt atom (PH2 in Figure 5.2b) are shown in Figure 5.6 to clarify the electronic interactions. Prior work of the adsobate-transition metal interaction[110, 163] suggested that the hybridization of adsorbate valance states with the valance states of the metal surface atoms leads to the bonding and antibonding states. In the H-metal (Ni, Cu, Pt, and Au) surface systems, the dominating H 1s-metal d bonding states lie within -10 and -5 eV.[163] In the CO_2-TiO_2 supported Pt hexamer interaction, the resonance peaks of Pt and CO_2 in figure 5.6a suggest such bonding states also lying mainly

between -10 and -5 eV, which is the same range also found in CO_2-TiO_2 supported Pt octamer.[113] Furthermore, in Figure 5.6b the p-DOS of s and p states of CO_2 show that the valence states of CO_2 between -10 and -5 eV are consisted of s and p states (no d states involved) with s states dominating in lower energy levels and p states in higher energy levels. DP1 ($2\sigma_g$), DP2, and DP3 & DP4 ($1\pi_u$) in Figure 5.6, a & b show CO_2 (s & p)-supported Pt hexamer bonding states consisted of bonding orbitals of CO_2 and d states of the Pt atom. This is consistent with the CO_2-supported Pt octamer interaction of the interface edge and Pt only (involving two Pt atoms) sites. Therefore, a general conclusion is that for CO_2-TiO_2 supported Pt subnanometer cluster CO_2 s&p - metal d are the dominating bonding states.

The binding tendency of the adsorbate with the support would be misleading if only the geometry is considered [58]. Pt clusters show appreciable binding inclination with surface O atoms of anatase TiO_2 (101) based on the observed geometries; however, DPs show that the root binding interaction comes from Pt clusters with the surface Ti atoms. The DPs in Figure 5.6 show that only one Pt atom is involved in this adsorption at Pt only site. The CO_2 adsorption energies at Pt only sites involving one and two Pt atoms suggest that the CO_2 binding strength is not related to the number of Pt atoms involved; also, the interface edge sites exhibit the strongest CO_2 binding strength probably due to extra bonding stabilization from CO_2 with surface O atoms.

5.4.2.1 Structural Fluxionality

Next, we investigate geometry-dependent binding factors. The geometry reconstructions are apparent for supported Pt clusters upon CO_2 adsorption, especially for Pt clusters of 3D geometry. For example, comparing PH1 and PH5 in Figure 5.2, a & e (PH5 is almost the same Pt hexamer geometry of the most favored deposited hexamer when no CO_2 molecule is present), leads to the conclusion that the Pt hexamer in PH1 undergoes appreciable geometry modification

during the CO_2 adsorption. This geometry reconstruction is due to structural fluxionality[118] ,one characteristic of the subnanometer metal clusters. During CO_2's interaction with the cluster, the cluster tends to vary its geometry to meet the maximum orbital overlaps of the cluster and CO_2 for the formation of the bonding orbitals to sustain their binding.

To measure this, we define a quantity called displacement (per Pt atom) to represent the extent of the cluster's structural fluxionality as the equation below:

$$\text{Displacement (structural fluxionality)} = \frac{\sum_n \sqrt{(X_{nf}-X_{ni})^2+(Y_{nf}-Y_{ni})^2+(Z_{nf}-Z_{ni})^2}}{n}$$

where X, Y, and Z represent the coordinates of the n^{th} atom in the cluster; i and f represent the initial and final states; and n= 1-N, where N equals the cluster size. Considering the CO_2 adsorption configurations obtained in this (supported Pt tetramer and hexamer) and our previous (supported octamer[113]) works, we evaluate the displacement of 3D, 3D/2D, and 2D Pt clusters (shown in Figure 5.7a for interface edge sites and in Fig. B8 of Appendix B for Pt only sites). Pt only sites show comparable fluxionality capability for all three Pt cluster geometries (3D, 3D/2D, and 2D) upon CO_2 adsorption, which is apparent because the adsorbate can easily modify itself instead of deposited clusters during the adsorption.

However, at interface edge sites 3D, 3D/2D, and 2D show different fluxionality capability. 3D geometry [PO1(BP1)[113], POVo1(BPVo1)[113], POVo4(BPVo4)[113], POVo6(BPVo6)[113], PH1, PH3, and PH7] tend to have high displacement values on average, indicating the large geometry changes during the CO_2 adsorption. The 3D/2D geometry (PHVo2, PHVo3, PHVo4, and PHVo6) show smaller displacements; but, as seen from the optimized geometries (Figure 5.4), the displacements mostly come from horizontal shifting. The 2D geometry exhibits limited reconstruction. This is because the 2D structure binds tightly with surface atoms, restricting its self-modification, while top layer atoms of the 3D structure are less

restricted, giving greater freedom for 3D clusters to modify itself. Displacement (structural fluxionality) is also related to the CO_2 binding strength. The displacements of stable interface edge sites are given in Figure 5.7b. As can be seen, there is a positive correlation of displacement and the CO_2 adsorption energy, which means that the more the cluster modify its geometry, the more the maximum orbital overlaps are reached, resulting in stronger CO_2 binding strength.

5.4.2.2 Binding Competition

Though the hybridization of bonding states of CO_2 with d states of the Pt atoms sustains the binding as detailed above, it can also cause instability in the CO_2 adsorption. Considering the major bonding states of the CO_2-Pt clusters/TiO_2 (-10 eV to -5 eV), the DP at -6.00 eV of PHVo5 (Figure 5.8a) indicates the presence of two pulling forces against each other on the CO_2 (due to bonding interactions of Pt1 and Pt6 individually with the CO_2 molecule) that makes CO_2 unstable. This is made clearer by comparing the Pt-C-Pt angle to other corresponding stable ones. The Pt-C-Pt angles in PH4 (Figure 5.2d) and in those on supported Pt octamers[113] are 71.3°, and 64.9° & 64.3°, which is considerably smaller than 94.8° of the metastable PHVo5. It is understood that the net force acting on CO_2 with smaller Pt-C-Pt angles results in both Pt atoms stabilizing the adsorbate; on the other hand, with larger angles Pt-CO_2 stabilizing forces become smaller, and the forces start to cancel each other due to both Pt atoms competing with each other to bind with the adsorbate. Another evidence is from PHVo6 (Figure 5.4f). Looking at the DP at -6.48 eV (Figure 5.8b), it is seen that in addition to CO_2's binding with Pt6, the binding with surface O atoms is also present (which is the reason of the titled CO_2); it is suggested that the latter interaction may disturb sufficient orbital overlaps of the CO_2 with lopes of the d state of the Pt atom.

The reason that CO_2 is not able to bind on the top surface of the 2D Pt tetramer (refer to Figure 5.3) may be due to two factors: limited structural fluxionality and binding competition. One scenario is that CO_2 diffuses from the bulk to the 2D surface, lying horizontally. The binding of C with a Pt atom initiates the adsorption process pulling the CO_2 molecule, followed by the other Pt atom trying to bind with the adsorbate. Then, each Pt atom starts to attempt the maximum overlap with CO_2 orbitals, but bindings of Pt with surface Ti atoms restrict the geometry modification of the Pt tetramer to satisfy both overlaps. Each pulling force under large Pt-C-Pt angle starts to cancel each other, gradually resulting in weak CO_2 stabilizing force on the surface; finally, CO_2 leaves the surface to the bulk.

5.4.3 CO_2 Bond Breaking Tendency

An evaluation of the CO_2 bonding breaking tendency is possible by current characterization capabilities.[125, 164-166] These studies shed light on the nature of CO_2 photoreduction on subnanometer metal clusters based photocatalyst. Freund summarized the characterization tools such as LEED and NEXAFS to gain information of CO_2 geometry.[125] NEXAFS was used to show the geometries of CO_2 species on Ni(110).[164] IRRAS along with computation results also reveal the CO_2 structure on rutile TiO2(110)[165] and ZnO(10$\bar{1}$0).[166] To promote the formation of light hydrocarbons via CO_2 photoreduction, the breaking of the C-O bond of the CO_2 molecule is a crucial factor. We find that the C-O bond breaking tendency is correlated with the charge transfer to C and the O-C-O angle of CO_2.

The C-O bond breaking is attributed to the electron population to antibonding orbitals of the CO_2 molecule. We have shown such bond breaking capability of neutral TiO_2 - supported Pt octamers.[113] A further evidence for antibonding states below Fermi level is shown in DP5 (Figure 5.6a) which suggests the hybridization of the nonbonding CO_2 orbital (HOMO, $1\pi_g$) with

the Pt d states. This conclusion is also supported from a study regarding the chemistry of the CO_2 molecule: bent form CO_2 resulting in the lowering of the $2\pi_u$ energy, even lower than $1\pi_g$.[125] Therefore, we consider all the CO_2 adsorption sites in contact with the Pt clusters: tetramer (PT1 in Figure 5.1a, and PTVo1 in Figure 5.3a), hexamer (PH1-PH4 & PH7 in Figure 5.2, a-d & g, and PHVo1-PHVo6 in Figure 5.4a-f), and octamer (BP1-BP3 in Figure 5.1d-f, and BPVo1-BPVo4 & BPVo6 in Figure 5.2, d-g & i in our previous work[113]). A correlation between the negative charge accumulation at C of CO_2 and the C-O bond length is found, as shown in Figure 5.9a. The more electron accumulation at C is, the longer the C-O length, and this can be attributed to the filling of antibonding states of CO_2. A DFT calculation using Gaussian09 program package[94] with B3LYP functional[122] comparing CO_2 and CO_2 anion was performed to reveal the role of C in the hybridization of antibonding states. Natural bond orbital (NBO) charge[167] shows C of CO_2 possessing 1.02+ with an average C-O bond length of 1.16Å, while C of CO_2^- anion possessing 0.50+ with an average C-O bond length of 1.23Å, indicating that as C gains electron, the length of C-O bond also increases. Another correlation of the C-O bond length is found with the angle of O-C-O of CO_2 among the configurations just mentioned, shown in Figure 5.9b. The smaller the angle is, the longer the C-O bonds. As more electrons accumulate at C of CO_2, these electrons tend to repulse with the electrons in C-O bonds, resulting in smaller O-C-O angle. This is similar to the repelling character of lone pairs that makes H_2O a bent structure. Note that among 12 interface edge and 9 Pt only sites, four out of the five longest C-O bonds are interface edge, while four out of the least five longest C-O bonds are Pt only sites. This suggests that the interface site of the anatase TiO_2 (101) - supported Pt clusters has higher bond breaking tendency over the Pt only sites.

5.4.4 Vibrational Frequency

The vibrational frequencies of symmetric (ν1) and asymmetric (ν3) stretching for adsorbed CO_2 on several metal oxide surfaces have shown relatively good agreement between experimental[143, 144] and computational[113, 122, 124, 128] results; the reported experimental values for the CO_2^- anion were in the ranges of 1219-1247 and 1640-1670 cm^{-1} on P25[143]/anatase TiO_2[144, 145]. We have previously revealed that on supported Pt octamer surfaces there are correlations of ν2 mode and charge accumulation at C of bent-form CO_2, and of ν3 mode and O-C-O angle of CO_2.[113] We find that when incorporating adsorbed CO_2 species on supported tetramer (PT1 in Figure 5.1a and PTVo1 in Figure 5.3a) and hexamer (PH1-PH4 in Figure 5.2a-d and PHVo1-PHVo2 in Figure 5.4, a & b) along with octamer case (PO1-PO3 representing BP1-BP3 in Figure 5.1d-f, and POVo1-POVo4 representing BPVo1-BPVo4 in Figure 5.2d-g of our previous work[113]), these two correlations still hold true as shown in Figure 5.10, a & b. The sites with the most charge accumulations at C of the values around 0.600e have the ν2 mode in the range of 760-772 cm^{-1}, while smaller charge accumulations around 0.35e lie in 574-602 cm^{-1}. Likewise, smaller O-C-O angles around 126° lie in 1483-1529 cm^{-1} and larger O-C-O angles around 151° in 1918-1996 cm^{-1}. We suggest these two trends are generalized in supported subnanometer Pt clusters, and ν2 & ν3 modes can be reliable indicators for electronic and geometry properties of adsorbed CO_2 species.

More detailed information of Pt related adsorption sites (interface edge, one Pt, and two Pt sites) is found from ν2 and ν3 modes on top of our prior analysis.[113] Previously, ν2 in and below the range ~750-800 cm^{-1} indicate interface edge adsorption and Pt octamer related adsorption, respectively; interface edge sites were also revealed by smaller ν3 values (~1500-1540 cm^{-1}). In this study, we find that the lower ν2 tends to indicate one Pt only adsorption site

and higher ν2 tend to indicate interface edge sites. ν2 in the lower range (~570-625cm^{-1}) represents one Pt atom adsorption site; in the higher range (~760-775 cm^{-1}), ν2 signify interface edge sites as shown in Figure 5.10a. In between these two ranges, there is a mixed state of interface edge and two Pt atoms sites. A similar trend as ν2 mode is also found for ν3 mode as shown in Figure 5.10b. ν3 in the higher range (~1910-2000 cm^{-1}) represents one Pt atom adsorption site; in the lower range (1480-1540 cm^{-1}), ν3 tend to indicate interface edge sites. Likewise, a mixed state of interface edge and two Pt atoms sites also lies in between the ranges. In sum, lower ν2 and higher ν3 reveal one-Pt atom site, while higher ν2 and lower ν3 reveal interface edge site along with two-Pt atoms sites in the middle ranges.

There is some ambiguity when analyzing ν2 mode (below ~800 cm^{-1}) for CO_2 adsorption sites in contact with Pt clusters on supported tetramer and hexamer.[113] As shown in the Fig. B9 in Appendix B, though all ν2 modes of the direct TiO_2 surface sites are above ~800 cm^{-1}, the threshold is small. Promisingly, ν1 mode seems to be a more reliable indicator to differentiate Pt associated sites from direct TiO_2 surface sites. Shown in Figure 5.10c are stable CO_2 adsorption sites on the supported Pt tetramer, hexamer and octamer: Pt related (the same sites considered in Figure 5.10, a & b) and direct TiO_2 surface (PT2 in Figure 5.1b, PH5 & PH6 in Figure 5.2, e & f, and PO4 representing BP4 in Figure 5.1g and POVo5 representing BPVo5 in Figure 5.2h of our previous work[113]) sites. As can be clearly seen, ν1 larger than 1250 cm^{-1} represent direct TiO_2 surface sites, while below 1200 cm^{-1} there is a collection of Pt associated sites; the lower vibration of the latter may be due to CO_2 stretching inhibited by CO_2'sbonding interactions with Pt clusters as can be revealed by DPs in Figure 5.6.

We have shown the correlations of the C-O bond breaking tendency with negative charge accumulation at C and with O-C-O angle of CO_2, and the latter two properties well correspond to

vibrational frequencies (ν2 and ν3). Therefore, it is desirable to develop an experimental obtainable signal to predict promising CO_2 adsorption sites/configurations with high C-O bond breaking tendency. Plotted in Figure 5.10, d & e are the average C-O bond length verse ν2 and ν3 of stable CO_2 adsorption sites on supported tetramer, hexamer, and octamer (the same sites considered in Figure 5.10, a & b). Good relation of ν2 and ν3 with C-O bond length can be easily seen. Higher ν2 and lower ν3 frequencies suggest the adsorbed CO_2 with longer C-O bond length. We believe these correlations would offer valuable information to experimental maneuver in understanding the adsorption sites, electronic properties, and catalysis of adsorbed CO_2 species.

5.5 Conclusions

The geometry (2D or 3D) of Pt tetramer, hexamer, and octamer supported on anatase TiO_2 (101) can significantly affect the CO_2 adsorption based on DFT calculations. Compared to 2D Pt clusters, 3D Pt clusters provide more binding sites for bent form CO_2 with electron accumulated at C, which aids in the formation of key dissociation precursor leading to the products of CO_2 photoreduction. This geometry-dependent CO_2 adsorption may be explained by structural fluxionality and binding competition.

Structural fluxionality is quantified by defining it as displacement (per atom). We find that at interface edge site 3D clusters tend to have high structural fluxionality than pro-2D clusters. This is because the top layer atoms of 3D cluster are freer to move as compared to 2D cluster. High fluxionality capability is also related to stronger CO_2 binding, as greater geometry reconstruction enables maximum orbital overlaps of Pt clusters and CO_2. Binding competition occurs when more than one Pt atoms attempt to bind with CO_2, which may mitigate maximum orbital overlaps among each Pt-CO2 bonding interaction, leading to CO_2 instability. The failure for CO_2 to adsorb on the pro-2D surface can be understood by the structural fluxionality and

binding competition. When Pt tetramer and hexamer deposit on perfect anatase TiO_2 (101), they exhibit 3D structure, whereas on reduced surface, interestingly, pro-2D structure is favored. This is due to Pt cluster's strong disposition to bind with the surface Ti atoms; in addition to 5c-Ti and 6c-Ti, oxygen vacancy creates 4c-Ti and more 5c-Ti atoms on anatase TiO_2 (101) surface, which make Pt tetramer and hexamer flatter in order to easily bind with the surface Ti atoms.

DOS and DP suggest that the main bonding states for CO_2-TiO_2 supported subnanometer Pt cluster come from CO_2 s&p - metal d state in the range -10 and -5 eV (compared to Fermi level). In comparison of the DOS, DP, and the energetics of interface edge and Pt only (involving one and two Pt atoms) sites on supported Pt octamer and hexamer, it is suggested that CO_2 binding strength is not correlated with the number of Pt atoms involved. The interface edge site has stronger CO_2 binding strength than Pt only sites, and such enhancement may be from extra bonding interaction with the surface oxygen atom. Furthermore, to make CO_2 activation feasible leading to the products of CO_2 photoreduction, C-O bond breaking is critical, which results from the filling of antibonding orbitals of the CO_2 molecule.[113] We find that this bond breaking tendency is related to charge accumulation at C and O-C-O angle of adsorbed CO_2 species.

The electronic and geometric properties of the adsorbed CO_2 can be revealed by vibrational frequencies. In addition to CO_2 adsorption sites on Pt octamer (previously reported[113]), the correlations of ν2 and accumulation at C, and of ν3 and O-C-O angle of adsorbed CO_2 also apply to those on Pt tetramer and hexamer. We further find that ν1, ν2, and ν3 can be used as reliable indicators to more clearly identify CO_2 adsorption sites. For ν1, 1200 ~1250 cm^{-1} is the identifying range; above the range it represents the direct TiO_2 surface site, while below it represents Pt associated sites. For ν2, the lower range (~570-625cm^{-1}), higher range (~760-775

cm^{-1}), and in-between these two ranges indicate one-Pt atom, interface edge, and mixed interface edge/two-Pt atoms adsorption sites, respectively. For ν3, the higher range (~1910-2000 cm^{-1}), lower range (1480-1540 cm^{-1}), and in-between these two ranges indicate one-Pt atom, interface edge sites, and mixed interface edge/two-Pt atoms adsorption sites, respectively.

In summary, we have identified two geometry-dependent factors that affect the formation of the key dissociation precursor state for CO_2 photoreduction. The driving force for the reconstruction of the Pt clusters (2D or 3D) is discussed as well as the C-O bonding breaking tendency. Vibrational frequencies are proposed as indicators to gain insights into the adsorption sites, electronic properties, and catalysis of adsorbed CO_2 species to help practical design of promising CO_2 reduction photocatalyst in subnanometer metal/semiconctor framework.

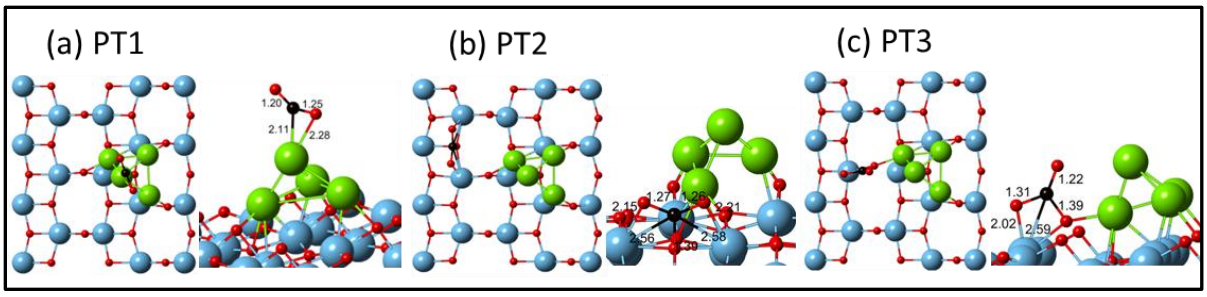

Figure 5.1 Stable CO_2 adsorption configurations on the perfect anatase TiO_2(101) surface in the presence of Pt tetramers (O in red, C in black, Ti in blue, and Pt in green. The numbers indicate the bond lengths in Å).

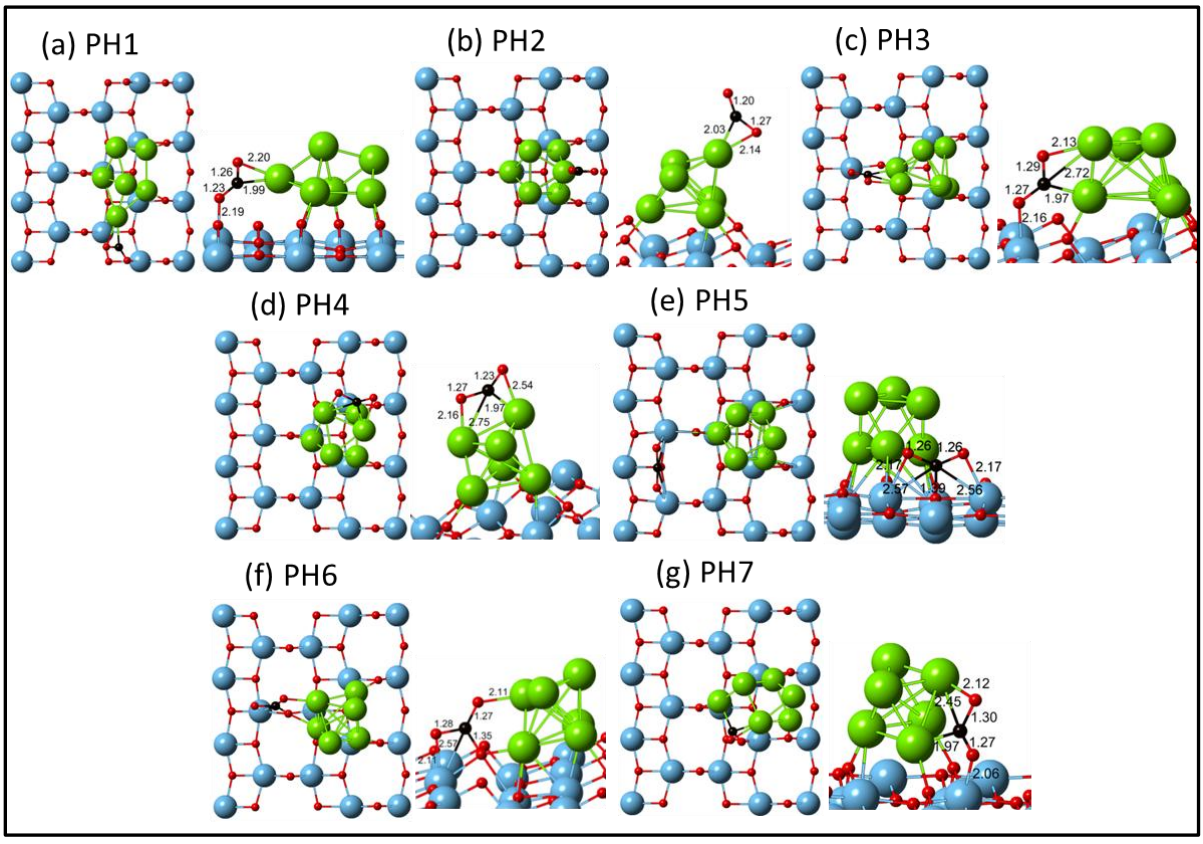

Figure 5.2 Stable CO_2 adsorption configurations on the perfect anatase TiO_2(101) surface in the presence of Pt hexamers (O in red, C in black, Ti in blue, and Pt in green. The numbers indicate the bond lengths in Å).

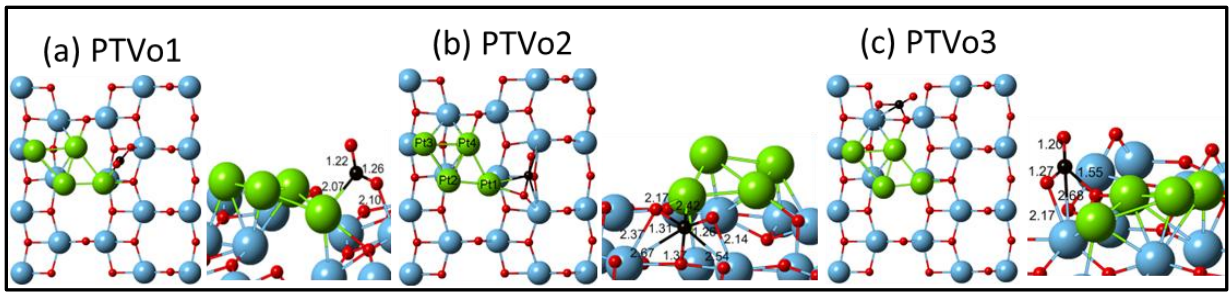

Figure 5.3 Stable CO_2 adsorption configurations on the reduced anatase TiO_2(101) surface in the presence of Pt tetramers (O in red, C in black, Ti in blue, and Pt in green. The numbers indicate the bond lengths in Å).

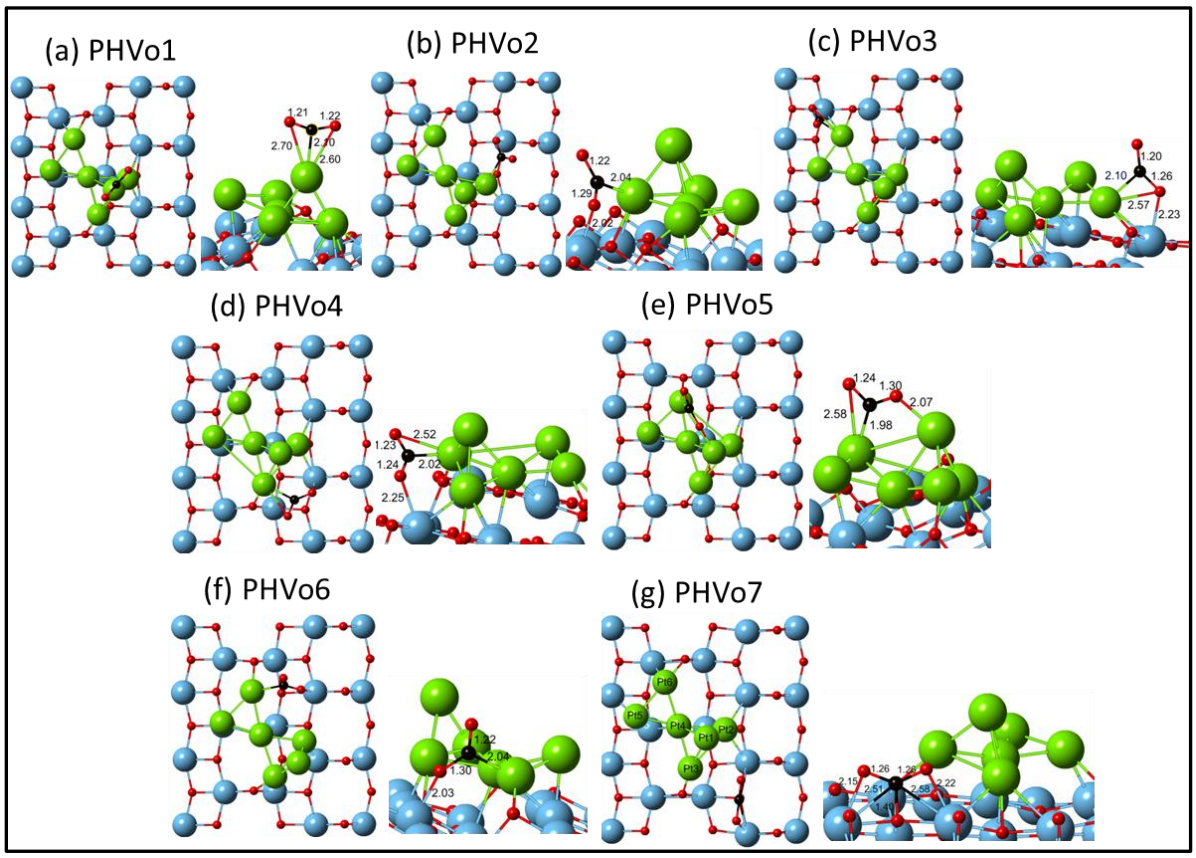

Figure 5.4 Stable CO_2 adsorption configurations on the reduced anatase TiO_2(101) surface in the presence of Pt hexamers (O in red, C in black, Ti in blue, and Pt in green. The numbers indicate the bond lengths in Å).

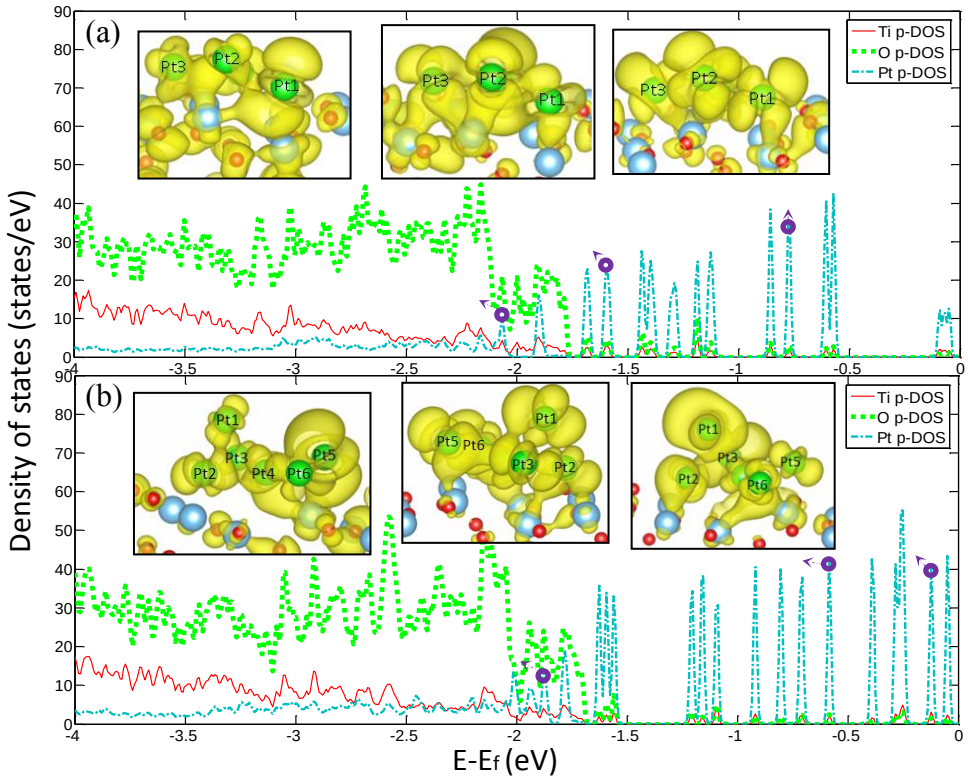

Figure 5.5 p-DOSs (Ti, O, and Pt) and density plots of reduced anatase TiO_2(101) surface-supported Pt clusters: (a) tetramer, and (b) hexamer. The insets show the density plots at corresponding positions: (a) -0.77, -1.60, and -2.05eV and (b) -0.12, -0.58, and -1.77eV (Shown in the figures correspond to spin up).

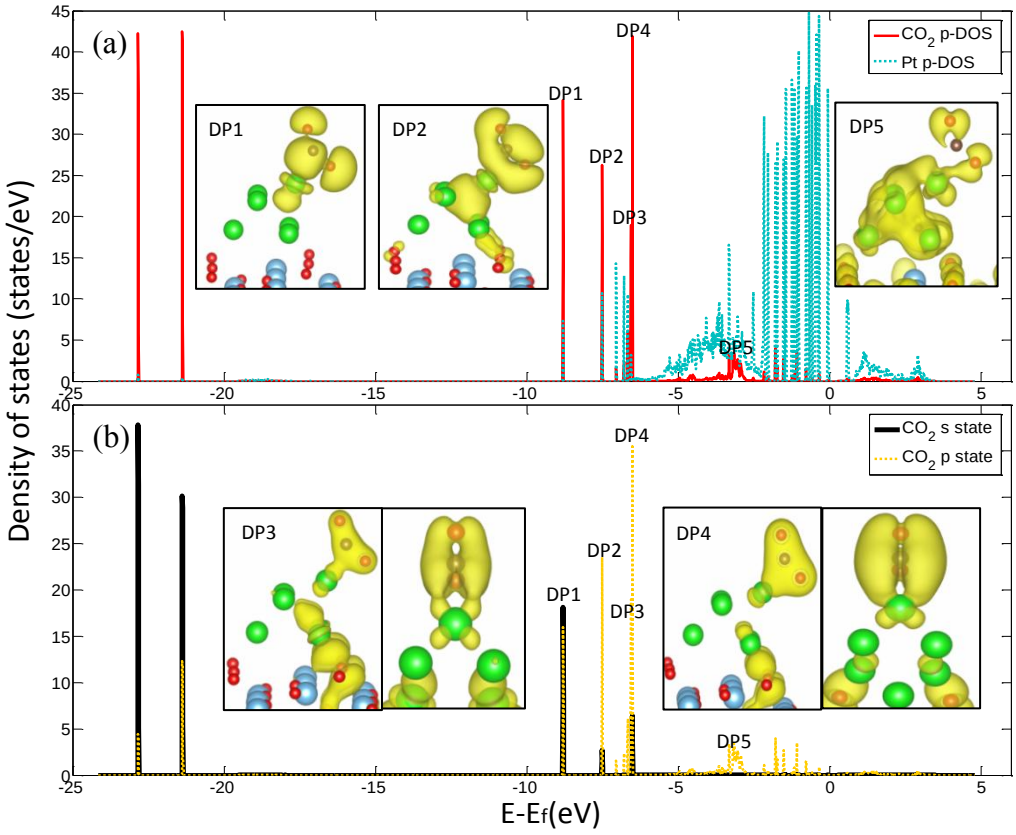

Figure 5.6 p-DOSs and associated density plots (DPs) of specific states formed upon CO_2 adsorption directly on the Pt hexamer involving one Pt atom (PH2): (a) p-DOSs of the adsorbed CO_2 and Pt; (b) p-DOSs of s and p states of the adsorbed CO_2. DP1-DP5 are the same states in both figures accordingly at -8.80, -7.50, -6.66, -6.55, and -3.30 eV (Shown in the figures correspond to spin up).

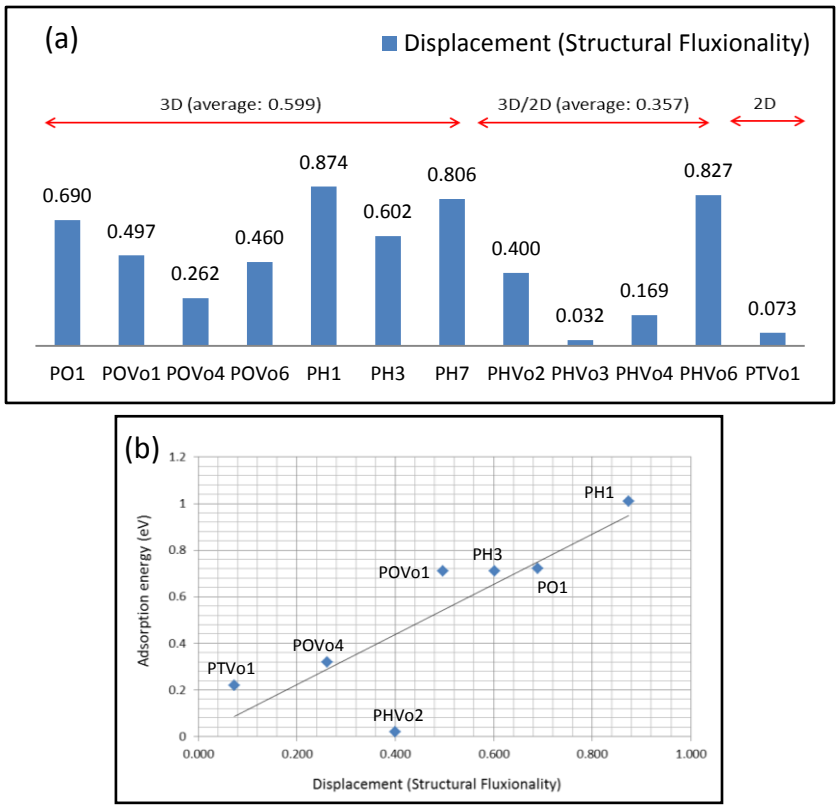

Figure 5.7 (a) Displacement (structural fluxionality tendency) of all CO_2 adsorption sites at the interface edge; (b) Displacement verses adsorption energy of stable interface edge sites on the anatase TiO_2(101) supported tetramer, hexamer, and octamer (octamer[113]: PO1(BP1), POVo1(BPVo1), POVo4(BPVo4), and POVo6(BPVo6); PO, PH, and PT represent Pt octamer, hexamer, and tetramer; Vo represents an oxygen vacancy).

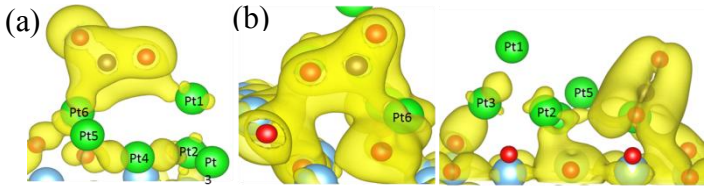

Figure 5.8 (a) The DP at -6.00 eV of PHVo5; (b) the DP at -6.48 eV of PHVo6.

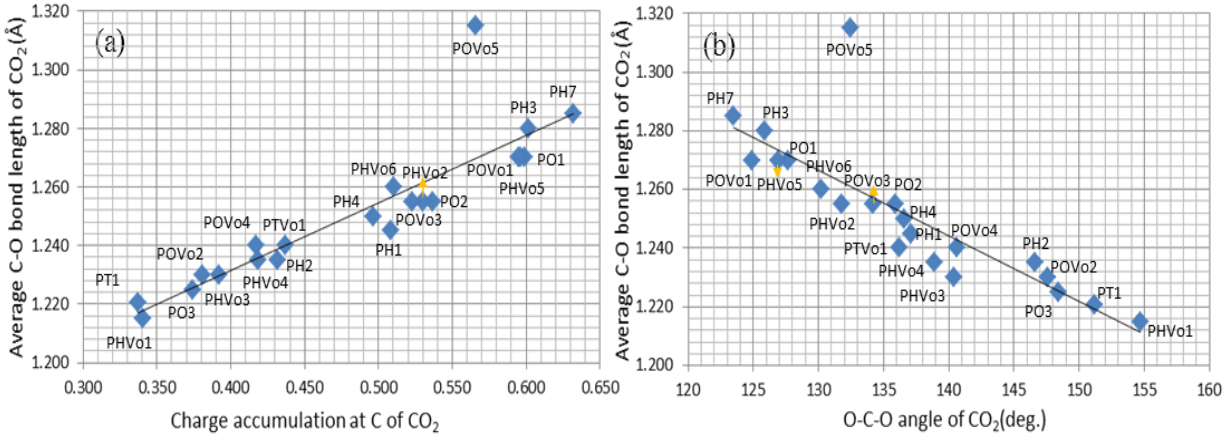

Figure 5.9 Correlations between the average C-O bond length (bond breaking tendency) and (a) the negative charge accumulation at C, and (b) O-C-O angle of the adsorbed CO_2 species in contact with the supported Pt tetramer, hexamer, and octamer[113].

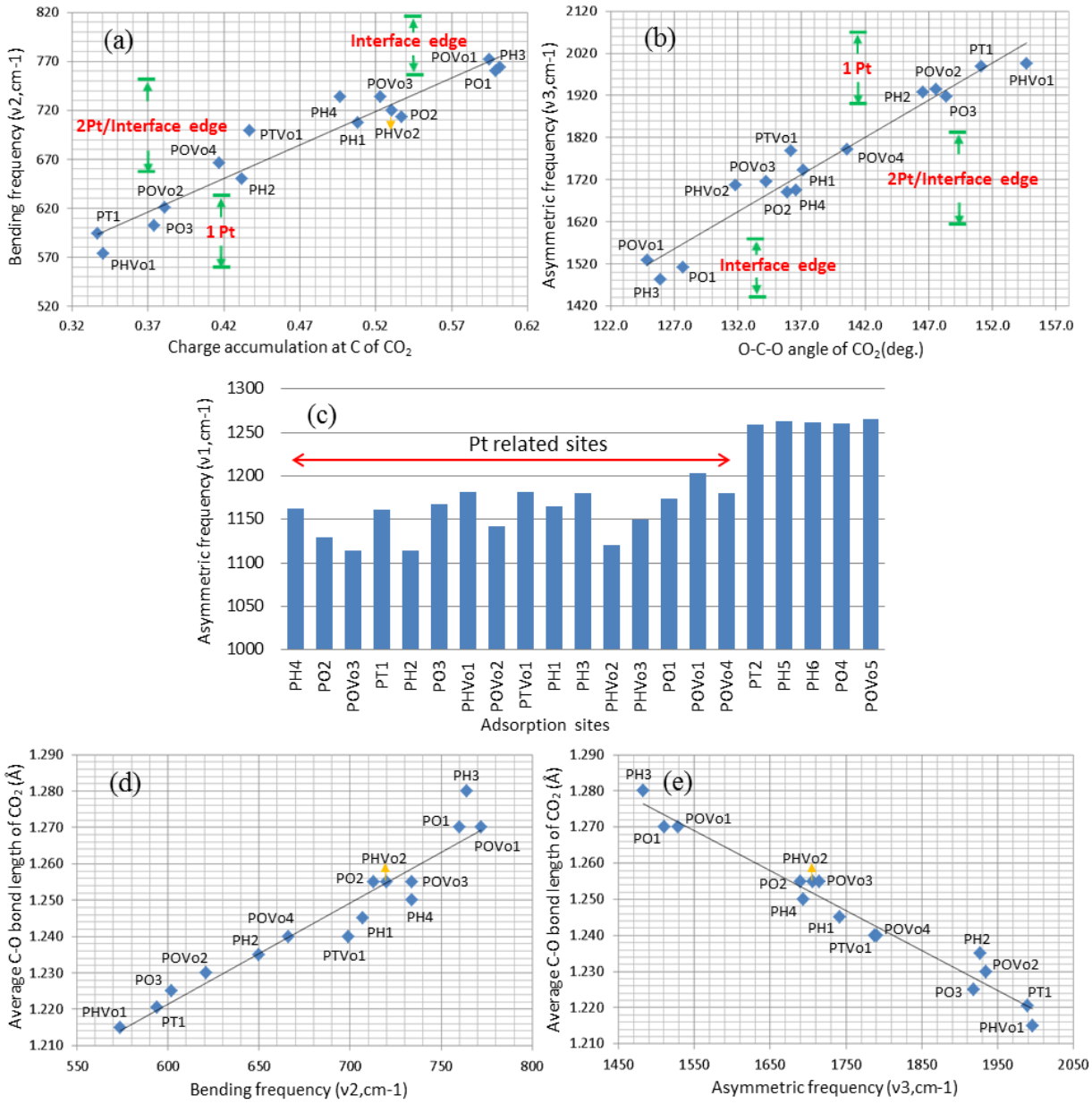

Figure 5.10 Correlations between (a) the bending frequency (v2) and the negative charge accumulation at C of CO_2, and between (b) the asymmetric stretching frequency (v3) and the O-C-O angle of CO_2. (c) The symmetric stretching frequency (v1) verses all the stable adsorption sites. Correlations between average C-O bond length (bond breaking tendency) and (d) v2, and (e) v3 [(a)(b)(d)(e) from Pt related sites and (c) from all the stable sites on supported tetramer, hexamer, and octamer; Octamer[113]: PO1(BP1), POVo1(BPVo1), POVo4(BPVo4), and POVo6(BPVo6); PO, PH, and PT represent Pt octamer, hexamer, and tetramer; Vo represents an oxygen vacancy].

Table 5.1 Calculated properties[a] based on CO_2 adsorption configurations on perfect anatase TiO_2(101) in the presence of Pt tetramer and hexamer.

Ads. Config.	-Eads(eV)	∠OCO(deg.)	Δe of CO2			ν(CO2)(cm-1)		
			C	O	O	ν1	ν2	ν3
PT1	0.22	151.2	0.337	-0.078	-0.023	1161	594	1989
PT2	-0.01	133.5	-0.002	0.036	0.061	1259	801	1663
PT3	-0.07	130.0	0.006	0.075	-0.013	1161	788	1695
PH1	1.01	137.1	0.508	0.061	-0.111	1165	707	1742
PH2	0.72	146.6	0.432	-0.025	-0.109	1114	650	1927
PH3	0.71	125.9	0.602	0.037	-0.064	1180	764	1483
PH4	0.64	136.6	0.497	-0.039	-0.051	1163	734	1694
PH5	0.08	133.3	-0.012	0.055	0.047	1263	804	1654
PH6	0.01	125.9	-0.023	0.020	-0.001	1262	833	1541
PH7	-0.04	123.5	0.632	0.058	-0.063	1163	738	1434

[a]Values represent the adsorption energy, O-C-O angle of CO_2, difference of Bader charge of CO_2 molecule upon adsorption, and vibrational frequencies of symmetric (ν1), bending (ν2), and asymmetric (ν3) stretching modes (Δe >0 means electron accumulation; PT and PH represent Pt tetramer and Pt hexamer, respectively).

Table 5.2 Calculated properties[a] based on CO_2 adsorption configurations on reduced anatase TiO_2(101) in the presence of Pt tetramer and hexamer.

Ads. Config.	-Eads(eV)	∠OCO(deg.)	Δe of CO2			ν(CO2)(cm-1)		
			C	O	O	ν1	ν2	ν3
PTVo1	0.22	136.2	0.437	0.038	-0.028	1182	699	1788
PTVo2	-0.06	131.1	0.114	-0.003	0.033	1191	762	1532
PTVo3	-0.97	137.4	0.117	0.048	0.015	1163	699	1858
PHVo1	0.16	154.7	0.341	-0.053	-0.047	1181	574	1996
PHVo2	0.02	131.8	0.530	0.000	0.011	1121	720	1706
PHVo3	-0.03	140.4	0.392	-0.004	-0.004	1150	648	1858
PHVo4	-0.13	138.9	0.419	-0.041	0.044	1194	686	1774
PHVo5	-0.33	126.9	0.596	-0.034	-0.053	1124	740	1593
PHVo6	-0.41	130.2	0.510	-0.006	0.036	1095	714	1710
PHVo7	-0.83	133.5	-0.017	0.050	0.040	1262	792	1680

[a]Values represent the adsorption energy, O-C-O angle of CO_2, difference of Bader charge of CO_2 molecule upon adsorption, and vibrational frequencies of symmetric (ν1), bending (ν2), and asymmetric (ν3) stretching modes (Δe >0 means electron accumulation; PT and PH represent Pt tetramer and Pt hexamer, respectively; Vo represents an oxygen vacancy).

CHAPTER 6: CO_2 PHOTOREDUCTION ON SUPPORTED PT SUBNANOMETER CLUSTERS: EFFECT OF EXTRA ELECTRONS

In this chapter we will explore the effect of extra electrons on CO_2 adsorption sites of supported Pt tetramer, hexamer, and octamer sites obtained previously. Adding electrons to the model surfaces is to simulate photoexcited electrons and to study how it affects the CO2 anion formation, the first and key step in CO2 photoreduction. In previous study, we found significant charge transfer to the adsorbed CO_2 on neutral TiO2 surface. On the charged surfaces, the subnanometer Pt clusters help transfer the electron to CO2. This indicates the potential of the subnanometer Pt or other metal clusters to not only offer adsorption sites for bent form CO_2 but also to facilitate CO_2 reduction. The energetics and electron induced cluster reconstruction on charged surfaces are also reported in this chapter.

6.1 Introduction

Theoretical studies can help in the efficient design of promising catalyst.[168] Recently, we explored CO_2 photoreduction on subnanometer Ag and Pt clusters supported on TiO_2 surfaces using first-principles calculations.[58, 113] The root cause of cluster induced sub-bandgaps[73, 74] was investigated. The tendency for cluster sintering was also evaluated.

The incorporation of CO_2 molecule to the supported Pt clusters surfaces was then investigated to shed lights on the first and key step (CO_2 to CO_2^- anion[7, 122]) of CO_2 photoreduction mechanism.[113] Prior ab initio studies showed that bent form CO_2 barely adsorbed on stoichiometry surfaces of cluster and periodic TiO_2 models, [124, 126, 127, 152] while some

adsorption sites were identified on the surface with an oxygen vacancies.[122, 153] Similar trends were reported on other oxide surfaces such as ceria(110).[140] Surprisingly, we found that Pt octamers deposited on anatase TiO_2 benefit adsorption sites for bent form CO_2 in highly bent form thus enhancing such tiny cluster's capability to dissociate CO_2.[113] Besides, we also found a morphology effect (two dimensional (2D) and three dimensional (3D) geometries) of the Pt clusters on CO_2 adsorption, which was used to explain the structural fluxionality characteristics of the cluster.

In this article, we extend our previous studies to simulate photoexcited electrons on the supported Pt clusters, which we consider the effect of "light", the energy source enabling the photoreaction. Photoexcited electron has been simulated by introducing extra electrons to the systems with the compensating neutralizing positive background charges, [122, 124, 151] and by attaching a hydrogen atom allowing the population of the electron from hydrogen atom to the conduction band.[169] He et al.[122] studied the enegetics of adsorbed CO_2 on anatase TiO_2(101) surfaces upon the addition of one electron, and similar study has investigated on Brookite TiO_2 surfaces.[124] The mechanism steps leading to HCOOH and CO was studied on bulk TiO_2 surface and the TiO_2 nanocluster upon the addition of electrons;[151] on the other hand, such steps were also studied by attaching a hydrogen atom to the surface 2-fold bridging O atom to approximate photoexcited electrons.

Objectives of this study are to (i) find out whether or not the subnanometer Pt clusters help the transfer of the negative charge to the adsorbed CO_2 to increase the reduction chance (ii) investigate energetics and structural parameters of the adsorbed CO_2, (iii) see if there is any morphology effect upon the electron addition, and (vi) study the effect of extra electron on the CO_2 dissociation to CO. Together with our previous work regarding neutral supported Pt clusters

surfaces and the morphology effect,[113] this study will advance the design of potential subnanometer metal cluster/semiconductor photocatalysts for CO_2 photoreduction.

To study the success of the first and key step of CO_2 photoreduction on Pt clusters/TiO_2, extra electrons of 1, 2, and 3 are added to the obtained CO_2 adsorption configuration on perfect and reduced TiO_2 supported Pt tetramers, hexamers, and octamers.[113] We assess four basic ingredients[113] leading to the success of the first and key step, the availability of CO_2 binding sites, and their energetics and structural information. Reported in Figure 6.1 is a brief overview of such configurations. B2 and BVo1 (Figure 6.1a&b) are the adsorption sites without cluster's presence. PT2 (Figure 6.1c) is the site not associated with the cluster. PT1, PTVo1, PHVo1, PH2, PO2, and POVo1 (Figure 6.1d-i) are Pt related sites. Specifically, PTVo1 and POVo1 are interface edge sites where one O of CO_2 is interacting with the surface 5c-Ti atom while C or the other O with Pt clusters. PT1, PHVo1, PH2, and PO2 are Pt only site, among which PT1, PHVo1, and PH2 are 1-Pt only sites, and PO2 is 2-Pt only site. 1-Pt only and 2-Pt only sites mean CO_2 interacts with only one Pt and two Pt atoms of the clusters, respectively.[113]

6.2 Computational Methods

The model surfaces are from our previous studies of Pt tetramer, hexamer, and octamer supported on perfect and reduced anatase TiO_2 (101) surfaces.[58] The DFT calculations were performed using the VASP (Vienna Ab Initio Simulation package) code.[87-89] Exchange-correlation was represented by the Perdew–Burke–Ernzerhof (PBE) functional of the generalized gradient approximation (GGA),[90] and the electron-ion interactions were modeled by the projector-augmented wave (PAW)[91] method. The parameters used are the same as those in previous studies. To simulate the photoexcited electrons, we have added extra electrons to the model surfaces with the compensating neutralizing positive background charges, [122, 124, 151]

6.3 Results and Discussion

Reported in Figure 6.1 is a brief overview of such configurations. B2 and BVo1 (Figure 6.1a&b) are the adsorption sites without cluster's presence. PT2 (Figure 6.1c) is the site not associated with the cluster. PT1, PTVo1, PHVo1, PH2, PO2, and POVo1 (Figure 6.1d-i) are Pt related sites. Specifically, PTVo1 and POVo1 are interface edge sites where one O of CO_2 is interacting with the surface 5c-Ti atom while C or the other O with Pt clusters. PT1, PHVo1, PH2, and PO2 are Pt only site, among which PT1, PHVo1, and PH2 are 1-Pt only sites, and PO2 is 2-Pt only site. 1-Pt only and 2-Pt only sites mean CO_2 interacts with only one Pt and two Pt atoms of the clusters, respectively.[113]

6.3.1 Effect of Extra e^- on Adsorption Energy

Upon the addition of electrons (the light irradiation), we find that initial metastable adsorption sites become stable; for initial stable sites, which are mainly Pt clusters related sites (Pt only & interface edge sites), some CO_2 binds more stronger and some do oppositely. For Pt only sites the increase of adsorption energy positively correlates with the number of electrons added, whereas no such trend was found on interface edge sites. Note that on supported Pt tetramers, both Pt only and interface edge sites exhibit positive correlations between adsorption energy and the electron addition. This implies that smaller clusters are more sensitive to the added electrons positively in terms of CO_2 adsorption. In general, it is suggested the irradiation of light can strengthen the CO_2 binding or increase the binding sites on the TiO_2 surfaces without Pt clusters as well as the TiO_2 surfaces with cluster's presence.

For initial metastable sites, shown in Figure 6.2 are selected initial metastable CO_2 adsorption of sites without cluster's presence (B1, B2, and BVo5), not associated with cluster (PT2 and PT3), and Pt related (PH7 and PHVo3-PHVo5). As can be seen, when adding more

electrons, sites without cluster's presence become stable. For example, the CO_2 binding of BVo5 gradually increases as the incorporation of electrons from neutral to three. The same trend is also found on sites not associated with clusters. The more electron is added, the stronger the CO_2 binding in PT2 and PT3 sites. Pt related sites that are initially metastable also have similar trend; the adsorption energies of PHVo3 and PHVo5 have increased to fairly strong CO_2 binding, and the instability of CO_2 is decreased for PHVo4.

For initial stable sites, Pt related sites (interface edge and Pt only sites) behave differently upon the electron addition. Shown in Figure 6.3a are the selected interface edge sites. As can be seen, some sites show the correlation of CO_2 binding with electron addition, while some don't. For example, PTVo1 and PH3 show the positive correlation, while the extra electrons mitigate the CO_2 binding in PO1 and POVo1. However, Pt only sites exhibit positive correlations between the electron and CO_2 binding, as shown in Figure 6.3b. We would like to point out that interface edge and Pt only sites on supported Pt tetramer (PTVo1 & PT1) both show positive correlations, and this is not seen in larger size clusters, especially for Pt octamer. For Pt hexamer cases (PH1-PH4 and PHVo1 & PHVo2), interface edge and Pt only sites still have the same trends of the adsorption energy upon electron addition except PH1. As on the supported octamers, interface edge and Pt only sites start to behave differently. Also, PT1 shows the most increase in adsorption energy than any other sites. It is revealed that the smaller the cluster is, its respond to electron addition is more enhanced, which we will explain in the section followed.

6.3.2 Cluster Enhanced Charge Transfer

Even though the addition of electrons (the light irradiation) stabilizes the initial metastable CO_2 adsorption sites, the negative charge transfer to those adsorbed CO_2 is inhibited. Strangely, most sites that are not associated with clusters do not populate electron to the

adsorbed CO_2, but some do, which makes them resemble the electron population capability of Pt related sites. On the contrary, supported Pt clusters help the electron transfer to the adsorbed CO_2 upon electron addition to the model systems. This is a promising result, which leads to a conclusion that subnanometer Pt cluster not only provide adsorption site for bent form CO_2,[113] but also help electron transfer to such CO_2 to facilitate the formation of CO_2^- anion and CO_2 bond breaking.

For CO_2 adsorption associated with TiO_2, shown in Figure 6.4 a&b is the transfer of negative charge to C of CO_2 on the sites only in contact with TiO_2: B1, B2, and BVo1-BVo5 are the sites without the presence of the clusters, while PT2, PTVo2, PO4, and POVo5 are direct adsorption on the TiO_2 with the cluster's presence. It can be seen that the additional electrons do not transfer to the adsorbed CO_2 or for some cases additional electrons mitigate the negative charge originally possessed in the adsorbed CO_2. B2 and PT2 show trends of losing or gaining charges as the addition of the electrons, and BVo2 and BVo3 illustrate the charge decreasing trend. However, some adsorbed CO_2 do accumulate charge as the electron is added. As shown in Figure 6.4b, BVo1, BVo4, and PTVo2 (Vo representing the reduced surface) show some charge increment.

For CO_2 adsorption associated with Pt clusters, in general, the added electrons transfer to the adsorbed CO_2 in Pt related sites, but there are some differences between interface edge and Pt only sites. Shown in Figure 6.5a&b are the interface edge and Pt only sites from Pt tetramer, hexamer, and octamer deposited on stoichiometric and reduced anatase TiO_2(101) surfaces. Figure 6.5a shows that at some interface edge sites there is a limitation of the charge transfer to the adsorbed CO_2. PH3 and PH7 indicate that the charge transfer is saturated to those CO_2, while from PHVo3 and PHVo4 more electrons added reveal a decrease in the negative charge in the

CO_2. On the other hand, adsorbed CO_2 species in Pt only sites indicate fairly consistent trends of the charge increase on the adsorbed CO_2. This indicates the potential of Pt related sites to accumulate more electrons as more and more electrons are photo-excited, leading to the high success of the first and key step of CO_2 photoreduction and C-O bond breaking leading to valuable hydrocarbons such as CO, HCO_2H, CH_2CO, CH_3OH, and CH_4.

We would like to point out that the charge accumulation capability of CO_2 in BVo1, BVo4, and PTVo2 is similar to the Pt related sites just discussed. From our previous study, we have shown that the binding of CO_2 in the Pt related sites is facilitated by the hybridization of the bonding molecular orbitals of CO_2 with d orbitals of the Pt atoms.[113] We suggest that these boning orbitals formed by CO_2 and Pt clusters serve as channels for the charge transfer when the electron is added to the systems. The selected density plot of BVo1 from the dominating bonding states (Figure 6.4c) shows the formation of the bonding orbital form by C of CO_2 and surface Ti atom of the anatase TiO_2 (101) surface. It is concluded that as long as C of CO_2 is bonding with Ti, Pt, or any other metal clusters, it is possibly that CO_2 can be bound, leading to the formation of CO_2^- anion and further to light hydrocarbons.

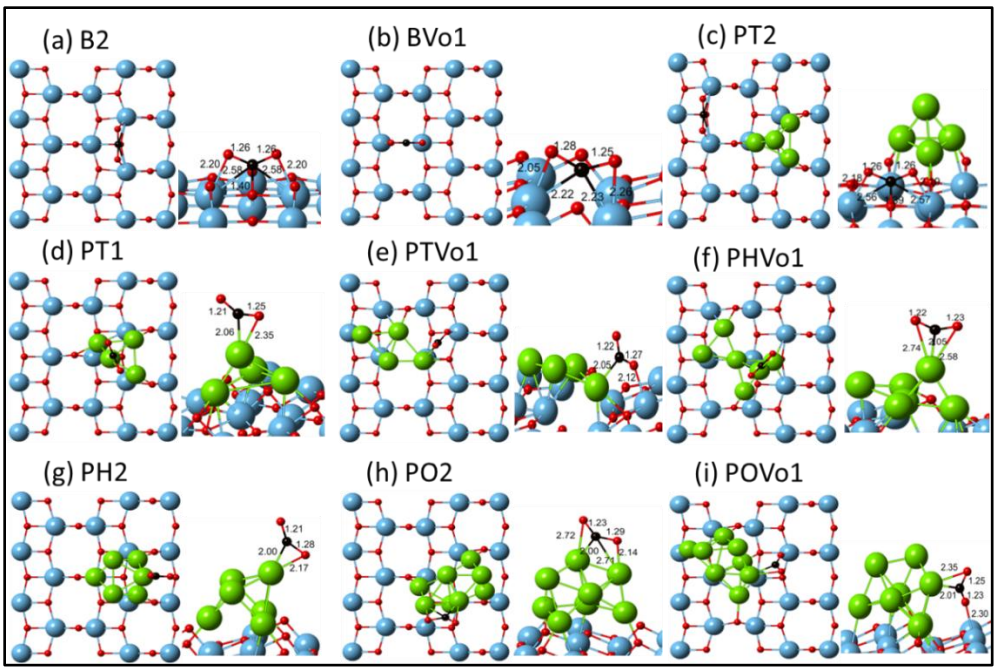

Figure 6.1 Selected CO_2 adsorption configurations on anatase TiO_2(101) surfaces w/wo Pt clusters (B representing TiO_2(101) surface without cluster; PH, PT, and PO representing Pt tetramer, Pt hexamer, and octamer, respectively; Vo represents an oxygen vacancy; O in red, C in black, Ti in blue, and Pt in green. The numbers indicate the bond lengths in Å).

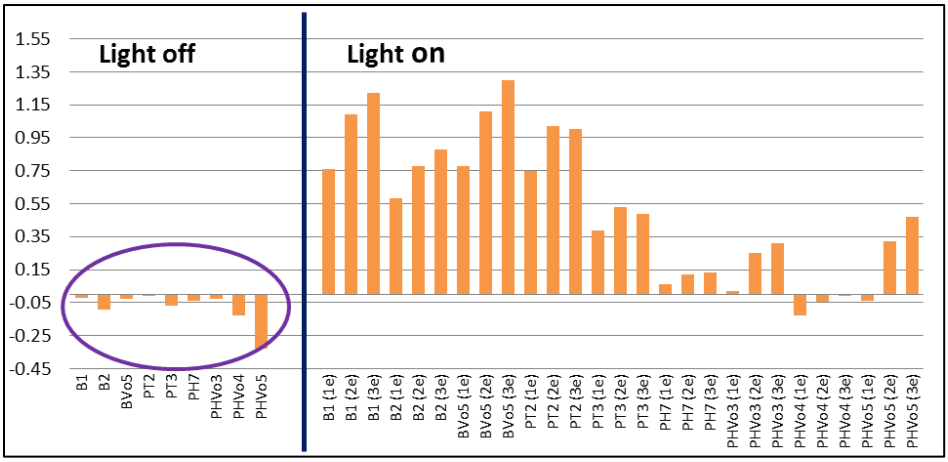

Figure 6.2 CO_2 adsorption configurations on anatase TiO_2(101) surfaces w/wo Pt clusters (B representing TiO_2(101) surface without cluster; PH, PT, and PO representing Pt tetramer, Pt hexamer, and octamer, respectively; Vo represents an oxygen vacancy; 1e-3e representing the addition of 1-3 electrons).

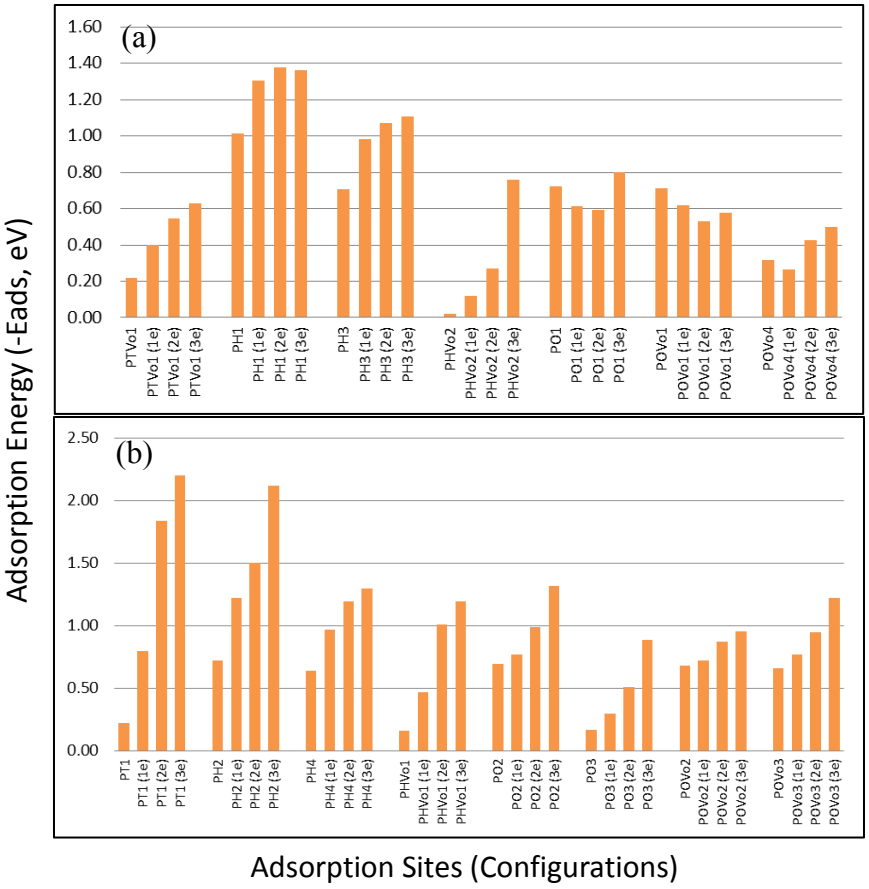

Figure 6.3 CO_2 adsorption configurations on anatase TiO_2(101) surfaces w/wo Pt clusters: (a) interface edge sites and (b) Pt only sites (B representing TiO_2(101) surface without cluster; PH, PT, and PO representing Pt tetramer, Pt hexamer, and octamer, respectively; Vo represents an oxygen vacancy; 1e-3e representing the addition of 1-3 electrons).

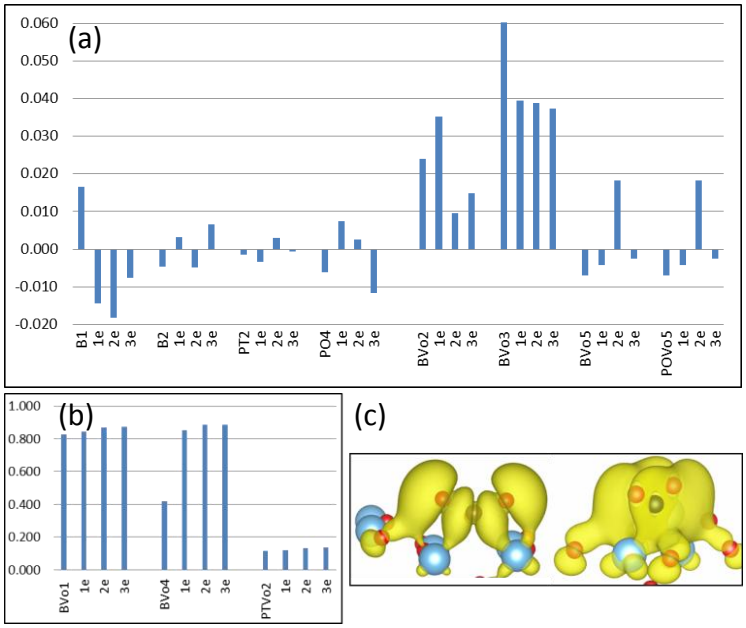

Figure 6.4 Negative charge accumulation at C of bound CO_2 of sites on anatase TiO_2(101) surfaces w/wo Pt clusters: (a) inhibited and (b) promoted charge transfer to C upon the addition of electrons. (c) Density plot of BVo1 (B representing TiO_2(101) surface without cluster; PH, PT, and PO representing Pt tetramer, Pt hexamer, and octamer, respectively; Vo represents an oxygen vacancy; 1e-3e representing the addition of 1-3 electrons).

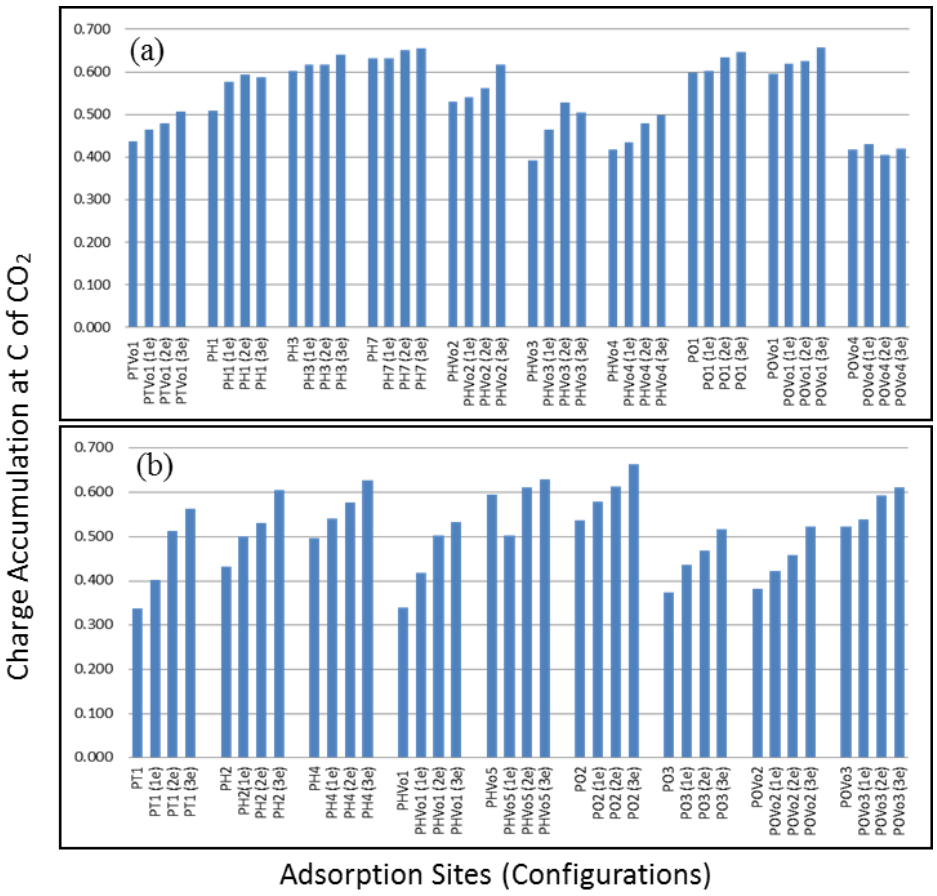

Figure 6.5 Negative charge accumulation at C of bound CO_2 of sites on anatase TiO_2(101) surfaces w/wo Pt clusters upon the addition of electrons: (a) Interface edge and (b) Pt only sites (B representing TiO_2(101) surface without cluster; PH, PT, and PO representing Pt tetramer, Pt hexamer, and octamer, respectively; Vo represents an oxygen vacancy; 1e-3e representing the addition of 1-3 electrons).

CHAPTER 7: PRELIMINARY EXPERIMENTAL STUDIES ON SUBNANOMETER PT CLUSTER SYNTHESIS AND CHARACTERIZATION

Compared to the conventional photocatalyst TiO_2, from DFT modeling the TiO_2 in the presence of Pt subnanometer clusters are found to offer adsorption sites for bent-form CO_2 species with CO_2^- anion-like nature, and these CO_2 bind rather strongly. Besides, the deposition of Pt clusters possibly induces sub-bandgaps, which enhances photocatalysis in terms of the maximum utilization of source light. In this chapter, an exploratory experimental work is performed to validate these computational results. It is shown from experimental results that subnanometer Pt clusters seems to be able to offer adsorption sites for CO_2, and there seems to be some bandgap reduction.

7.1 Introduction

Semiconductor based photocatalytic CO_2 reduction has become an important field, and the main products are useful light hydrocarbons such as CO, HCO_2H, CH_2O, CH_3OH, and CH_4. The success of this CO_2 reduction depends on the first and key step (reduction of CO_2 to CO_2^-), which relies on the geometry with which CO_2 is adsorbed on the TiO_2 surface: the more bent the geometry of the adsorbed CO_2 molecule, the easier the transfer of photoexcited electrons to CO_2 to form the CO_2^- anion.[122-124] From the computational study, Pt octamer and hexamer deposited on the TiO_2 are promising CO_2 reduction photocatalysts because they offer adsorption sites for bent-form CO_2 on the supported Pt octamer and hexamer surfaces either at the interface edge of the cluster and the TiO_2 or directly on the Pt clusters. On the other hand, doping[9-11] and defect

creation[72] have been demonstrated to reduce the bandgap, but it also increases the chances for the recombination of e-/h+ pairs[117]. Prior theoretical reports have shown sub-bandgap creation by depositing Pt_n(n=1-3),[73] Pt_n(n=1-8),[81] and Ag clusters(dimer, tetramer, and octamer)[58, 74, 75] on anatase and rutile TiO_2 surfaces. The recent theoretical result shows that the Pt cluster of 37 atoms is very likely to induce a continuous band within the bandgap of anatase TiO_2 (101), bringing a negative effect to photoactivity of TiO_2 due to the formation of recombination center of e-/h+ pairs.[109]

In this study, cluster sizes consisting of 8, 16, 24, 32, 40, and 55 atoms on anatase TiO_2 will be obtained via dendrimer-encapsulated synthesis. Temperature-programmed desorption and UV-Vis are used to validate the adsorption sites and cluster induced sub-bands reported by the DFT results.

7.2 Experimental Details

For synthesis, the dendrimer-encapsulated metal clusters[52, 170-172] was used to synthesize Pt subnanometer clusters. The synthesis procedure follows Castillo et al. work,[52, 57] which starts with the complexation of the Pt ion with the PAMAM dendrimer (G4-OH) for 24 hours. The molar ratio of the metal ion/dendrimer of 6, 10, 21, and 55 are used to synthesize subnanometer clusters and nanoparticle. Fourth-generation dendrimer (G4OH) with 10 wt% in methanol solution from Dendritech Inc. (Midland, MI) is used with a dendrimer stock solution of 250μM. K_2PtCl_4 (>99%) is used as received, and the metal precursor of 0.01M is prepared. 20 molar fold, compared to metal precursor, of freshly prepared $NaBH_4$(1M) is then used as reduction agent leading to encapsulated Pt clusters. The deposition of the clusters on the surface of anatase TiO_2 follows a previous study that the slurry containing the dendrimer-encapsulated metal clusters and

anatase TiO_2 is stirred until the color of the slurry turn to light gray.[173] The decomposition of the dendrimer is via thermal treatment; mixture of He and O_2 at 200°C.

For characterization, the TEM picture in Figure 6.1 shows that the sizes of the Pt clusters around 3nm that validates the synthesis procedure with the target 55 molar ratio of the metal ion/dendrimer. The Pt particles can be seen clearly deposited on the anatase TiO_2 surface, and this confirms the deposition procedure. CO_2 temperature-programmed desorption (CO_2-TPD) studies were performed to investigate the availability of the CO_2 adsorption sites and the CO_2 binding strength on the anatase TiO_2 supported Pt clusters. A Cirrus MKS mass spectrometer (MS) is connected with the reactor inside a Thermoscientific Thermolyne tube furnace, and 50 mg of the catalyst is used. The catalyst is first reduced under a gas mixture of 5% H_2 and He at a temperature of 200°C for 1 hour, and then is cooled to a temperature of 50°C under He only environment. 10% CO_2 in He was introduced for 30 min for the CO_2 adsorption on the catalysts, and the CO_2 desorption was carried out at a ramp rate of 10°C/min to 800°C which is held for 10 min. when reached. UV/Vis diffuse reflectance is used to estimate the optical band gaps of the catalysts, which is the estimation of sub-bandgaps formation. The catalyst powders were sandwiched between two quartz plates, and the spectra were using JASCO V-670.

7.3 Results and Discussions

CO_2 - TPD results of Pt clusters (6, 10, and 21 atoms) and clean anatase TiO_2 are shown in Figure 6.2. No apparent peaks of clean anatase TiO_2 reveal CO_2 adsorption is not likely to happen on the clean anatase TiO_2. Surprisingly, supported Pt clusters (6, 10, and 21 atoms) reveal their availability of CO_2 adsorption sites. There are two major peaks locating at around 300-400°C and 600-700°C, and a peak occurs at 100-150°C for supported 21 atom Pt cluster case. The peak positions for the three catalysts are almost the same in the 300-400°C, and this

means that there is no cluster size effect on the binding site in this range. However, peak positions at 600-700°C show some variation, which means that size is one factor for the binding site in this range. It appears, at 600-700°C, the larger the Pt clusters is, the smaller amount the CO_2 adsorption. However, we would like to point out that the peaks at 300-400°C and 600-700°C could also indicate the CO_2 from the dendrimer decomposition. A proper dendrimer removal step is needed to eliminate this factor. Since our adopted dendrimer removal step is below 200°C, the peak occurring at 100-150°C for supported 21 atom Pt cluster may reveal the availability of CO_2 adsorption sites on these tiny clusters.

As shown in Figure 6.3, the optical absorption of the sample catalysts are represented by Kubelka−Munk spectrum calculated with reflectance data using Kubelka−Munk equation.[174] It is revealed that the bandgap of anatase TiO_2 is estimated to be around 3.23eV, which is consistent with literature results.[5, 175] There seems to be a bandgap reduction toward visible range as the size of the Pt clusters decrease, possibly resulting from induced states within the bandgap by the deposition of subnanometer Pt clusters.

7.4 Conclusions

The subnanometer Pt cluster of the size in 6, 10, and 21 atoms are synthesized using dendrimer-encapsulated techniques, and deposited on the anatase TiO_2 to validate the DFT results. From TPD results, it seems that supported subnanometer Pt clusters can offer adsorption sites for CO2, but a strong dendrimer removal step is needed to further clarify the results. DFT results show possible sub-bandgaps formation by the application of subnanometer Pt cluster on the anatase TiO_2, which agrees with the trends shown in the experimental results. From the computational and experimental methods, it is indicated that the application of subnanometer

metal cluster can be an feasible method for the design of potential photocatalysts for CO_2 reduction.

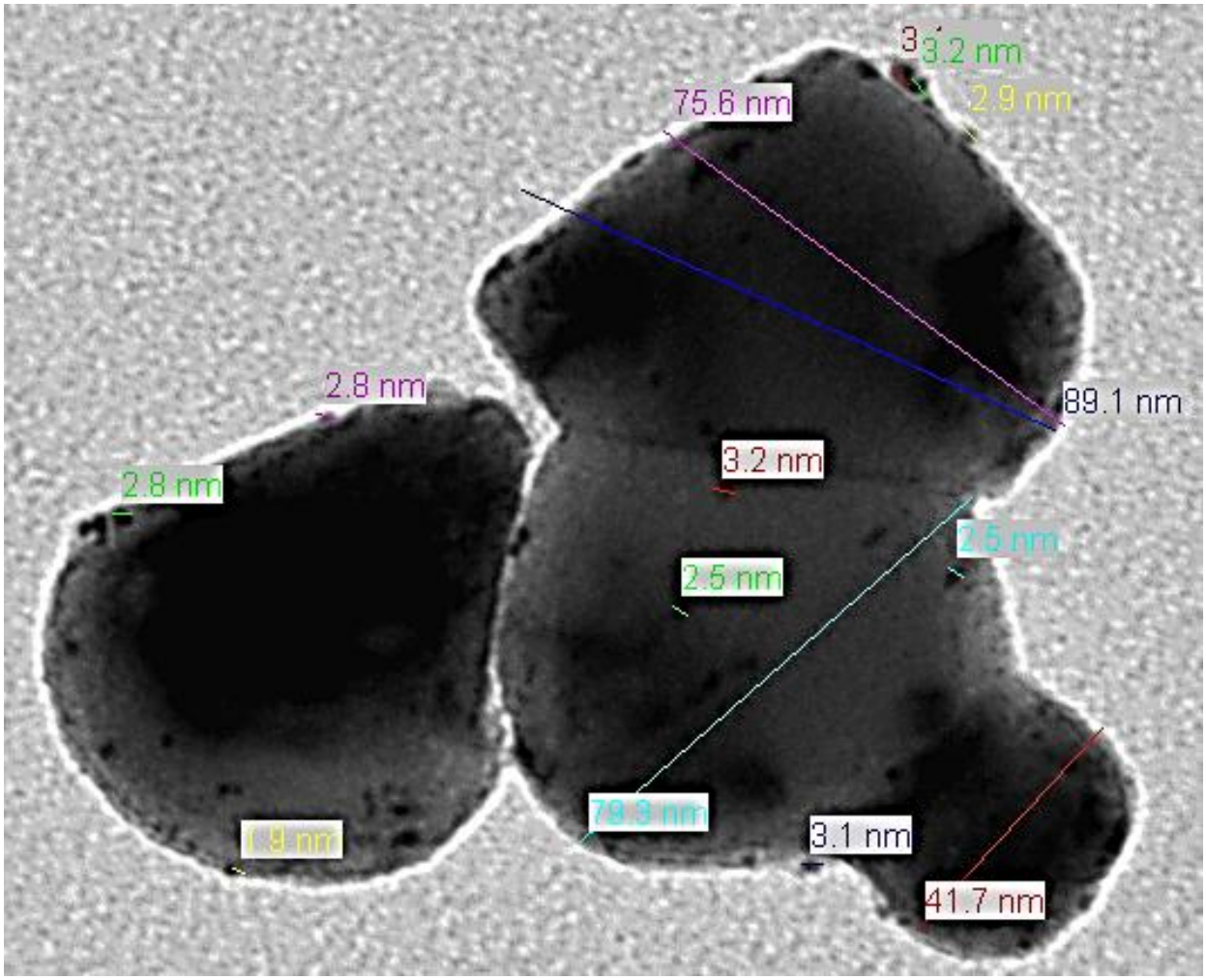

Figure 7.1 TEM photo of the Pt particles (55 molar ratio of the metal ion/dendrimer) on the anatase TiO_2 surface (TEM by Kassie Ngo, USF).

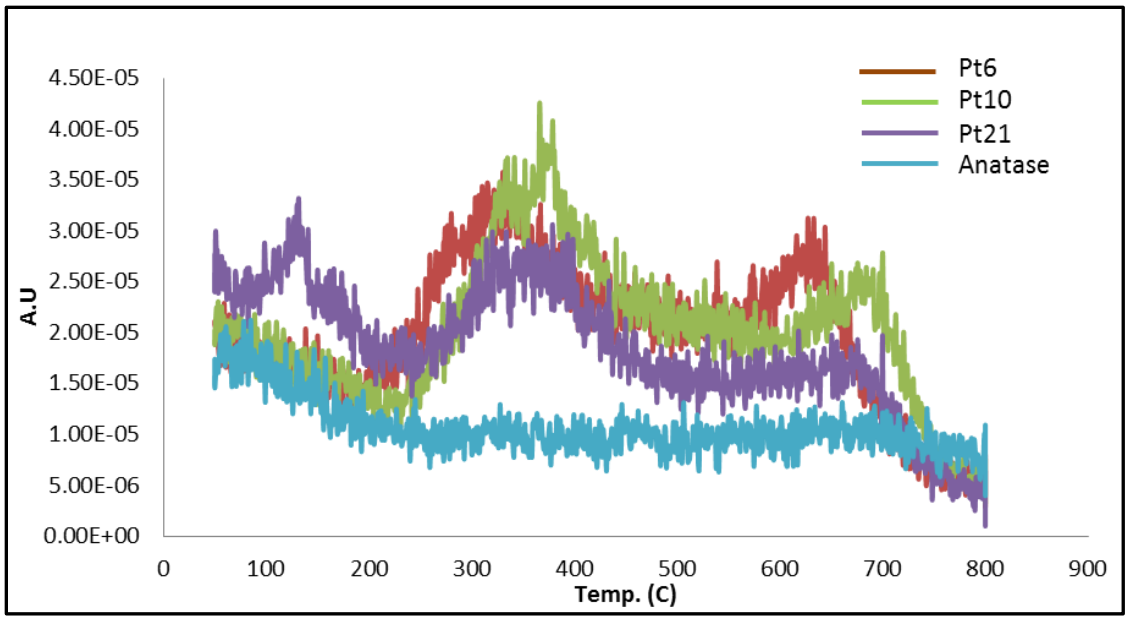

Figure 7.2 CO_2-TPD of anatase TiO_2 and supported n (n=6,10,and 21) atom Pt clusters (TPD by Ummuhan Cimenler, USF).

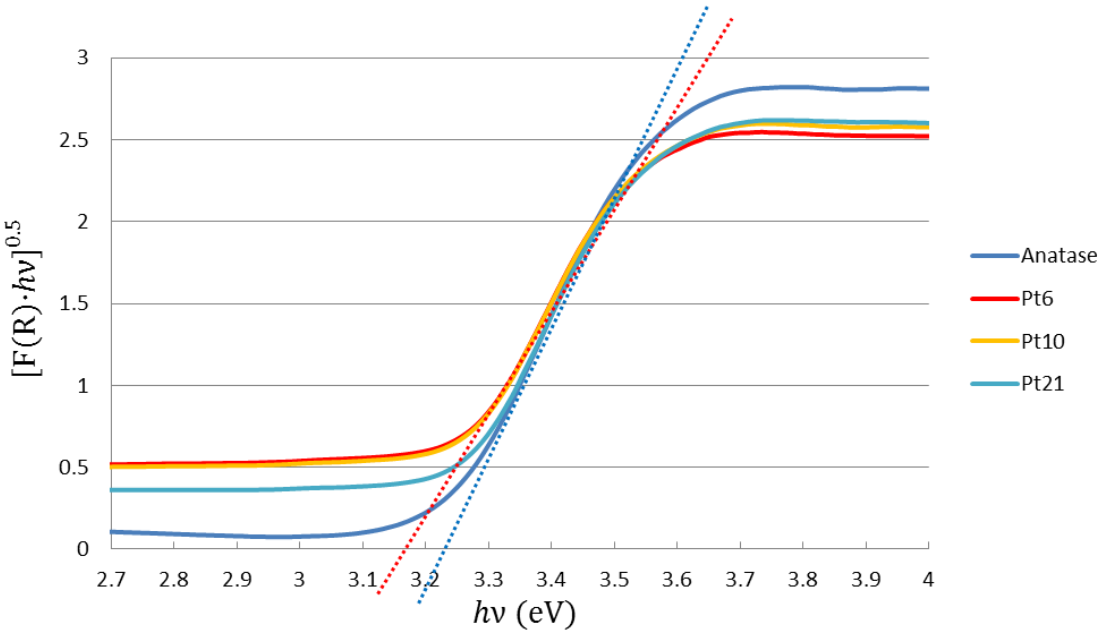

Figure 7.3 Kubelka−Munk function vs the energy of anatase TiO_2 and supported n (n=6,10,and 21) atom Pt clusters.

CHAPTER 8: CONCLUSIONS AND FUTURE WORK

8.1 Conclusions

In this research, the reduction of CO_2 on subnanometer Ag/Pt clusters (dimer, tetramer, hexamer, and octamer) supported on anatase TiO_2 are explored using Density Functional Theory calculations to shed light on the design of subnanometer metal clusters based photocatalysts.

In the study of interplays between the subnanometer cluster and TiO_2 support (catalysis part), the goal was to investigate binding mechanism to assist subnanometer clusters characterization and to gain insights into issues related to catalysis. It was found that when clusters are deposited on the anatase TiO_2 (101) surface, the nucleation centers for Ag clusters are surface O atoms, while for Pt clusters the centers are surface Ti sites. A possible driving force for encapsulation is metal cluster's strong tendency to binding with specific surface atoms of the support. An NEB study resulting in the preliminary encapsulation state considers rotation and diffusion of the Pt cluster on the support, and suggests the rotation takes the most energy to initiate cluster encapsulation. The adsorption energy and the number of stable cluster adsorption sites are indicators for the tendency of the cluster sintering tendency. The stronger adsorption energy and more stable adsorption sites mean that clusters bind strongly with support and that there are more trapping sites for the clusters. Compared to Ag clusters, Pt clusters are less likely to sinter on the anatase TiO_2 (101) surface.

In the investigation of CO_2 adsorption on TiO_2 in the presence of Ag/Pt clusters (CO_2 photoreduction study), the focus was on the first and key step of the CO_2 photoreduction. The

effect of the presence of subnanometer clusters were first studied using Ag/Pt octamers; Pt tetramer, hexamer, and octamer were then used to explore the cluster geometry effect. It was found that the presence of Ag or Pt octamers can substantially modify CO_2 adsorption even at TiO_2 surface sites where there is no direct CO_2 binding between with the octamer. The underlying factors are electron density donation from the clusters to the surfaces and the Ti-O (CO_2) attraction and Ti-C (CO_2) repulsion.

Interestingly, as opposed to supported Ag octamer and clean TiO_2, supported Pt octamer provides certain advantages for CO_2 photoreduction. The extra adsorption sites for bent-form CO_2, a key dissociation precursor for CO_2 activation, are obtained at interface edge and directly on the Pt octamer; furthermore, CO_2 binds rather strongly on these sites. Bader charge analysis suggests that these Pt related CO_2 binding sites are CO_2^- anion-type complex as negative charge accumulates at the C atom of the CO_2 molecule. A detailed examination of the associated electronic structure suggests that unlike binding to TiO_2 sites, where electrostatics play a key role, the interaction between CO_2 and Pt is instead facilitated by the formation of bonding orbitals consist of molecular orbitals of CO_2 forming and d states of Pt in the clusters. Further analysis shows the main bonding states for Pt-CO_2 come from CO_2 s&p - metal d state in the range -10 and -5 eV (compared to Fermi level). Besides, the interface sites bind stronger than Pt-only sites which may be extra bonding interaction with the surface oxygen atom.

Two geometry factors were found for the key precursor adsorption: structural fluxionality and binding competition. Structural fluxionality is measured by defining it as displacement (per atom of the clusters), and it was found that especially at interface edge site 3D Pt clusters have higher structural fluxionality than pro-2D Pt clusters. High fluxionality capability means more chances to reach maximum orbital overlaps of Pt clusters and CO_2, resulting in stronger CO_2

binding. Binding competition occurs when there is a tug of war between more than one Pt- CO_2 interactions, leading to failure to meet maximum orbital overlaps of Pt clusters and CO_2. The failure for CO_2 to adsorb on the 2D surface can be understood by the limited structural fluxionality and binding competition: full orbital overlaps of more than Pt- CO_2 interactions are restricted by the rigid 2D Pt resulting from the strong Pt and surface Ti interactions. Pt tetramer and hexamer exhibit different structures on perfect and reduced surfaces. The pro-2D (on reduced surface) rather than 3D structures can be explained by more interactions of the Pt clusters with the surface Ti atom of the support.

The negative charge accumulation, O-C-O angle, and adsorption sites of the adsorbed CO_2 on supported Pt clusters (octamer, hexamer, and tetramer) can be revealed by vibrational frequencies. ν2 mode is an reliable indicator of negative charge accumulation on C while ν3 mode an indicator for identifying bent CO_2 geometries, which together revealing the formations of CO_2^- anion precursor leading to the success of CO_2 photoreduction. ν1, ν2, and ν3 modes can be used to identify CO_2 adsorption sites. Firstly, the Pt cluster associated sites and direct TiO_2 surface site can be unveiled by ν1 and ν2 modes. Specifically, interface edge sites are correlated with ν2 in higher range (~760-775 cm^{-1}) and ν3 in lower range (1480-1540 cm^{-1}). 1-Pt only sites are correlated with ν2 in lower range (~570-625cm^{-1}) and ν3 in higher range (~1910-2000 cm^{-1}). A mixed interface edge/2-Pt only sites are in between the higher and lower ranges of ν2 and ν3.

One possible mechanism of CO_2 dissociation to CO on the Pt octamer/reduced anatase TiO_2 (101) surface, with an energy barrier of 1.01eV, may open alternative pathways for CO_2 photoreduction, resulting from the structural fluxionality of the Pt octamer and the filling of antibonding orbitals of CO_2 to weaken the intramolecular C-O bond. We also find that the bond breaking tendency is related to charge accumulation at C and O-C-O angle of adsorbed CO_2

species, which can be correlated with vibrational frequencies ν2 and ν3. Moreover, the utilization of a larger fraction of photons in the solar spectrum in subnanometer based photocatalysts can be achieved by the cluster induced sub-bandgaps. We found that d-band center of the cluster can be an indicator for such induced sub-bandgaps. When the absolute value of the d-band center is closer and smaller than the value the bandgap of some semiconductors, it is very likely the sub-bandgaps will exist. Pt clusters can help populate photoexcited electrons to the adsorbed CO_2 to facilitate the CO_2 reduction, as evidenced by results obtained with extra electrons added to the system.

Finally, the experimental results seem to validate the computational results, but further clarification is needed to make conclusive findings. The variation of the surface electronic structure is one factor determining the chemical and physical properties of the catalyst, and we have shown the capability of subnanometer metal clusters to modify the surface electronic structure. Our results will be useful in the design of promising subnanometer metal clusters based catalysts and photocatalyts.

8.2 Future Work

This research investigated the preferred CO_2 adsorption in the first and key step of CO_2 photoreduction. Aspects of studies are 1. The effect of the presence of the subnanometer metal clusters on TiO_2 as compared to the pure TiO_2 surfaces. 2. The cluster effect on the preferred CO_2 adsorption. An ongoing work is the addition of electrons to simulate photoexcited electrons, expecting to see supported Pt cluster help the population of photoexcited electron to the adsorbate as compared to clean TiO_2 surface.

Further steps to the production of light hydrocarbons such as HCOOH and CO has been studied on TiO_2 and TiO_2 cluster;[151] and the reaction barriers were compared. The same steps

studies can be investigated on the supported subnanometer metal clusters. This research has shown that the application of the subnanometer metal clusters can modify the electronic structure of the convention semiconductors. Also, the mechanism of the cluster induced CO_2 dissociation to CO due to structural fluxionality is different from larger size nanoparticle. The reaction barrier leading to HCOOH and CO is an area worth exploring on the supported Pt subnanometer clusters. Pioneering study of further steps of CO_2 photoreduction to HCHO, CH_3OH, and CH4 can also be investigated and compared.

MOF (Metal Organic Frameworks) are promising nanoporous materials[113, 176] which are crystalline 3D inorganic–organic hybrids constructed from metal clusters (secondary building units)[177] and organic linkers via coordination bonds.[58, 178] Two main aspects can be investigated: 1. screening of potential secondary building units and linker candidates for proper bandgap and band edges for CO_2 reduction reaction. 2. The mechanism study of the first and key step and others steps leading to the light hydrocarbon. Bandgap and band edges are crucial to photocatalysis. Suitable bandgap allows the utilization of specific light sources, whereas proper band edges allow the transfer of the photo-excited electron-hole pairs to facilitate redox reactions. The mechanism can also gain insights into the development of potential photocatalysts. The applications of the subnanometer metal cluster on MOF materials can also be studied. Different combinations of secondary building units, organic ligands, and metal clusters may lead to interesting electronic structure, which can open another exciting field photocatalytic CO_2 reduction.

REFERENCES

1. P. Usubharatana, D. McMartin, A. Veawab and P. Tontiwachwuthikul, *Industrial & Engineering Chemistry Research*, 2006, 45, 2558-2568.
2. S. C. Roy, O. K. Varghese, M. Paulose and C. A. Grimes, *ACS Nano*, 2010, 4, 1259-1278.
3. S. N. Habisreutinger, L. Schmidt-Mende and J. K. Stolarczyk, *Angew Chem Int Edit*, 2013, 52, 7372-7408.
4. Ipcc, 2007: Climate Change 2007: The Physical Science Basis. Contribution of Working Group I to the Fourth Assessment Report of the Intergovernmental Panel on Climate Change [Solomon, S., D. Qin, M. Manning, Z. Chen, M. Marquis, K.B. Averyt, M.Tignor and H.L. Miller (Eds.)]. Cambridge University Press, Cambridge, United Kingdom and New York, Ny, USA. 2007.
5. A. L. Linsebigler, G. Lu and J. T. Yates, *Chem Rev*, 1995, 95, 735-758.
6. K. Koci, L. Obalova and Z. Lacny, *Chemical Papers*, 2008, 62.
7. V. P. Indrakanti, J. D. Kubicki and H. H. Schobert, *Energ Environ Sci*, 2009, 2.
8. T. Yui, Y. Tamaki, K. Sekizawa, O. Ishitani and C. A. Bignozzi, Springer Berlin / Heidelberg, 2011, vol. 303, pp. 151-184.
9. O. K. Varghese, M. Paulose, T. J. LaTempa and C. A. Grimes, *Nano Lett*, 2009, 9, 731-737.
10. J. Wang, D. N. Tafen, J. P. Lewis, Z. Hong, A. Manivannan, M. Zhi, M. Li and N. Wu, *Journal of the American Chemical Society*, 2009, 131, 12290-12297.
11. K. Kočí, K. Matějů, L. Obalová, S. Krejčíková, Z. Lacný, D. Plachá, L. Čapek, A. Hospodková and O. Šolcová, *Applied Catalysis B: Environmental*, 2010, 96, 239-244.
12. K. Awazu, M. Fujimaki, C. Rockstuhl, J. Tominaga, H. Murakami, Y. Ohki, N. Yoshida and T. Watanabe, *Journal of the American Chemical Society*, 2008, 130, 1676-1680.
13. D. B. Ingram and S. Linic, *J Am Chem Soc*, 2011, 133, 5202-5205.
14. N. Sasirekha, S. J. S. Basha and K. Shanthi, *Appl Catal B-Environ*, 2006, 62, 169-180.
15. P. Christopher, D. B. Ingram and S. Linic, *J Phys Chem C*, 2010, 114, 9173-9177.
16. W. B. Hou, Z. W. Liu, P. Pavaskar, W. H. Hung and S. B. Cronin, *Journal of Catalysis*, 2011, 277, 149-153.
17. P. Christopher, H. L. Xin and S. Linic, *Nat Chem*, 2011, 3, 467-472.
18. Q.-H. Zhang, W.-D. Han, Y.-J. Hong and J.-G. Yu, *Catalysis Today*, 2009, 148, 335-340.
19. I. M. Arabatzis, T. Stergiopoulos, D. Andreeva, S. Kitova, S. G. Neophytides and P. Falaras, *Journal of Catalysis*, 2003, 220, 127-135.
20. W. Hou, Z. Liu, P. Pavaskar, W. H. Hung and S. B. Cronin, *Journal of Catalysis*, 2011, 277, 149-153.
21. Y. Lei, F. Mehmood, S. Lee, J. Greeley, B. Lee, S. Seifert, R. E. Winans, J. W. Elam, R. J. Meyer, P. C. Redfern, D. Teschner, R. Schlogl, M. J. Pellin, L. A. Curtiss and S. Vajda, *Science*, 2010, 328, 224-228.
22. I. X. Green, W. Tang, M. Neurock and J. T. Yates, *Science*, 2011, 333, 736-739.

23. B. Yoon, H. Häkkinen, U. Landman, A. S. Wörz, J.-M. Antonietti, S. Abbet, K. Judai and U. Heiz, *Science*, 2005, 307, 403-407.
24. H. Häkkinen, S. Abbet, A. Sanchez, U. Heiz and U. Landman, *Angewandte Chemie International Edition*, 2003, 42, 1297-1300.
25. B. T. Qiao, A. Q. Wang, X. F. Yang, L. F. Allard, Z. Jiang, Y. T. Cui, J. Y. Liu, J. Li and T. Zhang, *Nat Chem*, 2011, 3, 634-641.
26. S. Vajda, M. J. Pellin, J. P. Greeley, C. L. Marshall, L. A. Curtiss, G. A. Ballentine, J. W. Elam, S. Catillon-Mucherie, P. C. Redfern, F. Mehmood and P. Zapol, *Nat Mater*, 2009, 8, 213-216.
27. C. Mohr, H. Hofmeister, J. Radnik and P. Claus, *J Am Chem Soc*, 2003, 125, 1905-1911.
28. S. J. TAUSTER, *Accounts Chem Res*, 1987, 20.
29. G. A. Ferguson, F. Mehmood, R. B. Rankin, J. P. Greeley, S. Vajda and L. A. Curtiss, *Top Catal*, 2012, 55, 353-365.
30. Y. Wang and J. P. Perdew, *Phys Rev B*, 1991, 44, 13298-13307.
31. K. Burke, M. Ernzerhof and J. P. Perdew, *Chem Phys Lett*, 1997, 265, 115-120.
32. J. C. Phillips, *Phys Rev*, 1958, 112, 685-695.
33. V. Heine, *Solid State Physics*, 1970, 24, 1-36.
34. D. Vanderbilt, *Phys Rev B*, 1990, 41, 7892-7895.
35. P. E. Blochl, *Phys Rev B*, 1994, 50, 17953-17979.
36. M. Aizawa, S. Lee and S. L. Anderson, *J Chem Phys*, 2002, 117, 5001-5011.
37. L. Benz, X. Tong, P. Kemper, Y. Lilach, A. Kolmakov, H. Metiu, M. T. Bowers and S. K. Buratto, *J Chem Phys*, 2005, 122.
38. S. S. Lee, C. Y. Fan, T. P. Wu and S. L. Anderson, *Journal of the American Chemical Society*, 2004, 126, 5682-5683.
39. H. Bonnemann and R. M. Richards, *European Journal of Inorganic Chemistry*, 2001, 2455-2480.
40. H. Zhang, J. Okuni and N. Toshima, *One-pot synthesis of Ag-Au bimetallic nanoparticles with Au shell and their high catalytic activity for aerobic glucose oxidation*, 2011.
41. Y. L. Liu and A. R. H. Walker, *Angewandte Chemie-International Edition*, 2010, 49, 6781-6785.
42. B. Rodriguez-Gonzalez, A. Burrows, M. Watanabe, C. J. Kiely and L. M. Liz-Marzan, *Journal of Materials Chemistry*, 2005, 15, 1755-1759.
43. D. Ferrer, A. Torres-Castro, X. Gao, S. Sepulveda-Guzman, U. Ortiz-Mendez and M. Jose-Yacaman, *Nano Letters*, 2007, 7, 1701-1705.
44. M. Zhou, S. H. Chen, S. Y. Zhao and H. Y. Ma, *Physica E-Low-Dimensional Systems & Nanostructures*, 2006, 33, 28-34.
45. J. B. Raoof, R. Ojani and S. Rashid-Nadimi, *Journal of Electroanalytical Chemistry*, 2010, 641, 71-77.
46. S. Remita, M. Mostafavi and M. O. Delcourt, *Radiation Physics and Chemistry*, 1996, 47, 275-279.
47. T. A. Yamamoto, T. Nakagawa, S. Seino and H. Nitani, *Applied Catalysis a-General*, 2010, 387, 195-202.
48. Y. Mizukoshi, K. Okitsu, Y. Maeda, T. A. Yamamoto, R. Oshima and Y. Nagata, *Journal of Physical Chemistry B*, 1997, 101, 7033-7037.
49. S. Anandan, F. Grieser and M. Ashokkumar, *Journal of Physical Chemistry C*, 2008, 112, 15102-15105.

50. M. Sakamoto, M. Fujistuka and T. Majima, *Journal of Photochemistry and Photobiology C-Photochemistry Reviews*, 2009, 10, 33-56.
51. C. M. Gonzalez, Y. Liu and J. C. Scaiano, *Journal of Physical Chemistry C*, 2009, 113, 11861-11867.
52. W. Huang, J. N. Kuhn, C. K. Tsung, Y. Zhang, S. E. Habas, P. Yang and G. A. Somorjai, *Nano Lett*, 2008, 8, 2027-2034.
53. Y. H. Niu and R. M. Crooks, *Cr Chim*, 2003, 6, 1049-1059.
54. D. Yamamoto, S. Watanabe and M. T. Miyahara, *Langmuir*, 2010, 26, 2339-2345.
55. T. Kibata, T. Mitsudome, T. Mizugaki, K. Jitsukawaa and K. Kaneda, *Chem Commun*, 2013, 49, 167-169.
56. T. Imaoka, H. Kitazawa, W.-J. Chun, S. Omura, K. Albrecht and K. Yamamoto, *J Am Chem Soc*, 2013, 135, 13089-13095.
57. V. A. Castillo and J. N. Kuhn, *J Phys Chem C*, 2012, 116, 8627-8633.
58. C. T. Yang, N. Balakrishnan, V. R. Bhethanabotla and B. Joseph, *J Phys Chem C*, 2014, 118, 4702-4714.
59. U. Heiz, A. Sanchez, S. Abbet and W. D. Schneider, *J Am Chem Soc*, 1999, 121, 3214-3217.
60. Y. Zhang, X. Cui, F. Shi and Y. Deng, *Chemical Reviews*, 2011, 112, 2467-2505.
61. S. Bonanni, K. Aït-Mansour, W. Harbich and H. Brune, *J Am Chem Soc*, 2012, 134, 3445-3450.
62. Y. Watanabe, X. Wu, H. Hirata and N. Isomura, *Catalysis Science & Technology*, 2011, 1, 1490-1495.
63. S. Lee, C. Fan, T. Wu and S. L. Anderson, *The Journal of Chemical Physics*, 2005, 123, 124710-124713.
64. X. Tong, L. Benz, P. Kemper, H. Metiu, M. T. Bowers and S. K. Buratto, *J Am Chem Soc*, 2005, 127, 13516-13518.
65. L. Benz, X. Tong, P. Kemper, Y. Lilach, A. Kolmakov, H. Metiu, M. T. Bowers and S. K. Buratto, *The Journal of Chemical Physics*, 2005, 122, 081102-081104.
66. X. Tong, L. B. Benz, S. Chretien, Y. Lilach, P. R. Kemper, A. Kolmakov, H. Metiu, M. T. Bowers and S. K. Buratto, *Abstr Pap Am Chem S*, 2005, 229, U663-U663.
67. A. Uzun, V. Ortalan, Y. Hao, N. D. Browning and B. C. Gates, *Acs Nano*, 2009, 3, 3691-3695.
68. A. Sanchez, S. Abbet, U. Heiz, W. D. Schneider, H. Hakkinen, R. N. Barnett and U. Landman, *J Phys Chem A*, 1999, 103, 9573-9578.
69. W. E. Kaden, T. P. Wu, W. A. Kunkel and S. L. Anderson, *Science*, 2009, 326, 826-829.
70. A. Sclafani and J.-M. Herrmann, *Journal of Photochemistry and Photobiology A: Chemistry*, 1998, 113, 181-188.
71. S. Linic, P. Christopher and D. B. Ingram, *Nat Mater*, 2011, 10, 911-921.
72. W. Hou, W. H. Hung, P. Pavaskar, A. Goeppert, M. Aykol and S. B. Cronin, *ACS Catalysis*, 2011, 1, 929-936.
73. Y. Han, C.-j. Liu and Q. Ge, *The Journal of Physical Chemistry B*, 2006, 110, 7463-7472.
74. A. S. Mazheika, V. E. Matulis and O. A. Ivashkevich, *Journal of Molecular Structure: THEOCHEM*, 2010, 942, 47-54.
75. A. S. Mazheika, T. Bredow, V. E. Matulis and O. A. Ivashkevich, *The Journal of Physical Chemistry C*, 2011, 115, 17368-17377.
76. S. Chretien and H. Metiu, *The Journal of Chemical Physics*, 2007, 127, 149902-149901.

77. D.-e. Jiang, S. H. Overbury and S. Dai, *The Journal of Physical Chemistry C*, 2012, 116, 21880-21885.
78. Y. Zhou, C. L. Muhich, B. T. Neltner, A. W. Weimer and C. B. Musgrave, *J Phys Chem C*, 2012, 116, 12114-12123.
79. X. Q. Gong, A. Selloni, O. Dulub, P. Jacobson and U. Diebold, *Journal of the American Chemical Society*, 2008, 130, 370-381.
80. Y. Han, M. Zhang, W. Li and J. Zhang, *Phys Chem Chem Phys*, 2012, 14, 8683-8692.
81. D. Çakır and O. Gülseren, *The Journal of Physical Chemistry C*, 2012, 116, 5735-5746.
82. A. Selloni, *Nat Mater*, 2008, 7, 613-615.
83. N. A. Deskins, R. Rousseau and M. Dupuis, *J Phys Chem C*, 2010, 114, 5891-5897.
84. S. Chretien and H. Metiu, *The Journal of Chemical Physics*, 2007, 127, 244708-244713.
85. A. S. Mazheika, V. E. Matulis and O. A. Ivashkevich, *J Mol Struc-Theochem*, 2010, 942, 47-54.
86. P. Scheiber, M. Fidler, O. Dulub, M. Schmid, U. Diebold, W. Y. Hou, U. Aschauer and A. Selloni, *Phys Rev Lett*, 2012, 109.
87. G. Kresse and J. Furthmuller, *Comp. Mater. Sci.*, 1996, 6, 15-50.
88. G. Kresse and J. Furthmuller, *Phys. Rev. B: Condens. Matter Mater. Phys.*, 1996, 54, 11169-11186.
89. G. Kresse and J. Hafner, *Phys. Rev. B: Condens. Matter Mater. Phys.*, 1993, 47, 558-561.
90. J. P. Perdew, K. Burke and M. Ernzerhof, *Phys. Rev. Lett.*, 1996, 77, 3865-3868.
91. P. E. Blochl, *Phys. Rev. B: Condens. Matter Mater. Phys.*, 1994, 50, 17953-17979.
92. J. Yang, C. Q. Lv, Y. Guo and G. C. Wang, *J Chem Phys*, 2012, 136.
93. H. J. Monkhorst and J. D. Pack, *Phys. Rev. B: Condens. Matter Mater. Phys.*, 1976, 13, 5188-5192.
94. M. J. T. Frisch, G. W.; Schlegel, H. B.; Scuseria, G. E.; Robb, M. A.; Cheeseman, J. R.; Scalmani, G.; Barone, V.; Mennucci, B.; Petersson, G. A.; Nakatsuji, H.; Caricato, M.; Li, X.; Hratchian, H. P.; Izmaylov, A. F.; Bloino, J.; Zheng, G.; Sonnenberg, J. L.; Hada, M.; Ehara, M.; Toyota, K.; Fukuda, R.; Hasegawa, J.; Ishida, M.; Nakajima, T.; Honda, Y.; Kitao, O.; Nakai, H.; Vreven, T.; Montgomery, Jr., J. A.; Peralta, J. E.; Ogliaro, F.; Bearpark, M.; Heyd, J. J.; Brothers, E.; Kudin, K. N.; Staroverov, V. N.; Kobayashi, R.; Normand, J.; Raghavachari, K.; Rendell, A.; Burant, J. C.; Iyengar, S. S.; Tomasi, J.; Cossi, M.; Rega, N.; Millam, J. M.; Klene, M.; Knox, J. E.; Cross, J. B.; Bakken, V.; Adamo, C.; Jaramillo, J.; Gomperts, R.; Stratmann, R. E.; Yazyev, O.; Austin, A. J.; Cammi, R.; Pomelli, C.; Ochterski, J. W.; Martin, R. L.; Morokuma, K.; Zakrzewski, V. G.; Voth, G. A.; Salvador, P.; Dannenberg, J. J.; Dapprich, S.; Daniels, A. D.; Farkas, Ö.; Foresman, J. B.; Ortiz, J. V.; Cioslowski, J.; Fox, D. J., *Gaussian 09; Gaussian, Inc.,Wallingford CT*, 2009.
95. A. D. Becke, *J Chem Phys*, 1993, 98, 5648-5652.
96. C. T. Lee, W. T. Yang and R. G. Parr, *Phys Rev B*, 1988, 37, 785-789.
97. W. Tang, E. Sanville and G. Henkelman, *Journal of Physics-Condensed Matter*, 2009, 21.
98. D. Sheppard, R. Terrell and G. Henkelman, *J Chem Phys*, 2008, 128.
99. G. Henkelman and H. Jonsson, *J Chem Phys*, 2000, 113, 9978-9985.
100. G. Henkelman, B. P. Uberuaga and H. Jonsson, *J Chem Phys*, 2000, 113, 9901-9904.
101. V. Celik, H. Unal, E. Mete and S. Ellialtioglu, *Phys Rev B*, 2010, 82.
102. F. Pesty, H. P. Steinruck and T. E. Madey, *Surf Sci*, 1995, 339, 83-95.
103. O. Dulub, W. Hebenstreit and U. Diebold, *Phys Rev Lett*, 2000, 84, 3646-3649.

104. V. V. Pushkarev, Z. W. Zhu, K. J. An, A. Hervier and G. A. Somorjai, *Top Catal*, 2012, 55, 1257-1275.
105. S. Bernal, J. J. Calvino, M. A. Cauqui, J. M. Gatica, C. López Cartes, J. A. Pérez Omil and J. M. Pintado, *Catalysis Today*, 2003, 77, 385-406.
106. J. Zhang and A. N. Alexandrova, *J Chem Phys*, 2011, 135.
107. F. Rieboldt, L. B. Vilhelmsen, S. Koust, J. V. Lauritsen, S. Helveg, L. Lammich, F. Besenbacher, B. Hammer and S. Wendt, *J Chem Phys*, 2014, 141.
108. S. C. Ammal and A. Heyden, *J Chem Phys*, 2010, 133.
109. C. L. Muhich, Y. Zhou, A. M. Holder, A. W. Weimer and C. B. Musgrave, *J Phys Chem C*, 2012, 116, 10138-10149.
110. A. Nilsson, L. G. M. Pettersson, B. Hammer, T. Bligaard, C. H. Christensen and J. K. Norskov, *Catal Lett*, 2005, 100, 111-114.
111. M. Landmann, E. Rauls and W. G. Schmidt, *J Phys-Condens Mat*, 2012, 24.
112. N. Lopez and J. K. Norskov, *Surf Sci*, 2002, 515, 175-186.
113. C.-T. Yang, B. C. Wood, V. Bhethanabotla and B. Joseph, *The Journal of Physical Chemistry C*, 2014, DOI: 10.1021/jp509219n.
114. A. Fujishima and K. Honda, in *Nature*, 1972, vol. 238, pp. 37-38.
115. I. K. Konstantinou and T. A. Albanis, *Appl Catal B-Environ*, 2004, 49, 1-14.
116. B. Aurianblajeni, M. Halmann and J. Manassen, *Solar Energy*, 1980, 25, 165-170.
117. P. Christopher, D. B. Ingram and S. Linic, *The Journal of Physical Chemistry C*, 2010, 114, 9173-9177.
118. H. Hakkinen, W. Abbet, A. Sanchez, U. Heiz and U. Landman, *Angew Chem Int Edit*, 2003, 42, 1297-1300.
119. C.-T. Yang, N. Balakrishnan, V. R. Bhethanabotla and B. Joseph, *The Journal of Physical Chemistry C*, 2014, 118, 4702-4714.
120. D. Çakır and O. Gülseren, *The Journal of Physical Chemistry C*, 2012, 116, 5735-5746.
121. M. A. Henderson, *Surface Science Reports*, 2011, 66, 185-297.
122. H. He, P. Zapol and L. A. Curtiss, *The Journal of Physical Chemistry C*, 2010, 114, 21474-21481.
123. V. P. Indrakanti, H. H. Schobert and J. D. Kubicki, *Energy & Fuels*, 2009, 23, 5247-5256.
124. M. M. Rodriguez, X. H. Peng, L. J. Liu, Y. Li and J. M. Andino, *J Phys Chem C*, 2012, 116, 19755-19764.
125. H. J. Freund and M. W. Roberts, *Surf Sci Rep*, 1996, 25, 225-273.
126. V. P. Indrakanti, J. D. Kubicki and H. H. Schobert, *Energy & Fuels*, 2008, 22, 2611-2618.
127. A. Markovits, A. Fahmi and C. Minot, *Journal of Molecular Structure: THEOCHEM*, 1996, 371, 219-235.
128. W. A. A.-S. Dan C. Sorescu, and Kenneth D. Jordan, *J Chem Phys*, 2011, 135, 124701.
129. M. Setvin, C. Franchini, X. F. Hao, M. Schmid, A. Janotti, M. Kaltak, C. G. Van de Walle, G. Kresse and U. Diebold, *Phys Rev Lett*, 2014, 113.
130. P. Deak, J. Kullgren and T. Frauenheim, *Phys Status Solidi-R*, 2014, 8, 583-586.
131. S. G. Park, B. Magyari-Kope and Y. Nishi, *Phys Rev B*, 2010, 82.
132. D. Cakir and O. Gulseren, *J Phys Chem C*, 2012, 116, 5735-5746.
133. Y. Han, M. Zhang, W. Li and J. L. Zhang, *Phys Chem Chem Phys*, 2012, 14, 8683-8692.
134. U. Aschauer, Y. B. He, H. Z. Cheng, S. C. Li, U. Diebold and A. Selloni, *J Phys Chem C*, 2010, 114, 1278-1284.

135. E. Sanville, S. D. Kenny, R. Smith and G. Henkelman, *J Comput Chem*, 2007, 28, 899-908.
136. R. Wanbayor, P. Deak, T. Frauenheim and V. Ruangpornvisuti, *J Chem Phys*, 2011, 134.
137. A. S. Mazheika, T. Bredow, V. E. Matulis and O. A. Ivashkevich, *J Phys Chem C*, 2011, 115, 17368-17377.
138. L. Liu, W. L. Fan, X. Zhao, H. G. Sun, P. Li and L. M. Sun, *Langmuir*, 2012, 28, 10415-10424.
139. M. M. Rodriguez, X. H. Peng, L. J. Liu, Y. Li and J. M. Andino, in *J Phys Chem C*, 2012, vol. 116, pp. 19755-19764.
140. Z. Cheng, B. J. Sherman and C. S. Lo, *J Chem Phys*, 2013, 138.
141. K. O. Hartman and Hisatsun.Ic, *J Chem Phys*, 1966, 44, 1913-&.
142. G. Ramis, G. Busca and V. Lorenzelli, *Mater Chem Phys*, 1991, 29, 425-435.
143. J. Rasko and F. Solymosi, *The Journal of Physical Chemistry*, 1994, 98, 7147-7152.
144. W. G. Su, J. Zhang, Z. C. Feng, T. Chen, P. L. Ying and C. Li, *J Phys Chem C*, 2008, 112, 7710-7716.
145. L. J. Liu, H. L. Zhao, J. M. Andino and Y. Li, *Acs Catalysis*, 2012, 2, 1817-1828.
146. J. Rasko, *Catal Lett*, 1998, 56, 11-15.
147. J. Rasko and F. Solymosi, *Journal of Physical Chemistry*, 1994, 98, 7147-7152.
148. J. Lee, D. C. Sorescu and X. Y. Deng, *Journal of the American Chemical Society*, 2011, 133, 10066-10069.
149. Z. Zou, J. Ye, K. Sayama and H. Arakawa, *Nature*, 2001, 414, 625-627.
150. X. Zhang, J. Qin, Y. Xue, P. Yu, B. Zhang, L. Wang and R. Liu, *Sci. Rep.*, 2014, 4.
151. D. Lee and Y. Kanai, *Journal of the American Chemical Society*, 2012, 134, 20266-20269.
152. W. Pipornpong, R. Wanbayor and V. Ruangpornvisuti, *Applied Surface Science*, 2011, 257, 10322-10328.
153. L. Mino, G. Spoto and A. M. Ferrari, *The Journal of Physical Chemistry C*, 2014, 118, 25016-25026.
154. K. R. Hahn, M. Iannuzzi, A. P. Seitsonen and J. Hutter, *The Journal of Physical Chemistry C*, 2013, 117, 1701-1711.
155. B. Yoon, H. Hakkinen, U. Landman, A. S. Worz, J. M. Antonietti, S. Abbet, K. Judai and U. Heiz, *Science*, 2005, 307, 403-407.
156. S. Vajda, M. J. Pellin, J. P. Greeley, C. L. Marshall, L. A. Curtiss, G. A. Ballentine, J. W. Elam, S. Catillon-Mucherie, P. C. Redfern, F. Mehmood and P. Zapol, *Nat Mater*, 2009, 8, 213-216.
157. T. Imaoka, H. Kitazawa, W. J. Chun, S. Omura, K. Albrecht and K. Yamamoto, *Journal of the American Chemical Society*, 2013, 135, 13089-13095.
158. X. Tong, L. Benz, P. Kemper, H. Metiu, M. T. Bowers and S. K. Buratto, *Journal of the American Chemical Society*, 2005, 127, 13516-13518.
159. M. Valden, X. Lai and D. W. Goodman, *Science*, 1998, 281, 1647-1650.
160. Y. Watanabe, X. Y. Wu, H. Hirata and N. Isomura, *Catal Sci Technol*, 2011, 1, 1490-1495.
161. U. Heiz, A. Sanchez, S. Abbet and W. D. Schneider, *Journal of the American Chemical Society*, 1999, 121, 3214-3217.
162. A. A. Herzing, C. J. Kiely, A. F. Carley, P. Landon and G. J. Hutchings, *Science*, 2008, 321, 1331-1335.

163. B. Hammer and J. K. Norskov, *Nature*, 1995, 376, 238-240.
164. G. Illing, D. Heskett, E. W. Plummer, H. J. Freund, J. Somers, T. Lindner, A. M. Bradshaw, U. Buskotte, M. Neumann, U. Starke, K. Heinz, P. L. Deandres, D. Saldin and J. B. Pendry, *Surf Sci*, 1988, 206, 1-19.
165. X. Lin, Y. Yoon, N. G. Petrik, Z. J. Li, Z. T. Wang, V. A. Glezakou, B. D. Kay, I. Lyubinetsky, G. A. Kimmel, R. Rousseau and Z. Dohnalek, *J Phys Chem C*, 2012, 116, 26322-26334.
166. M. Buchholz, P. G. Weidler, F. Bebensee, A. Nefedov and C. Woll, *Phys Chem Chem Phys*, 2014, 16, 1672-1678.
167. A. E. Reed, L. A. Curtiss and F. Weinhold, *Chem Rev*, 1988, 88, 899-926.
168. J. K. Norskov, T. Bligaard, J. Rossmeisl and C. H. Christensen, *Nat Chem*, 2009, 1, 37-46.
169. H. Y. He, P. Zapol and L. A. Curtiss, *Energ Environ Sci*, 2012, 5, 6196-6205.
170. M. Q. Zhao and R. M. Crooks, *Angew Chem Int Edit*, 1999, 38, 364-366.
171. D. S. Deutsch, G. Lafaye, D. X. Liu, B. Chandler, C. T. Williams and M. D. Amiridis, *Catal Lett*, 2004, 97, 139-143.
172. O. M. Wilson, R. W. J. Scott, J. C. Garcia-Martinez and R. M. Crooks, *Chemistry of Materials*, 2004, 16, 4202-4204.
173. C. J. Crump, J. D. Gilbertson and B. D. Chandler, *Top Catal*, 2008, 49, 233-240.
174. H. Lin, C. P. Huang, W. Li, C. Ni, S. I. Shah and Y. H. Tseng, *Appl Catal B-Environ*, 2006, 68, 1-11.
175. D. O. Scanlon, C. W. Dunnill, J. Buckeridge, S. A. Shevlin, A. J. Logsdail, S. M. Woodley, C. R. A. Catlow, M. J. Powell, R. G. Palgrave, I. P. Parkin, G. W. Watson, T. W. Keal, P. Sherwood, A. Walsh and A. A. Sokol, *Nat Mater*, 2013, 12, 798-801.
176. H.-C. Zhou, J. R. Long and O. M. Yaghi, *Chemical Reviews*, 2012, 112, 673-674.
177. L.-M. Yang, P. Ravindran and M. Tilset, *Inorganic Chemistry*, 2013, 52, 4217-4228.
178. S. Kitagawa, R. Kitaura and S.-i. Noro, *Angewandte Chemie International Edition*, 2004, 43, 2334-2375.

APPENDIX A: COPYRIGHT INFORMATION

Below is the permission for the use of Chapter 3

1/27/2015 Rightslink® by Copyright Clearance Center

Copyright Clearance Center RightsLink® Home Create Account Help Live Chat

ACS Publications Most Trusted. Most Cited. Most Read.

Title: Interplay between Subnanometer Ag and Pt Clusters and Anatase TiO2 (101) Surface: Implications for Catalysis and Photocatalysis

Author: Chi-Ta Yang, Nianthrini Balakrishnan, Venkat R. Bhethanabotla, et al

Publication: The Journal of Physical Chemistry C

Publisher: American Chemical Society

Date: Mar 1, 2014

Copyright © 2014, American Chemical Society

LOGIN

If you're a copyright.com user, you can login to RightsLink using your copyright.com credentials. Already a RightsLink user or want to learn more?

PERMISSION/LICENSE IS GRANTED FOR YOUR ORDER AT NO CHARGE

This type of permission/license, instead of the standard Terms & Conditions, is sent to you because no fee is being charged for your order. Please note the following:

- Permission is granted for your request in both print and electronic formats, and translations.
- If figures and/or tables were requested, they may be adapted or used in part.
- Please print this page for your records and send a copy of it to your publisher/graduate school.
- Appropriate credit for the requested material should be given as follows: "Reprinted (adapted) with permission from (COMPLETE REFERENCE CITATION). Copyright (YEAR) American Chemical Society." Insert appropriate information in place of the capitalized words.
- One-time permission is granted only for the use specified in your request. No additional uses are granted (such as derivative works or other editions). For any other uses, please submit a new request.

BACK CLOSE WINDOW

https://s100.copyright.com/AppDispatchServlet

Appendix A (Continued)

Below is the permission for the use of Chapter 4

1/27/2015 Rightslink® by Copyright Clearance Center

Copyright Clearance Center RightsLink® Home Create Account Help Live Chat

ACS Publications Most Trusted. Most Cited. Most Read.

Title: CO2 Adsorption on Anatase TiO2 (101) Surfaces in the Presence of Subnanometer Ag/Pt Clusters: Implications for CO2 Photoreduction

Author: Chi-Ta Yang, Brandon C. Wood, Venkat R. Bhethanabotla, et al

Publication: The Journal of Physical Chemistry C

Publisher: American Chemical Society

Date: Nov 1, 2014

Copyright © 2014, American Chemical Society

LOGIN

If you're a copyright.com user, you can login to RightsLink using your copyright.com credentials. Already a RightsLink user or want to learn more?

PERMISSION/LICENSE IS GRANTED FOR YOUR ORDER AT NO CHARGE

This type of permission/license, instead of the standard Terms & Conditions, is sent to you because no fee is being charged for your order. Please note the following:

- Permission is granted for your request in both print and electronic formats, and translations.
- If figures and/or tables were requested, they may be adapted or used in part.
- Please print this page for your records and send a copy of it to your publisher/graduate school.
- Appropriate credit for the requested material should be given as follows: "Reprinted (adapted) with permission from (COMPLETE REFERENCE CITATION). Copyright (YEAR) American Chemical Society." Insert appropriate information in place of the capitalized words.
- One-time permission is granted only for the use specified in your request. No additional uses are granted (such as derivative works or other editions). For any other uses, please submit a new request.

BACK CLOSE WINDOW

https://s100.copyright.com/AppDispatchServlet

1/27/2015 Rightslink® by Copyright Clearance Center

Copyright © 2015 Copyright Clearance Center, Inc. All Rights Reserved. Privacy statement.
Comments? We would like to hear from you. E-mail us at customercare@copyright.com

APPENDIX B: SUPPORTING INFORMATION

Below is the supporting information for Chapter 3, 4 and 5 (Figure 38-41 for Chapter 3; Figure 42-44 and Table B1 for Chapter 4; Figure 45-46 for Chapter 5).

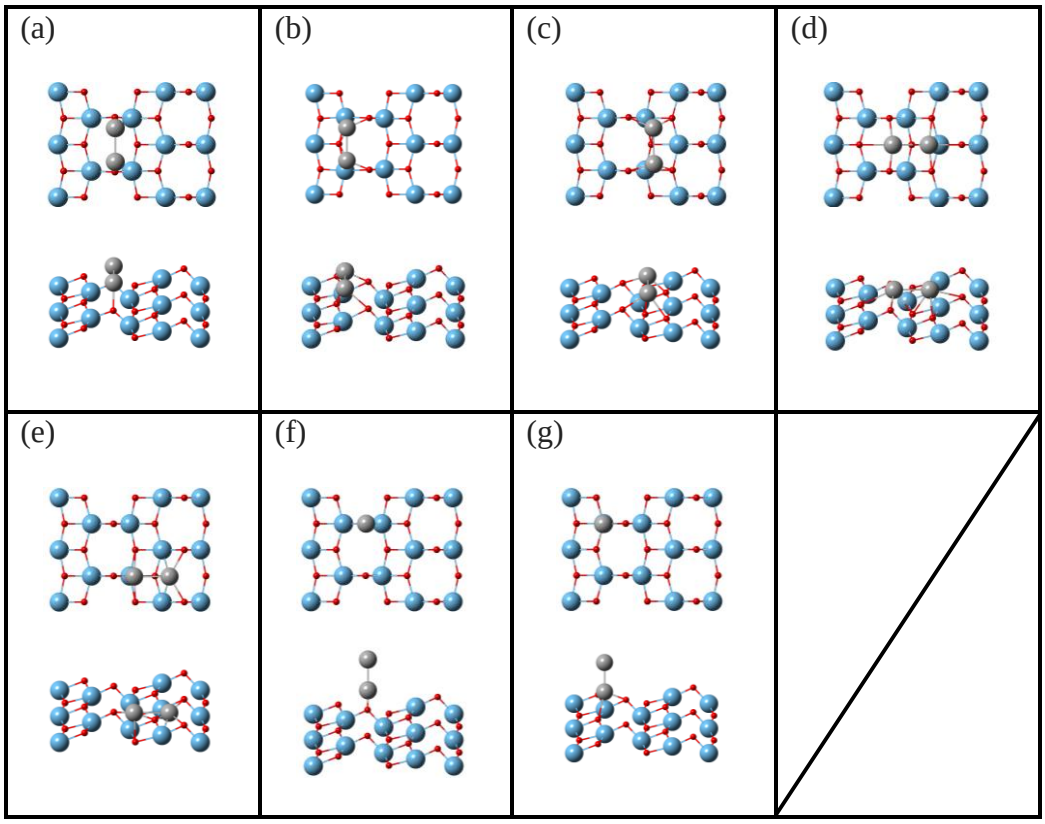

Figure B1 Initial adsorption configurations of Ag and Pt dimers (Ti in blue, O in red, and Ag or Pt in silver).

Appendix B (Continued)

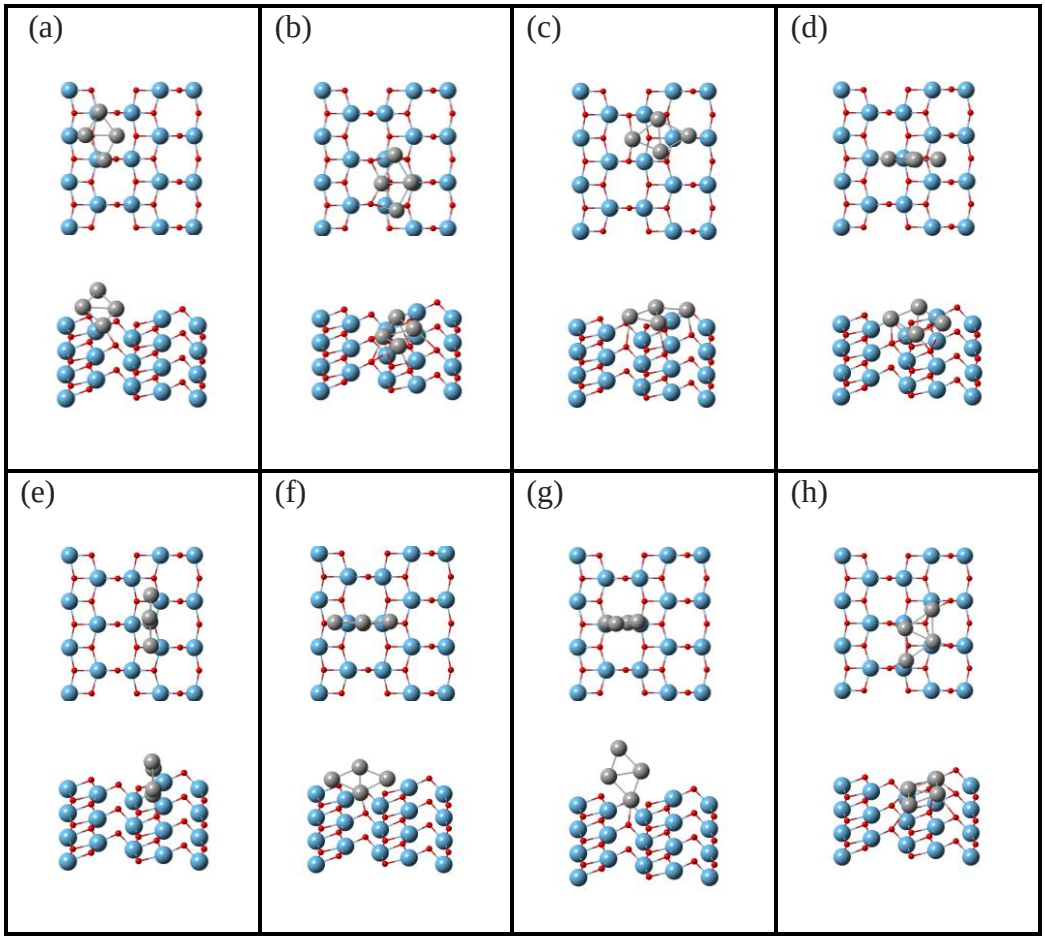

Figure B2 Initial adsorption configurations of Ag and Pt tetramers (Ti in blue, O in red, and Ag or Pt in silver).

Appendix B (Continued)

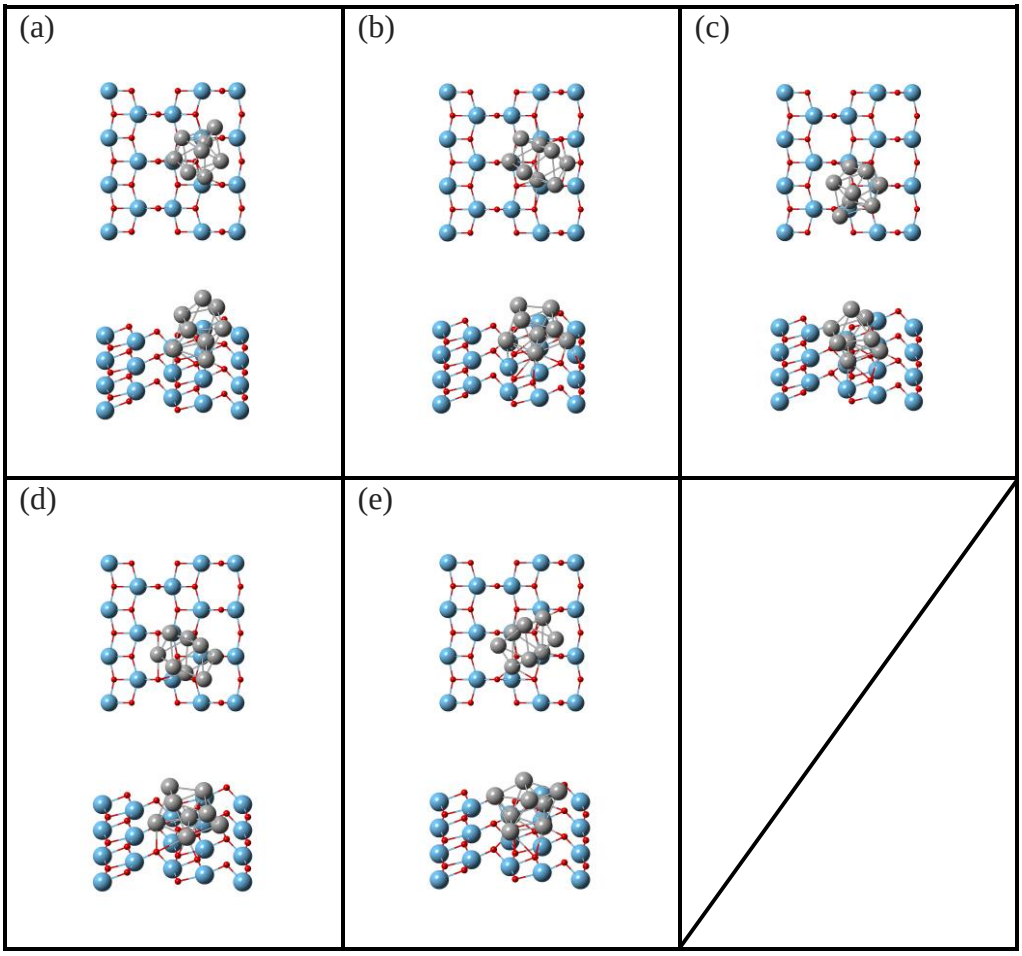

Figure B3 Initial adsorption configurations of Ag and Pt octamers (Ti in blue, O in red, and Ag or Pt in silver).

Appendix B (Continued)

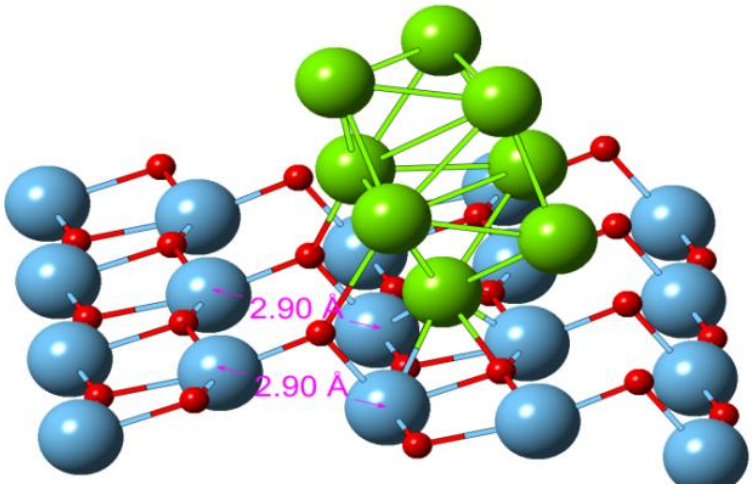

Figure B4 Assumed Pt and Ag octamers adsorbed on the model surface after its diffusion and rotation as temperature is increased (Ti in blue, O in red, and Pt or Ag in green).

Appendix B (Continued)

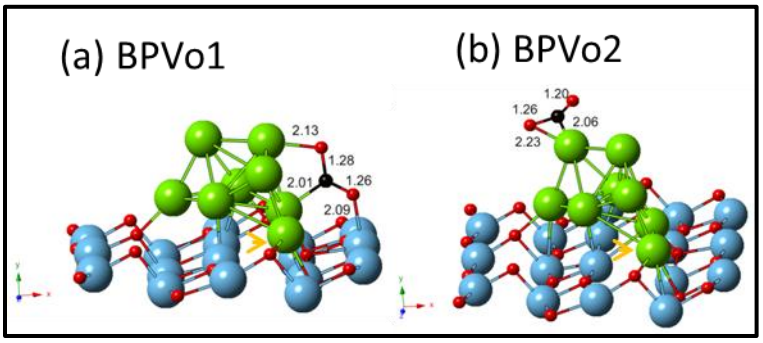

Figure B5 Stable CO_2 adsorption configurations on reduced anatase TiO_2(101) surface: (a) at the interface edge of the Pt octamer and reduced surface, and (b) directly on the Pt octamer (O in red, C in black, Ti in blue. Yellow arrow indicates the oxygen vacancy. The numbers indicate the bond lengths in Å).

Table B1 Calculated Bader charge of CO_2 based on BPVo1 and BPVo2 with standard DFT and DFT+U[a]

Ads. Config.	Δe of CO_2		
	C	O	O
BPVo1	0.595	-0.058	0.039
BPVo1_U3p5	0.599	-0.056	0.049
BPVo1_U4p0	0.603	-0.067	0.047
BPVo1_U4p5	0.599	-0.055	0.053
BPVo2	0.381	-0.086	-0.003
BPVo2_U3p5	0.382	-0.082	0.000

[a] BPVo1 and BPVo2 represent standard DFT. BPVo1_U3p5 and BPVo2_U3p5 represent DFT+U with the value of U=3.5 eV. BPVo1_U4p0 represents DFT+U with the value of U=4.0 eV. BPVo1_U4p5 represents DFT+U with the value of U=4.5 eV.

Appendix B (Continued)

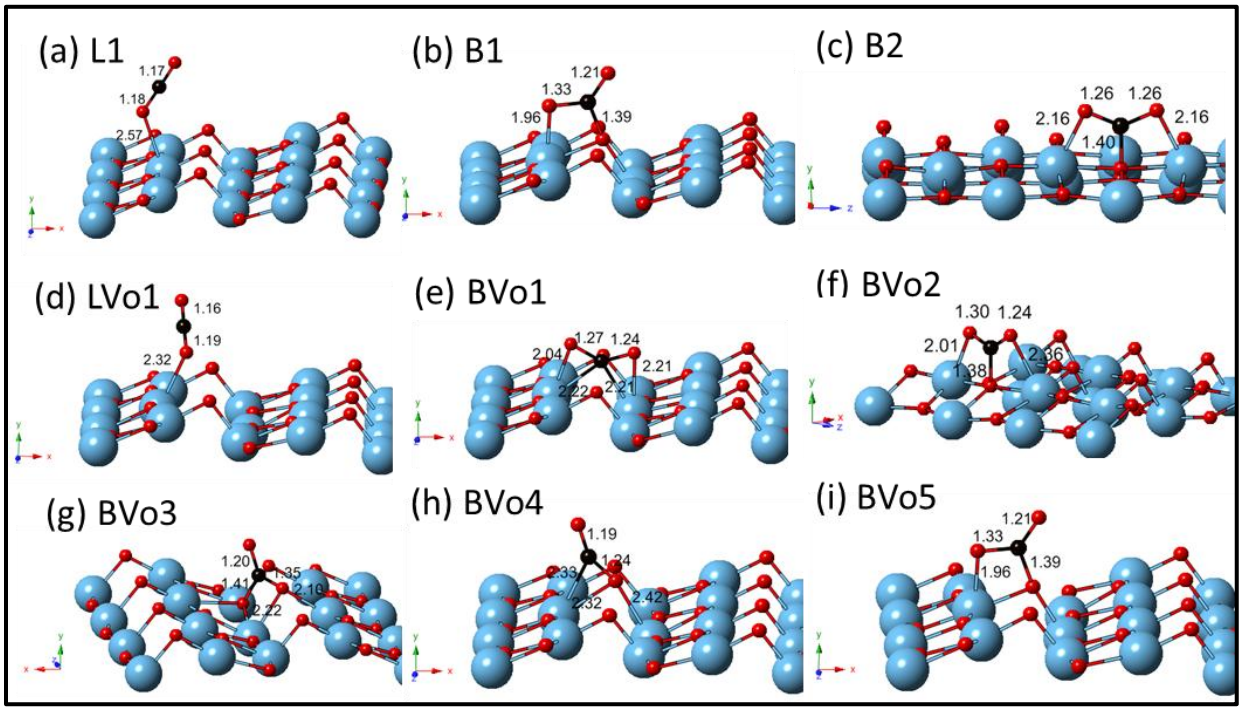

Figure B6 Stable CO_2 adsorption configurations on perfect and reduced anatase (101) surfaces: (a)-(c) on perfect surface, and (d)-(i) on reduced surface (O in red, C in black, Ti in blue. The numbers indicate the bond lengths in Å).

Appendix B (Continued)

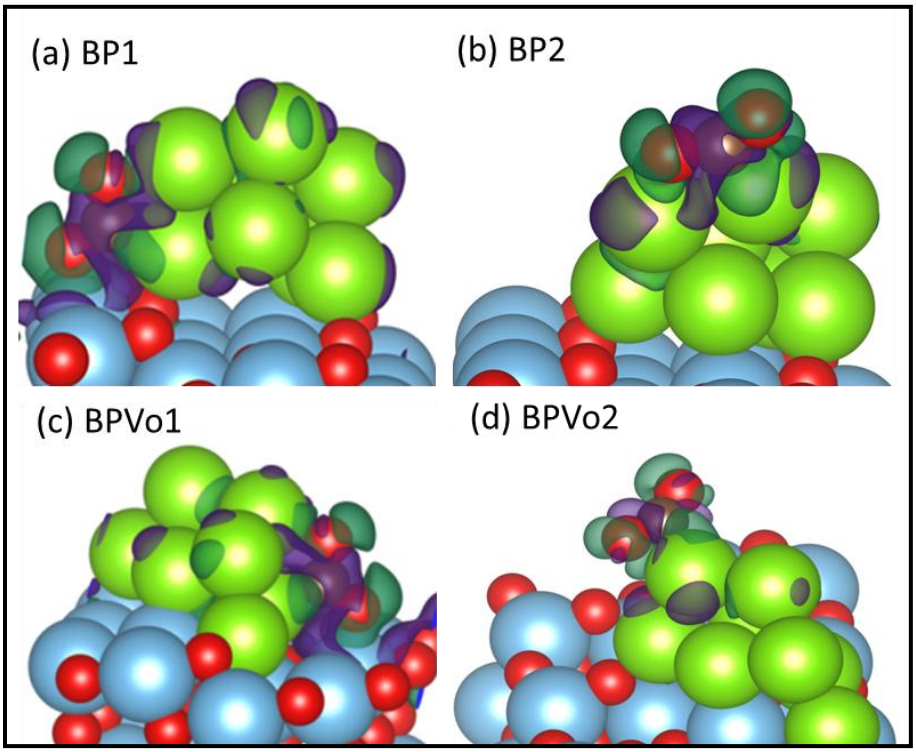

Figure B7 Charge density difference of the adsorbed CO_2: (a) at the interface (BP1) and (b) on the Pt octamer (BP2) on the perfect surface; (c) at the interface (BPVo1) and (d) on the Pt octamer (BPVo2) on the reduced surface (O in red, C in black, Ti in blue, and Pt in green; Purple isosurfaces representing excess, aruba blue isosurfaces representing depletion).

Appendix B (Continued)

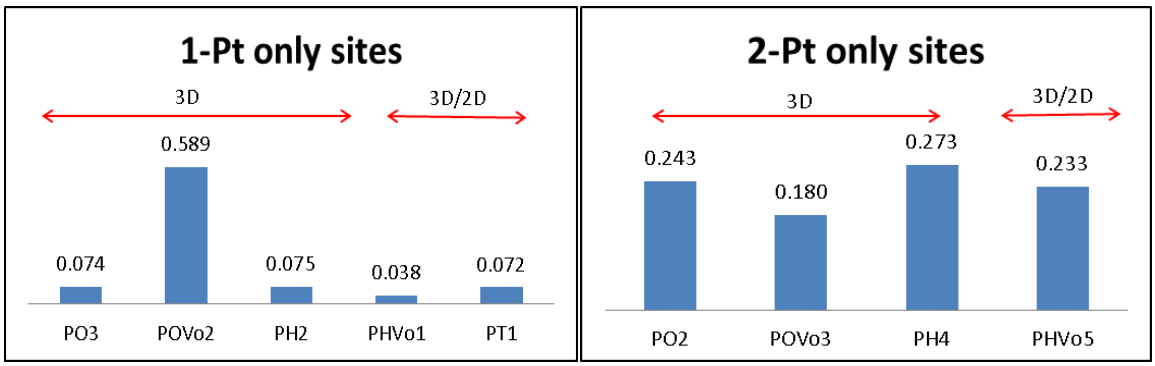

Figure B8 Structural fluxionality of stable Pt only (1-Pt & 2-Pt) sites on perfect and reduced surfaces supported Pt tetramer, hexamer, and octamer. Left: 1-Pt only sites; Right: 2-Pt only sites. [Octamer data[113]: PO2(BP2), PO3(BP3), POVo2(BPVo2), and POVo3(BPVo3); PO, PH, and PT accordingly represent Pt octamer, hexamer, and tetramer; Vo represents an oxygen vacancy].

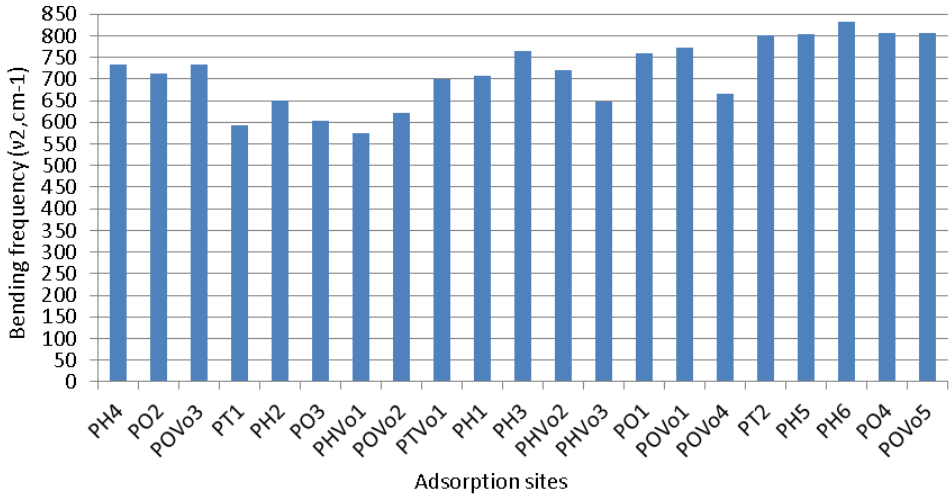

Figure B9 Bending frequency of stable Pt merely sites on perfect and reduced surfaces supported Pt tetramer, hexamer, and octamer (PO1-PO4 represent BP1-BP4 in Figure 1d-g, and POVo1-POVo5 represent BPVo1-BPVo5 in Figure 2d-g of our previous work[113](PO, PH, and PT represent Pt octamer, hexamer, and tetramer; Vo represents an oxygen vacancy).